Consistent space-based retrievals of chlorophyll fluorescence and atmospheric CO_2 and CH_4 for improved estimates of carbon fluxes

Zur Erlangung des akademischen Grades eines
DOKTORS DER NATURWISSENSCHAFTEN
von der Fakultät für Physik des
Karlsruher Institutes für Technologie (KIT)

genehmigte

DISSERTATION

von

Dipl.-Phys. Philipp Hahne
aus Berlin

Tag der mündlichen Prüfung:	13.11.2015
Referent:	Prof. Dr. Johannes Orphal
Korreferent:	PD Dr. Michael Höpfner

Abstract

Understanding the natural carbon cycle and its feedback to climate change requires atmospheric carbon observations to constrain carbon surface fluxes. The Greenhouse Gases Observing Satellite (GOSAT) provides spectroscopic measurements of sunlight backscattered at the Earth's surface and atmosphere containing absorption lines of O_2, CO_2, and CH_4. The retrieval method RemoTeC uses these measurements to retrieve total column averaged dry air mixing ratios of CO_2 and CH_4 (XCO_2 and XCH_4) accounting for the radiative transfer in a multiple scattering atmosphere. This work evaluates the performance of the so called full physics RemoTeC retrieval and shows that using the O_2 A-band in the retrieval is essential to account for atmospheric scattering effects properly. The O_2 A-band comprises the chlorophyll fluorescence, a spectral signal of plants photosynthesis. This work successfully retrieves the chlorophyll fluorescence using solar Fraunhofer lines on a monthly 4° by 4° grid and finds it to be highly correlated with photosynthetic gross primary production. If neglected, the spectroscopic signal of chlorophyll fluorescence affects the full physics aerosol retrieval and thereby affects the XCO_2 and XCH_4 retrieval. This work improves the full physics retrieval such that it accounts for chlorophyll fluorescence. Finally, this work shows that the XCO_2 retrieval accounting for chlorophyll fluorescence provides observational constraints on carbon surface fluxes and improves CO_2 surface flux estimates in the tropics.

Preface

The time of my dissertation were accompanied by many nice people, interesting events, and a lot of discussions. I want to thank a few people for the contributions and encouragements I received from them.

First of all, I want to thank my advisor André Butz. He was the one who wrote RemoTeC. It was an honor for me that I could refine and develop parts of RemoTeC under his supervision. He was always at hand if any question occurred and never missed the chance to point out the scientific context of a discussed issue. At the same time he gave me the freedom to follow my own ideas. Further, he introduced me to many people of his international network and gave me the opportunity to participate in important conferences.

I want to thank many people at the Netherlands Institute for Space Research (SRON) in Utrecht, where I enjoyed a three month internship. During this internship I implemented some changes in RemoTeC's core, the radiative transport algorithm LINTRAN, which was developed by Jochen Landgraf and Otto Hasekamp. I thank them both for the warm welcome, the supervision when working on the code, and for many discussions in every episode of my dissertation. Dinand Schepers, Sandrine Guerlet, Haili Hu, Rob Detmers, Arno de Lange, and Joost aan de Brugh I want to thank for fruitful discussions about RemoTeC and the joint work on improving RemoTeC.

I thank Johannes Orphal for reviewing my dissertation and granting me the excellent fife week winter school European Research Course on Atmospheres (ERCA) in Grenoble, France.

I want to thank Michael Höpfner for being the second referee of my thesis.

I thank Sourish Basu for supplying me with surface carbon flux estimates that helped me with discussing the significance of my work.

I am grateful for the discussions I had with Christian Frankenberg who had the idea and paved the way to retrieve chlorophyll fluorescence from GOSAT spectra.

My special thanks belong to my colleagues of our young investigator research group at the Karlsruhe Institute of Technology (KIT). I want to thank Arne Babenhauserheide and Friedrich Klappenbach for a great time working together on the same goal: remote sensing of greenhouse gases for carbon cycle modelling. Each of us worked in our own domain. Friedrich Klappenbach was working on the instrument development. I was working on the greenhouse gas retrievals. Arne Babenhauserheide was working on modelling carbon sources and sinks. It was great to learn from each other and to provide each other insights into the specific issues. I want to thank Arne Babenhauserheide, Friedrich Klappenbach, Constanze Fischerkeller, and Julian Kostinek for many discussions and for their proofreading and comments concerning this thesis.

I want to thank my colleagues from IMK, especially the lunch break group 'Teerunde' for many discussions, quizzes and relaxation.

Besonders danken möchte ich meinen Eltern, Petra Hamer-Hahne und Roland Hahne für die Möglichkeiten, mich meinen Weg gehen zu lassen und die zahlreichen Anregungen, die sie mir mitgegeben haben. Sie haben stets interessiert nach mir gefragt und aufmerksam zugehört. Ausserdem haben sie mich mit viel Expertise bei Arbeitstechniken und Motivationsmethoden unterstützt.

Zu guter Letzt gilt mein Dank meiner Frau Lucia Hahne für das gemeinsame Tragen der Dissertation und die erfüllte Zeit. Die organisatorischen, Klarheit verschaffenden und fachlichen Diskussionen haben entscheidend zu dem Erfolg dieser Dissertation beigetragen.

Karlsruhe, August 2015

Contents

1. Greenhouse gases and their biogeochemical cycles

Photosynthesis by plants extracts carbon dioxide (CO_2) from the atmosphere to build biomass. Opposingly, respiration releases CO_2 into the atmosphere. These two mechanisms drive the natural variation of the atmospheric CO_2 abundance with the seasons which is known as fast carbon cycle. Biomass decomposition and respiration of plants and microbials crucially depends on temperature and soil moisture. Water availability controls the photosynthetic activity together with other geophysical parameters, for instance, availability of nutrients and photosynthetic active radiation (Schulze, 2006).

The large stock of biospheric carbon is bound to change with any imbalance in the cycle of photosynthesis and respiration. Due to global warming many regions of the world are subject to changing geophysical conditions. For example, thawing permafrost soils and more frequent droughts and floodings are likely scenarios. Indeed, the terrestrial CO_2 sink has large inter annual variations (Le Quéré et al., 2014). Consequently, monitoring the carbon cycle on a regional scale and understanding the feedback of this fast carbon cycle on climate change is a major scientific challenge for the 21st century.

The Working Group I of the Intergovernmental Panel on Climate Change (IPCC) summarizes current knowledge on climate change in the fifth assessment report (Stocker et al., 2014). The anthropogenic radiative forcing is mainly due to the greenhouse gases CO_2 and methane (CH_4). The stocks and annual fluxes of both gases are shown in figure 1.1 taken from the IPCC report (Ciais et al., 2014).

The major fluxes of CO_2 are photosynthesis opposing respiration and gas exchange between the ocean and the atmosphere. The anthropogenic CO_2 emissions due to fossil fuel burning, cement production, and land usage change sum up to roughly 9 Pg C per year. Both photosynthesis and respiration are on the order of 120 Pg carbon (C) per year and sum up to an anthropogenic induced net biogenic flux of roughly 2.6 Pg C per year from the atmosphere to the land biomass. The ocean atmosphere gas exchange is on the order of 80 Pg C per year and results, due to anthropogenic carbon emissions, in an ocean sink of approximately 2.3 Pg C per year. Consequently, roughly 4 Pg C per year of the anthropogenic CO_2 emissions remain in the atmosphere. This results in an increase of nearly 2 parts per million (ppm) of the total column averaged dry air mixing ratio of CO_2 (XCO_2) per year.

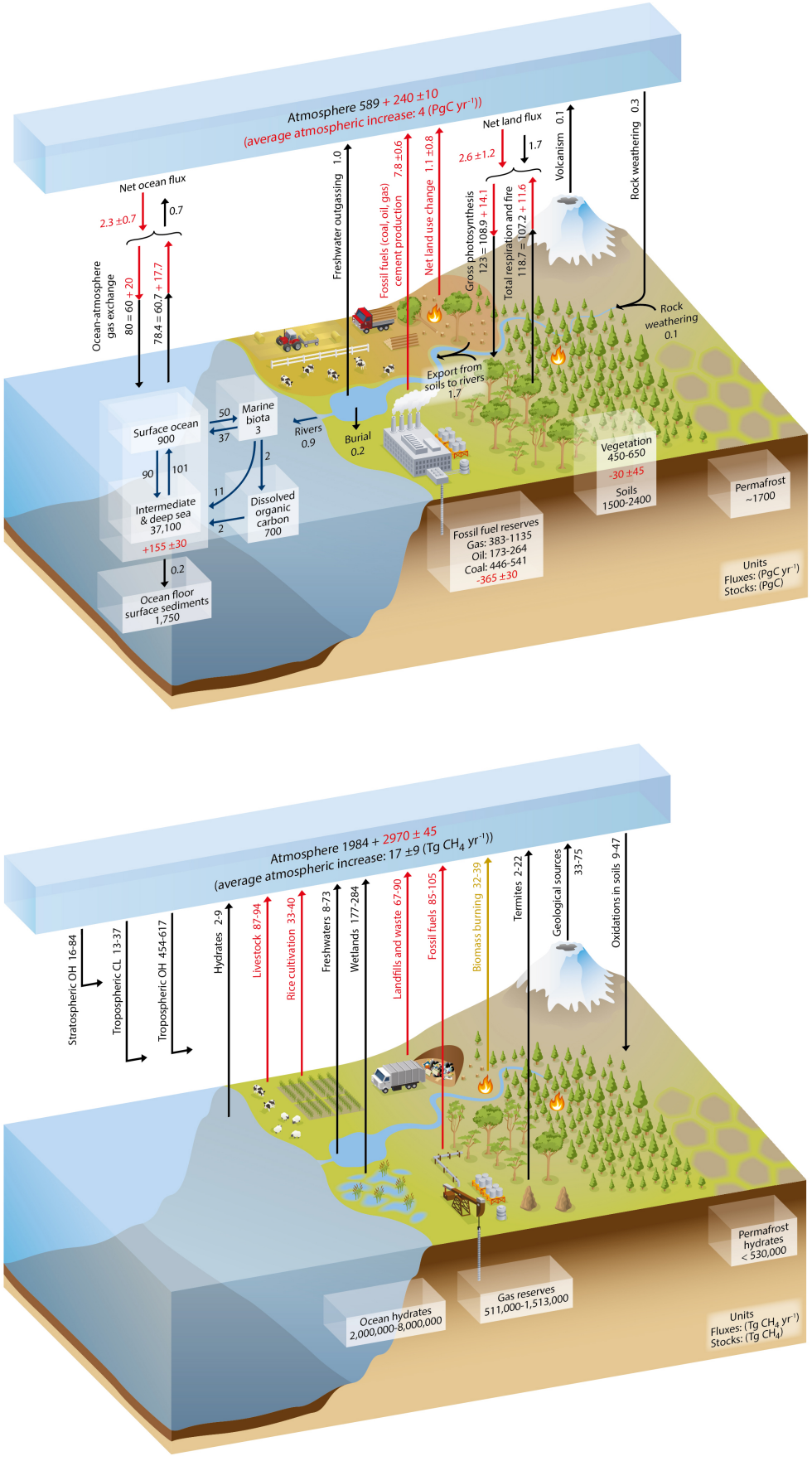

Figure 1.1.: The carbon cycle of CO_2 and CH_4 reported by the IPCC. The arrows denote the carbon fluxes. Changes or fluxes through anthropogenic activity are illustrated in red.

The main source of atmospheric CH_4 are wetlands and anthropogenic emissions due to livestock, rice cultivation, landfills, and fossil fuel leakages. In contrast to CO_2, CH_4 is removed from the atmosphere by chemical reactions mainly with hydroxyl radical (OH).

To estimate the sources and sinks of these greenhouse gases, inverse transport models need constraints by accurate global greenhouse gas concentration measurements (e.g. Meirink et al., 2008). The established measurement programs comprise in situ measurements, spectroscopic ground-based measurements, and satellite borne spectroscopic measurements (overviews are given for example by Masarie et al., 2014; Buchwitz et al., 2013). The in situ measurements are highly accurate. However, they are only representative for the air mass at the measurement location (Gerbig et al., 2003). In contrast, spectroscopic measurements sample the total air column and thus represent a larger air mass. Ground-based spectrometers are easier to operate than satellite missions. Moreover, by measuring direct sunlight they avoid complex radiative transfer problems. However, to observe the Earth's atmosphere on a global scale several satellite missions were developed and are planed for the future (e.g. Yokota et al., 2004; Crisp et al., 2004; Veefkind et al., 2012).

The Greenhouse Gases Observing Satellite (GOSAT, Yokota et al., 2004; Kuze et al., 2012) was launched on January 23 in 2009. It is the first satellite monitoring both greenhouse gases CO_2 and CH_4 using high resolution spectrometers. It provides the opportunity to estimate the sources and sinks on a sub-continental scale. This satellite instrument is introduced in chapter 2.

The algorithm RemoTeC retrieves XCO_2 and XCH_4 abundances from GOSAT spectra (Butz et al., 2009, 2010, 2011). The core of RemoTeC is an efficient radiative transfer model that calculates the sun's lightpath through a multiple scattering atmosphere (Landgraf et al., 2001; Hasekamp and Landgraf, 2002). RemoTeC retrievals using this radiative transfer model are called full physics retrievals. RemoTeC is subject to ongoing development (recent publications by Guerlet et al., 2013a; Schepers et al., 2014). Parts of it are modified and improved in the scope of this work. Chapter 3 gives an overview of its scientific applications and gives details on how it works.

Accuracy and precision of RemoTeC's XCO_2 and XCH_4 records are evaluated against the ground-based Total Carbon Column Observing Network (TCCON, Wunch et al., 2011b) in chapter 4.

To improve the retrieval performance, one component of GOSAT's spectroscopic measurements, the O_2 A-band, requires an improved retrieval procedure. In the wavelength range of the O_2 A-band a spectroscopic signal from the ground interferes with the reflected sunlight (Frankenberg et al., 2011b). This spectroscopic signal is on the order of 1% of the sunlight and has been neglected by XCO_2 and XCH_4 full physics retrievals. Thus, this signal was a potential error source in the retrieval of XCO_2 and XCH_4 (Frankenberg et al., 2012). Consequently, this error source hitherto mapped particularly into the sink estimate of CO_2 and also contaminated CH_4 flux estimates. For CO_2, this was particularly malign, because the origin of the spectroscopic signal itself is the sink process of CO_2. When plants photosynthesize biomass, the plants' green color pigments, reemit a part of the absorbed sunlight at wavelengths around the O_2 A-band. This so called chlorophyll fluorescence and its remote sensing is presented in chapter 5 in detail.

The impact of accounting or neglecting chlorophyll fluorescence in the full physics RemoTeC XCO_2 and XCH_4 retrieval is discussed in chapter 6. Further, this chapter evaluates the chlorophyll fluorescence data set retrieved with the full physics setup.

Finally, having XCO_2 retrievals that avoid chlorophyll fluorescence induced errors and having the remotely sensed record on photosynthetic activity chapter 7 presents insights in the regional carbon flux cycle that are provided by the GOSAT observations.

2. The GOSAT instrument and its measurements

This chapter gives an overview of the satellite instrument and the used observations. Section 2.1 introduces the satellite and Section 2.2 describes the instruments on board GOSAT. Finally, Section 2.3 discusses the issues that are relevant for this study.

2.1. The satellite

The Greenhouse Gases Observing Satellite (GOSAT) is the first satellite monitoring both greenhouse gases CO_2 and CH_4 simultaneously with high resolution spectrometers. The Japan Aerospace Exploration Agency (JAXA), the Japanese Ministry of the Environment, and the Japanese National Institute for Environmental Studies (NIES) designed and developed GOSAT and operate it to estimate the sources and sinks of atmospheric carbon dioxide and methane on a sub-continental scale (Kuze et al., 2009).

JAXA launched GOSAT on January 23 in 2009 into a sun synchronous orbit at 666 km altitude. Every three days GOSAT revisits each spot around one o'clock local time having performed 44 orbits in-between (Kuze et al., 2009). GOSAT changes its operation mode every three days. It operates in a nominal nadir mode, an ocean glint mode, and a target mode.

In the nominal operation mode GOSAT measures backscattered sunlight and emitted thermal radiation by looking downward close to nadir geometry. The field of view results in a footprint of 10.5 km diameter at sea level. The maximum off nadir angles are $\pm$ 35°. Due to issues with the pointing mirror system, the initial 5-point cross-track mode was adjusted at the end of June 2009 and in July 2010 finally changed to a 3-point cross-track mode such that GOSAT now measures three spots perpendicular to its flight direction. These three spots have a distance of 260 km. In the ocean glint mode GOSAT points at the specular reflection point as this yields relatively high signal levels whereas in nadir geometry the ocean is dark in the short wave infrared. In the target mode GOSAT points towards requested targets like volcanoes or mega cities (Kuze et al., 2012).

Band	**wavelength range** [cm^{-1}]	**absorption band**	**detector type**	**ILS FWHM** [cm^{-1}]
1	12900 - 13200	O_2 A-band	Si	0.37
2	5800 - 6400	weak CO_2, weak CH_4	InGaAs	0.26
3	4800 - 5200	strong CO_2, H_2O	InGaAs	0.26
4	700 - 1800	CH_4, O_3, CO_2	HgCdTe (MCT)	0.1

Table 2.1.: TANSO-FTS instrument specifications. Listed are the wavelength range with absorber gas and the used detector types and their instrumental line shape width for all four bands.

2.2. The instruments on board GOSAT

GOSAT has the Thermal And Near infrared Sensor for carbon Observation Fourier Transform Spectrometer (TANSO-FTS, Yokota et al., 2004) on board. TANSO-FTS detects the short wave infrared (SWIR) sunlight back-scattered by the Earth's surface and atmosphere as well as the thermal infrared (TIR) radiance emitted by the Earth's surface and atmosphere.

The TANSO-FTS simultaneously measures seven interferograms in four spectral bands. The back-scattered and therefore polarized SWIR radiance is measured in three bands with two detectors each. These detectors measure the radiance in two perpendicular polarization directions called S-polarized radiance and P-polarized radiance. The TIR radiance emitted by the Earth's surface and atmosphere is in good approximation unpolarized and hence measured with one single detector. The three SWIR channels cover the O_2 A-band around 0.7 µm, a weak CO_2 and CH_4 absorption band around 1.6 µm and a strong CO_2 absorption band around 2 µm wavelength. These three SWIR bands are illustrated in the top, middle, and lower panel of figure 2.1, respectively. The figure shows an exemplary GOSAT measurement observed over Australia. The colored bars placed in the upper range of each panel indicate the wavelength intervals that RemoTeC uses in its full physics setup. For details see chapter 3.

Table 2.1 summarizes basic instrument specifications of the TANSO-FTS (Kuze et al., 2009; Hamazaki et al., 2004). The full width half maximum (FWHM) of the instrumental line shape (ILS) is an important measure of the instrument resolution. Galli et al. (2014) discussed the impact of spectral resolution on XCO_2 and XCH_4 retrieval performance. Typically, the ILS of a FTS instrument is a sinc function depending on the optical path length difference and the wavelength. However, due to optical misalignment the GOSAT ILS is somewhat asymmetric in the O_2 A-band (Kuze et al., 2012). Figure 2.2 and its discussion at the end of this section give an illustration of the importance of the ILS.

GOSAT measures S and P polarized radiance separately with two detectors which in principle would make it possible to use both polarizations separately in a vector radiative transfer model. The radiance is polarized both by scattering events in the atmosphere or the Earth's surface and by the instrument itself. The instrument calibration was performed with unpolarized light, though. Thus, the calibration does not provide the information to use both signals independently for all instrument configurations (Kuze et al., 2012). O'Brien et al. (2013) showed that the polarizations of GOSAT are stable, meaning that they are perpendicular to each other for all GOSAT measurement geometries and therefore the first stokes vector component can be simply calculated by the sum of both radiance signals, see chapter 3.

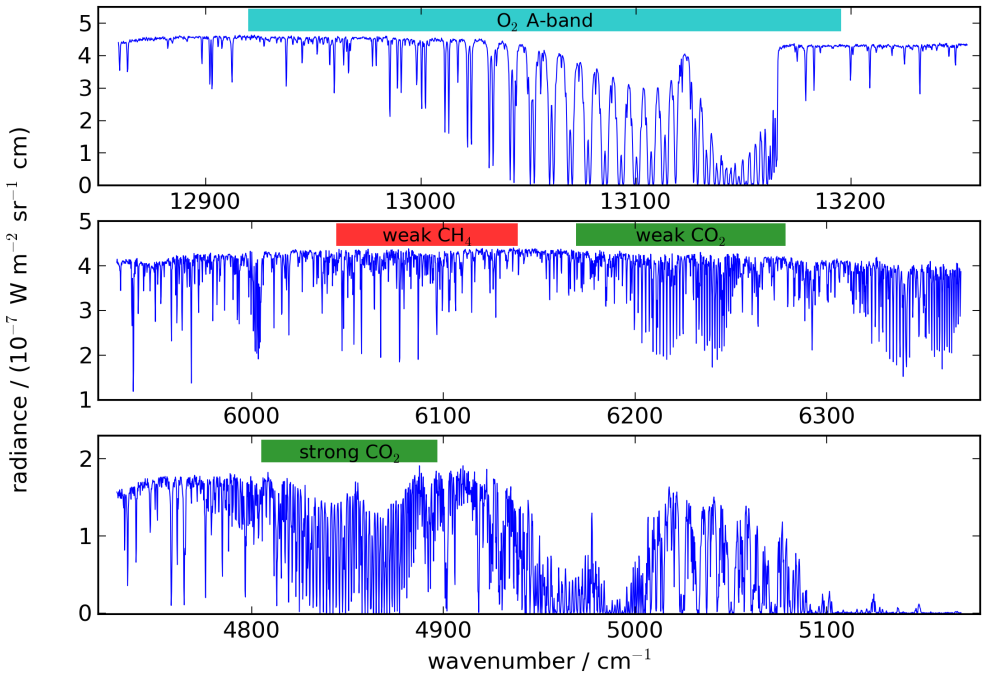

Figure 2.1.: Spectral overview and used retrieval windows. Shown are the three SWIR bands of a spectrum measured on 7th August 2009 over Australia. The upper panel contains the O_2 A-band with some Fraunhofer lines. The middle panel comprises weak absorption lines of CO_2 and CH_4 with some interfering water absorption lines. The lower panel shows three CO_2 absorption lines along with strong water absorption lines. The green bars indicate the spectral range used to retrieve XCO_2. The red and the light blue bar indicate the spectral range used to retrieve XCH_4 and aerosol information via the O_2 A-band, respectively.

The processing of the measured signals is quite different for the different detector types. The detector electronics can measure the signal coming from the detectors both direct coupled (DC) and capacitive coupled (AC). The DC-coupled interferogram contains the complete signal whereas the AC-coupled interferogram contains no offsets, as the capacitance works as high pass filter. To avoid aliasing of noise, the band 1 silicon detectors only acquire the AC signal. The band 2 and 3 InGaAs detectors acquire and co add both the AC signal and the DC signal. The band 4 MCT detector also measures both signals but treats them separately such that the DC signal is used to correct for detector non-linearity. All signals are stepwise amplified and converted to digital voltage signals having 16 bit resolution (Kuze et al., 2009). There are two gain settings, medium gain and high gain. The medium gain setting is used for spectra with high signal level that are typically observed over deserts. Most spectra are recorded with the so-called high gain setting.

In addition, GOSAT carries a Cloud and Aerosol Imager (TANSO-CAI, Ishida et al., 2011) which provides an overview of the observed scenes. RemoTeC used the TANSO-CAI product provided by NIES to filter cloudy scenes up to version 1.9 in 2013. Since version 2.0 RemoTeC uses cloud filters based on preprocessed ratios of O_2, XCO_2, and XH_2O. The filter criteria are summarized in section 3.3.

2.3. Relevant instrument issues

The non-linearity of detectors used in Fourier Transform Spectrometers can lead to a so-called zero level radiance offset in first approximation. Abrams et al. (1994) discusses this effect for MCT detectors. Besides the MCT detector, the two silicon detectors for the O_2 A-band show non-linear behavior. Additionally, any of the signal processing instances described above can cause non-linearity in the signal.

NIES provides the spectra in calibrated so-called level 1B (L1B) format where such zero level radiance offsets are already corrected to some extent. The different L1B versions provided by NIES contain different calibrations. Kuze et al. (2012) presents the GOSAT data level 0 to level 1 processing for the version 150. This work uses L1B version 141 which is available from June 2009 onward. In the wavelength range, considered in this work, the described procedure is virtually the same as in version 141.

Kuze et al. (2012) reports that the amplification in the analog circuit which depends on the capacitance is sensitive to temperature, signal level, gain setting, and time. Furthermore, it is different for each detector. The detector measuring the P-polarization is reported to exhibit stronger time dependence than the one measuring S-polarization.

Previous RemoTeC versions retrieved a radiance offset parameter (Guerlet et al., 2013b). The new RemoTeC setup presented in this work retrieves the offset of the uncalibrated spectrum. It is not a radiance offset but a detector signal offset in Volt units. However, this volt signal offset is named radiance offset to avoid confusion with published reports.

The mixed sources radiance offset depends on many parameters, chapter 5 discusses the dependencies of the radiance offset found in the level 2 data. In particular, the radiance offset depends on signal level, wavelength, detector gain setting, and time.

Figure 2.2 shows some more measurement details for the O_2 A-band. The upper panel shows the GOSAT measurement and the RemoTeC modeled spectrum in the O_2 A-band. The spectrum is measured over France on June 18 in 2009. Two spectral zooms highlight a Fraunhofer line and a double absorption line in the center of the O_2 A-band.

The lower panel of figure 2.2 shows the fit residuum which is the difference between the modeled and the measured spectrum. The residuum contains some structures apart from noise which hint at systematic errors that might come from the radiative transfer model in RemoTeC, instrument artifacts or spectroscopic inaccuracy. Section 6.2 discusses the residuum in closer detail.

As will be shown in chapter 5, the retrieved chlorophyll fluorescence record is quite noisy. To discuss this effect on a single measurement level, the lower panel of figure 2.2 shows a modeled fluorescence spectrum at the top of the atmosphere (TOA). To model this fluorescence spectrum, RemoTeC calculated the spectrum twice. In the second calculation all parameters were kept as in the first one except for the ground based fluorescence emittance source strength within the last iteration. This was enhanced in the last iteration step by 0.6 W m^{-1} sr^{-1} μm^{-1} which is a typical signal strength average in the GOSAT footprint in central Europe in summer. The fluorescence spectrum at the Earth's surface is given by a simple linear model as described in chapter 5. As the fluorescence signal transmits the Earth's atmosphere, it is subject to molecular absorption by O_2. Thus, the signal is nearly constant in the Fraunhofer lines and partially absorbed in the O_2 A-band.

The expected detector noise level is given by the black line in the lower panel of figure 2.2. It is calculated for each polarization by RemoTeC using the measured signal in the out of

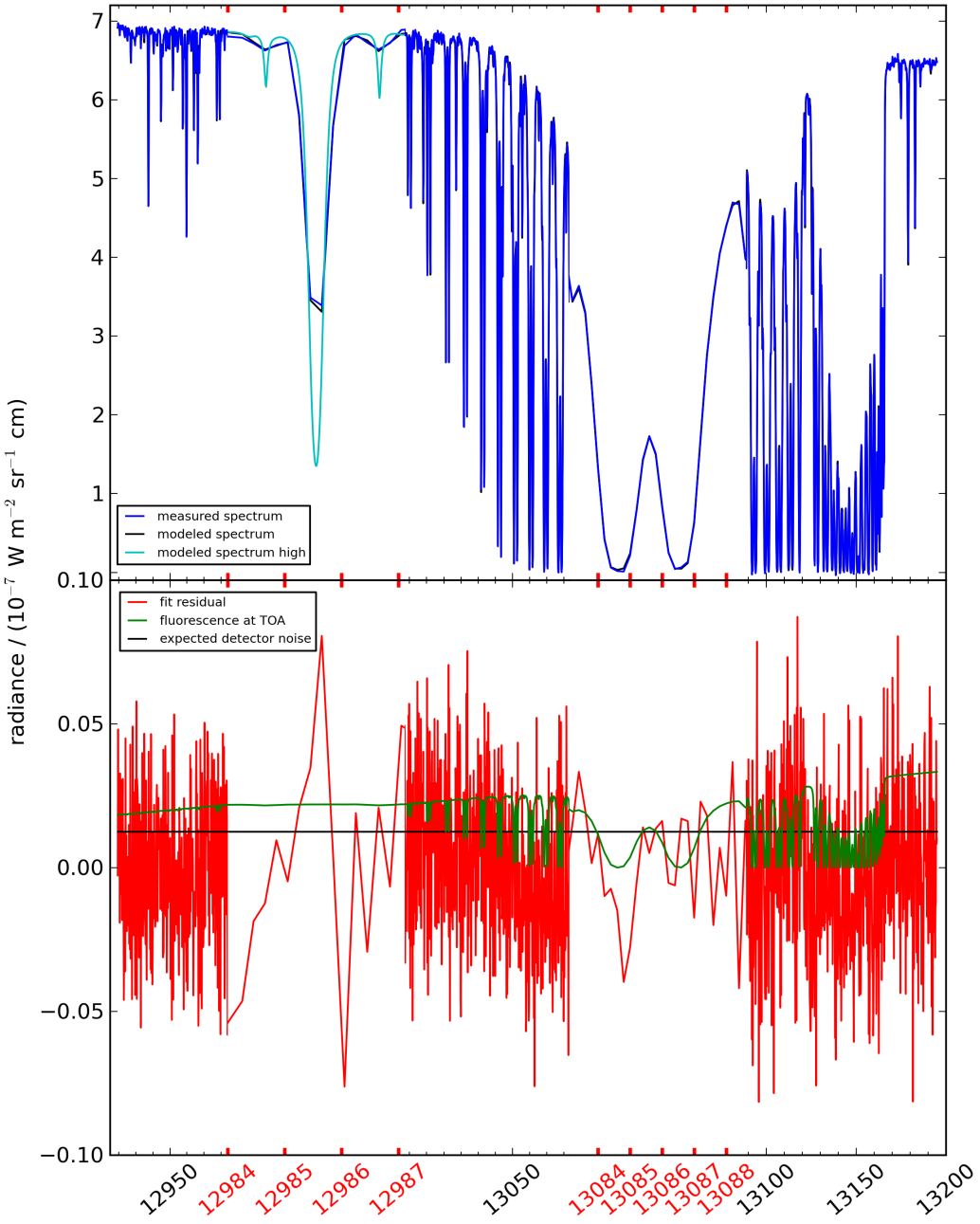

Figure 2.2.: Chlorophyll fluorescence signal in the O_2 A-band. The upper panel shows a measured spectrum in blue and the corresponding modeled spectrum in black with two spectral zooms. One zoom highlights the Fraunhofer line around 770.1 nm wavelength and one highlights a double absorption line in the center of the O_2 A-band. The importance of the ILS is illustrated by the modeled high resolution spectrum before it is convolved with the ILS in light blue within the first spectral zoom. The lower panel shows the fit residuum, that is the difference between the measured and the modeled spectrum, the expected detector noise level, and the theoretical fluorescence signal at the TOA for a typical European summer measurement. The single spectrum fluorescence measurement is clearly noise dominated as the SNR is only about a factor of 2.

band wavelength range where the detectors are insensitive to the incoming radiance. The noise of the radiance intensity is given by $\sigma_I = \sqrt{\sigma_P^2 + \sigma_S^2}$, where σ_P and σ_S denote the noise of each polarization direction.

The strength of the fluorescence signal shown in the lower panel of figure 2.2 is on the order of one percent of the spectral continuum level shown in the upper panel of figure 2.2. The strength of the fluorescence signal is only about a factor two higher than the detector noise. For the spectral range higher than 13170 wavenumbers this ratio is a bit larger, however, the retrieval window used on this side of the O_2 A-band is smaller.

In the vicinity of the Fraunhofer line around 770.1 nm wavelength figure 2.2 shows the high resolution (0.01 cm^{-1}) modeled spectrum before it is convolved with the GOSAT ILS. It is clearly visible that the Fraunhofer line is much deeper when it is measured with an instrument having a substantially higher resolution. In this case the fraction of the chlorophyll fluorescence signal from the measured signal, the so-called infilling effect, would be larger.

3. The retrieval algorithm RemoTeC

This chapter presents the retrieval algorithm RemoTeC. The first section 3.1 describes the scope of RemoTeC, section 3.2 gives a schematic overview of how RemoTeC works, section 3.3 summarizes the different setups which this work uses. The two final sections 3.5 and 3.6 give a description of the two core modules namely the radiative transport model and the inversion scheme, respectively.

3.1. Scope of RemoTeC

RemoTeC provides the data infrastructure, an efficient radiative transport model (RTM), and an inversion scheme to perform highly accurate retrievals of atmospheric trace gas abundances from solar radiance measurements. Its key characteristic is its sophisticated physics based retrieval which infers the trace gas abundance along with effective parameters accounting for light path modifications due to atmospheric scattering events. It is designed for current and future satellite and ground-based missions.

Two research groups are jointly developing this algorithm. One is located at the Netherlands Institute for Space Research in Utrecht, Netherlands, and the other is located at the Karlsruhe Institute for Technology in Karlsruhe, Germany. First RemoTeC studies by Butz et al. (2009, 2010) where based on simulated radiance measurements to show retrieval performance for column averaged dry air mixing ratios of CO2 (XCO_2) and CH_4 (XCH_4) in a scattering atmosphere. Since then RemoTeC has been used mainly to infer XCO_2 and XCH_4 records from the GOSAT satellite for example in Butz et al. (2011); Guerlet et al. (2013b). Several improving updates are reported, see Schepers et al. (2014) and references therein. The provided data sets have been shown to add valuable information to inverse modeling studies of sources and sinks for CO_2 (Basu et al., 2014; Takagi et al., 2014; Reuter et al., 2014) and for CH_4 (Alexe et al., 2015). Further, the RemoTeC XCO_2 and XCH_4 data record is part of the GreenHouse Gas Climate Change Initiative (GHG-CCI, Buchwitz et al., 2013; Dils et al., 2014). Additionally, RemoTeC is ready to analyze spectra from the recently launched Orbiting Carbon Observatory 2 (OCO-2, Crisp et al., 2004) satellite and is the official operating algorithm for the Tropomi instrument aboard the Sentinel 5 Precursor (S5P) satellite (Butz et al., 2012; Checa-Garcia et al., 2015).

3.2. Scheme of RemoTeC

The scheme in figure 3.1 illustrates how RemoTeC works. The radiative transfer model (RTM) receives a lot of input indicated by the light blue box. The meteorological input information is collected for each spectrum in a preprocessing step. It contains profile information on humidity as well as profile and surface information on wind speed, temperature and pressure. This information is interpolated to the time and place of the measurement from the ERA-Interim analysis data set from the European Centre for Medium-Range Weather Forecasts which is provided in a spatial resolution of 0.75° by 0.75° latitude by longitude in six hour intervals (Dee et al., 2011).

The spectroscopic information about the molecular absorption lines is based on HITRAN 2008 parameters (Rothman et al., 2009). The line shape of CH_4 and H_2O are Voigt profiles. The line shape profile of CO_2 accounts for line-mixing (Lamouroux et al., 2010). The line shape of O_2 accounts for line-mixing as well and additionally accounts for collision-induced absorption (Tran and Hartmann, 2008).

Information about the surface elevation within the GOSAT footprint is extracted from the SRTM [1] data base. Information about the measurement geometry, for instance the solar zenith angle, are given along with the GOSAT spectrum.

The blue box in the top right of figure 3.1 provides the atmospheric state vector. The state vector retrieval parameters are initially derived from a priori knowledge and are updated during the iteration process. The a priori CO_2 profile and the CH_4 profile are taken from Carbon Tracker (Peters et al., 2007) and TM4 (Meirink et al., 2006), respectively. The number of the RemoTeC state vector parameters is subject to the implemented retrieval setup. It generally comprises the amount of the target gases given in twelve atmospheric layers equidistant in pressure down to 0.1 hPa, the total amount of interfering gas absorbers if existing, the aerosol parameters if not neglected, a radiance offset parameter in the O_2 A-band, and for each retrieval window two spectral shift parameters and three albedo parameters. The spectral shift is twofold as the orbit of the Earth around the Sun and the satellite orbit around the Earth may both cause a Doppler shift. The three albedo parameters drive a Lambertian model for land spectra with two parameters for the albedo slope. These two parameters are also used for ocean glint spectra, for which the zeroth order albedo is calculated from a wind speed driven Cox and Munk model (Cox and Munk, 1954).

The RTM itself contains the model of the atmosphere and the mathematical description of the radiative transfer. This is a core module of RemoTeC and is presented in more detail in section 3.5. The RTM supplies the inversion routine with the modeled spectrum and the sensitivity of that spectrum with respect to the atmospheric state parameters.

The inversion scheme in the middle of figure 3.1 calculates the fit residuum, that is the difference between the modeled spectrum taken from the RTM above and the measured GOSAT spectrum. Using the sensitivity of the spectrum, also supplied by the RTM, and considering the physical assumptions and the boundary conditions, the inversion scheme updates the atmospheric state parameters to minimize the fit residuum. During the iteration process the fit residuum decreases. As soon as the fit residuum is smaller than a defined threshold, the inversion module stops the iteration process and passes the final atmospheric state vector to the post processing instance. More detail about the inversion scheme is discussed in section 3.6.

[1] url: www2.jpl.nasa.gov/srtm/ on 2015/08/14

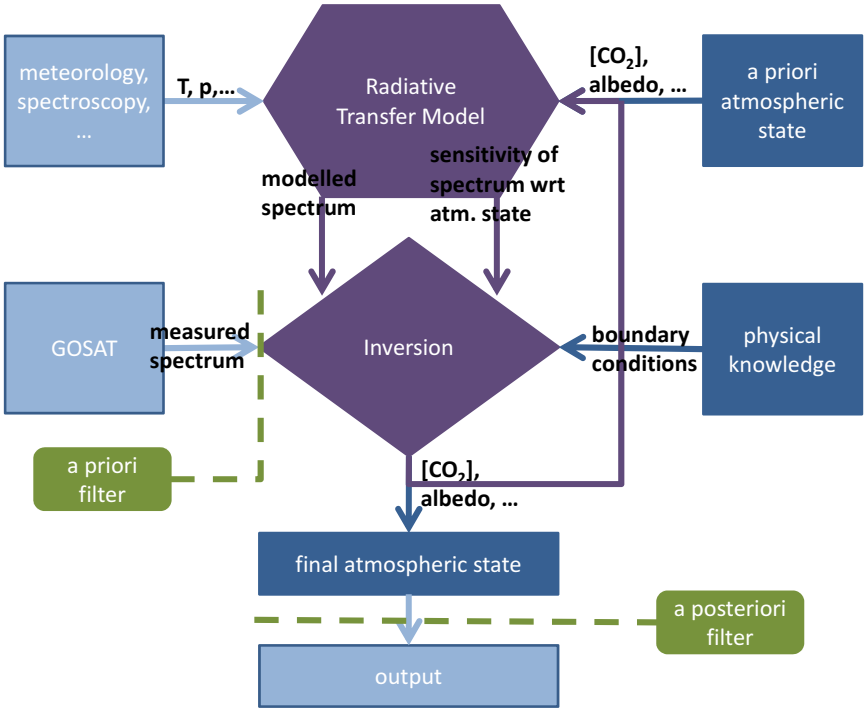

Figure 3.1.: This scheme shows how RemoTeC works. The two core modules (violet) show the radiative transfer model (RTM) and the inversion routine. The light blue boxes illustrate the data input and output. Two types of filters are involved (green). In blue are illustrated the physical assumptions, the prior knowledge, and the state vector parameters.

Finally, RemoTeC generates the output which contains the column averaged dry air mixing ratios of the target gases and also comprises an error estimate, the complete state vector, a priori information, the averaging kernel, and some meta data, for example the number of iterations and a quality flag. In addition, the RemoTeC output summarizes some instrument information, for instance, instrument quality flags, lists the preprocessed meteorological information, and collects some setup information.

The green boxes in figure 3.1 demonstrates the two types of involved filters. A priori filters screen the GOSAT spectra for measurement quality and geometries the radiative transfer model is not designed for. The information that is needed for these filters is prepared and formatted along with input information for RemoTeC in a preprocessing step. Additionally, a posteriori filters screen the record for inversion quality like χ^2 and, for instance, aerosol scenarios for which RemoTeC is not yielding the targeted single measurement precision.

3.3. Setups of RemoTeC

The previously described scheme of RemoTeC has different realizations. The following two sections present two setups that are subject to this study. First, the so-called full physics retrieval setup is presented, which is the most sophisticated retrieval scheme of RemoTeC to retrieve XCO_2 and XCH_4. Second, an overview is given of the so-called Fraunhofer retrieval scheme, which is developed in this work to retrieve chlorophyll fluorescence.

3.3.1. The full physics setup

The first version of the full physics RemoTeC retrieval is reported by Butz et al. (2011). Major updates have been reported by Guerlet et al. (2013a) and Schepers et al. (2014). The key characteristic of the full physics RemoTeC setup is the retrieval of XCO_2 and XCH_4 together with three aerosol parameters that effectively account for light path modification by atmospheric scattering events. The RTM assumes one single aerosol layer consisting of one spherical aerosol type. The optical properties of this aerosol layer are calculated via Mie theory. The real part of the refractive index is set to $m_r = 1.4$ and the imaginary part is m_i = -0.003. The height distribution of the aerosol particles is assumed to be Gaussian with a fixed layer width. Retrieval parameters are the total particle amount, the mean layer height, and the size distribution parameter α of the particles.

The retrieval windows cover the strong CO_2 absorption band from 4806.0 to 4896.0 cm^{-1}, the weak CH_4 absorption band from 6045.0 to 6138.0 cm^{-1}, the weak CO_2 absorption band from 6170.0 to 6277.5 cm^{-1}, and the O_2 A-band from 12920.0 to 13195.0 cm^{-1}. Figure 3.2 shows a measured and modeled spectrum in the used retrieval windows along with the fit residuum. For illustration purposes, the fit residuum is enhanced by a factor 10. In the strong CO_2 and the weak CH_4 window, interfering H_2O absorption lines appear which are used by RemoTeC to fit the H_2O total column number density. Further, in the weak CH_4 window are some CO_2 absorption lines which have been shown to be spectroscopically inconsistent with the CO_2 absorption lines in the two CO_2 windows (Butz et al., 2013). Therefore, RemoTeC treats these CO_2 absorption lines absolutely independent of the target CO_2. Technically, this is realized by setting the Jacobians of the target CO_2 to zero in the weak CH_4 window and by setting the Jacobians of the interfering CO_2 lines to zero in any window but the weak CH_4 window.

The a priori filters are the GOSAT instrument flags which must have the default values except for the so-called 'spike noise' flag which is ignored. The standard deviation of the surface elevation within the GOSAT footprint has to be below 80 m. The solar zenith angle needs to be below 70°. In earlier RemoTeC versions the cloud filter was based on a product of the GOSAT CAI instrument. In the RemoTeC setup used in this study it is based on three ratios called O_2 ratio, CO_2 ratio, and H_2O ratio. These ratios are calculated in a preprocessing step. The O_2 ratio is the quotient of non scattering retrieved O_2 and the meteorological O_2 input information. The RemoTeC non scattering setup ignores Mie scattering, a description is given in Schepers et al. (2012). The CO_2 ratio and the H_2O ratio are the quotients of CO_2 and H_2O retrieved in the weak absorption band around 1.6 µm and CO_2 and H_2O retrieved in the strong absorption band around 2.0 µm wavelength, respectively. The thresholds used in this study requires the O_2 ratio to be between 0.95 and 1.02, the CO_2 ratio to be between 0.99 and 1.015, and the H_2O ratio to be between 0.95 and 1.07. Cloud filtering based on these ratios is discussed, for instance, in Butz et al. (2013) and Mandrake et al. (2013).

The a posteriori filters for the used land data are: a) the signal to noise ratio (SNR) needs to be higher than 50 for each window and each polarization b) the χ^2 is generally below 4.5 and below 4.0 in the O_2 A-band c) the XCO_2 noise error must be smaller than 1.2 ppm d) the degrees of freedom for the target gas profiles must be higher than 1.0 e) the blended albedo (Wunch et al., 2011b) must be below 0.9 f) the aerosol size parameter α must be between 3.0 and 5.0 g) the scattering optical thickness (SOT) in the O_2 A-band must be below 0.3 and h) the product $\frac{SOT \cdot z}{\alpha}$ must be between 0 and 300.0 m, where z is the height parameter of the aerosol layer. Furthermore, the spectrum needs to converge within 30 iterations. If it needs more than 24 iterations, all three aerosol parameters are set fixed to the current values for the remaining five iterations.

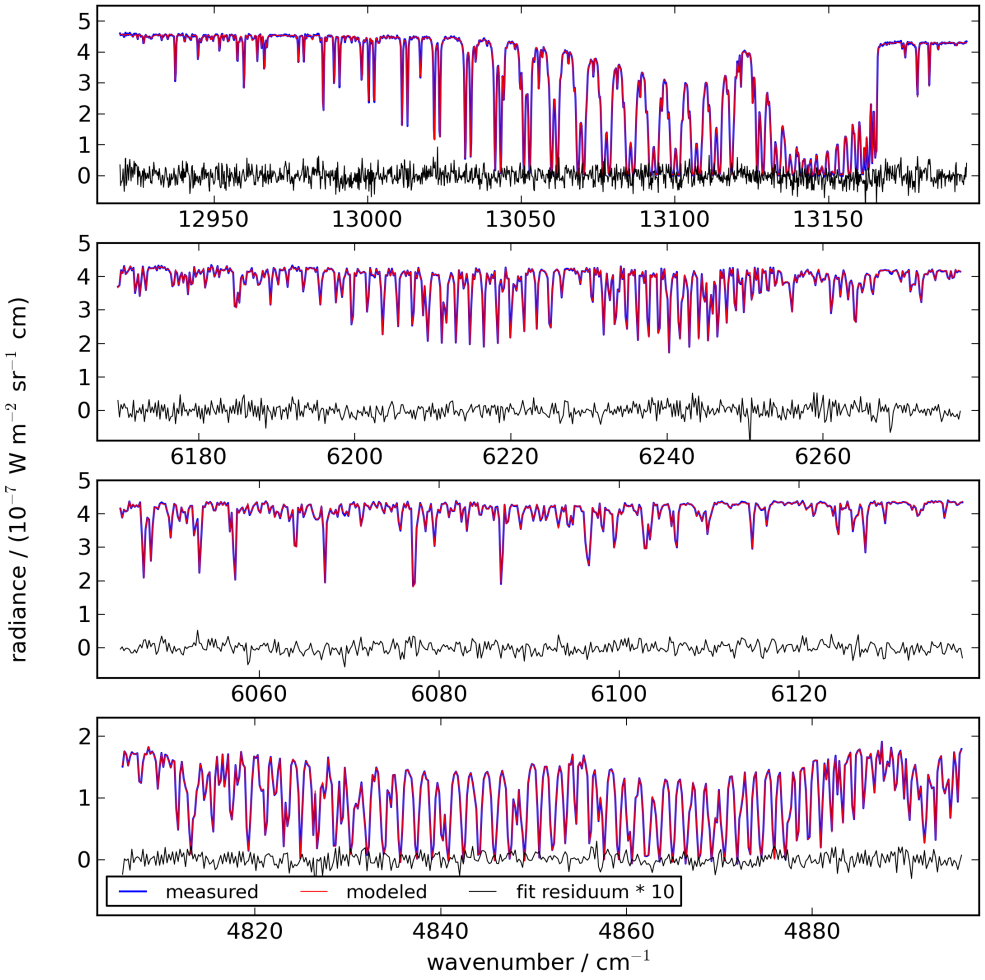

Figure 3.2.: The full physics setup uses the shown spectral ranges which are called retrieval windows. The upper panel shows a GOSAT measurement of the O_2 A-band (blue) along with the modeled spectrum by full physics RemoTeC (red). The difference of these two spectra is the fit residuum which is enhanced by a factor 10 (black). The panel underneath shows the weak CO_2 absorption band and the third panel from top shows the weak CH_4 absorption band. The lower panel shows the strong CO_2 absorption band which is referred to as '2 micron' as it is centered around 2.06 µm wavelength.

3.3.2. The Fraunhofer setup

This retrieval setup is very different from the full physics retrieval setup. This section summarizes the used state vector, the filters and the contrasts to the full physics setup. Chapter 5 discusses the details of how to retrieve chlorophyll fluorescence.

The Fraunhofer setup retrieves chlorophyll fluorescence within two relatively small wavelength windows ranging from 13174.0 to 13226.0 cm^{-1} and from 12905.0 to 12995.0 cm^{-1}. These windows are virtually the same as used by Frankenberg et al. (2011b, 2012) and

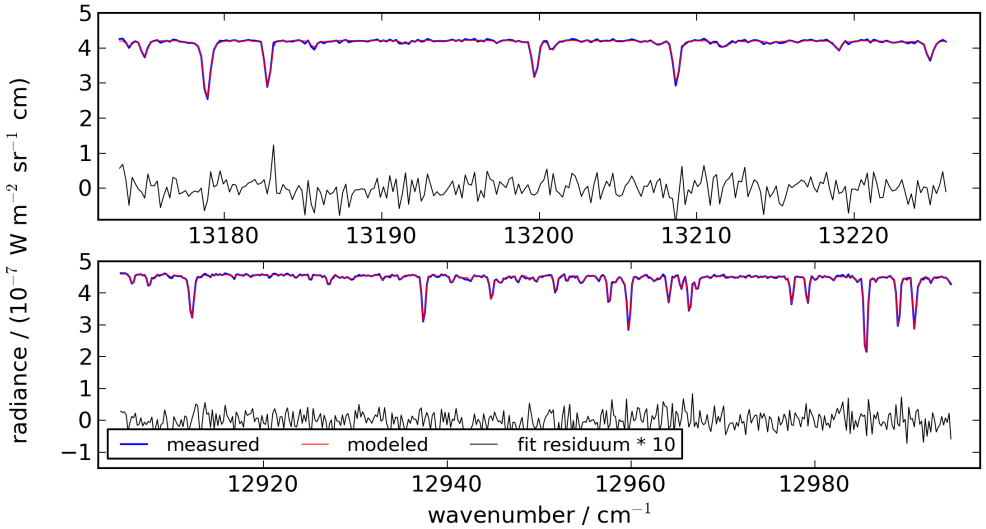

Figure 3.3.: The RemoTeC Fraunhofer setup uses these two small retrieval windows embracing the O_2 A-band. RemoTeC internally represents all wavelengths in wavenumber units. However, prevalent publications about chlorophyll fluorescence use wavelength as unit. To enable direct comparison with the current reports, this study refers to the window in the upper panel as '755 nm window' and the window in the lower panel as '772 nm window'.

are illustrated in figure 3.3. They mainly contain solar Fraunhofer lines which are the main asset of this setup. Technically, every RemoTeC setup needs at least one target gas. So, the interfering O_2 absorption lines from the enclosed O_2 A-band are used to fit O_2 as target gas. The accuracy of the O_2 fit is not evaluated in this study.

In this setup the RTM considers Rayleigh scattering but neglects Mie scattering. As Frankenberg et al. (2012) pointed out, the chlorophyll fluorescence can be retrieved from the Fraunhofer lines even in a cloudy atmosphere without taking atmospheric scattering into account. This so-called non-scattering retrieval is a significantly faster retrieval procedure than the full physics retrieval.

The a priori filters for this setup are the instrument flags and the solar zenith angle which should be below 70°. The a posteriori filters are $\chi^2 < 2.4$ and as cloud filter the O_2 ratio should be between 0.9 and 1.1 which is quite relaxed compared with the values used full physics approach.

3.4. Used data sets

This study uses 40 months of GOSAT data beginning from early June 2009 ending in late September 2012. The medium gain spectra, which are mainly recorded over deserts, are neglected as they are too few for the radiance offset correction procedure discussed in section 5.4. The high gain spectra measured over land and filtered for the full physics setup sum up to 236,173 spectra. From these spectra a subset of 31,625 spectra is coincident with measurements from the Total Carbon Column Observing Network (TCCON) according to our model based coincidence criterion which is described in chapter 4. For the Fraunhofer setup the filter criteria are more relaxed so that the total amount of spectra used in this setup sums up to roughly 7.6 mio spectra from which roughly 2.7 mio are measured over land.

For the correction procedure two data sets were used, one contains all Antarctica and Ocean glint data and one is called 'upper edge' data set. The Antarctica and Ocean glint data set covers 672,416 spectra which are used for the correction of the radiance offset. The 'upper edge' data set is introduced by Butz et al. (2011, 2013) it contains 15,350 ocean glint spectra which are assumed to be measured under clear sky conditions. Generally, light path modification by scatterers in the atmosphere leads to over and underestimation of a retrieved absorbing gas if scattering is not considered by the retrieval. The ratio of over and underestimation is mainly controlled by ground scene albedo. Over the ocean any off-glint geometry has a low albedo so that in good approximation all light path enhancement is suppressed. Butz et al. (2013) discussed this effect in more detail and showed empirically how to identify the clear sky ocean glint spectra used here.

3.5. The Radiative Transfer Model

The radiative transport model (RTM) is the core of the RemoTeC algorithm. The linear vector RTM called LINTRAN was developed by Landgraf et al. (2001) and Hasekamp and Landgraf (2002). A new version LINTRAN v2.0 is reported by Schepers et al. (2014). In this study LINTRAN v1.0 provides RemoTeC with the solution of the radiative transport equation and the derivatives of the intensity field with respect to the atmospheric properties of interest.

3.5.1. RemoTeC uses a scalar RTM for GOSAT measurements

LINTRAN is a vector RTM meaning that it can calculate the complete stokes vector:

$$\mathbf{I} = \begin{bmatrix} I \\ Q \\ U \\ V \end{bmatrix} \tag{3.1}$$

with the four stokes parameters I, Q, U, and V. I is the total intensity and the other three parameters describe the polarization of the radiance, see for instance Chandrasekhar (1960). This enables RemoTeC to handle polarization effects, caused by scattering events in the atmosphere or in the instrument itself. As discussed in chapter 2, GOSAT measures the radiance in two perpendicular polarization directions called 'S' and 'P'. However, the instrument calibration was performed with unpolarized light, jeopardizing the calculation of all stokes parameters. O'Brien et al. (2013) showed that in good approximation the first component of the stokes vector can be calculated from $I = S + P$ for all GOSAT retrievals. Thus, RemoTeC uses a scalar implementation of LINTRAN to retrieve GOSAT measurements in the full physics setup. However, in the Fraunhofer setup the two measurements S and P, recorded by two different detectors, are treated independently as the non-linear detector behavior is different for both detectors. The Fraunhofer retrieval is performed separately for GOSAT's S and P polarized radiance measurements. In the so-called S polarized radiance retrieval the first stokes parameter is calculated from the S polarized radiance measurements only. Accordingly, the so-called P polarized radiance retrieval is calculated from the P polarized radiance measurements only. Note that the chlorophyll fluorescence signal is in good approximation unpolarized and the separation of the polarization direction is performed only due to the two different detectors that GOSAT uses for the two measurements. The polarization itself is not subject to this retrieval approach.

3.5.2. The radiative transfer

The radiance of an electromagnetic wave at a wavelength λ is defined as the transported energy E in direction $\Omega = (\Theta, \phi)$ with the zenith angle Θ and the azimuth angle ϕ through an area A within the time t:

$$I_\lambda = \frac{\mathrm{d}E_\lambda}{\cos\theta \mathrm{d}A \mathrm{d}\Omega \mathrm{d}t \mathrm{d}\lambda} \tag{3.2}$$

Where θ denotes the angle between Ω and the normal of A. In principle, four processes contribute to the change in radiance when the wave propagates through a medium along the light path s. First, it can be absorbed by the medium where the proportionality is given by the absorption coefficient β_a which is the product of the number of particles n and their absorption cross section σ_a. Second, it can be enhanced by thermal emission of the medium determined by the temperature depending Plank function B_T and the emission coefficient β_{em}. Here, the atmosphere is assumed to be in thermodynamic equilibrium, so that emission equals absorption. This is known as Kirchhoff's law. Third, the radiance can be scattered out of the direction of the beam according to the scattering coefficient β_s which is again defined equivalent to β_a. Fourth, the radiance can be enhanced by light scattered into the direction Ω out of all other directions Ω'. Summing these processes up the radiative transport equation (RTE) in its general form is given by

$$\frac{\mathrm{d}I_\lambda}{\mathrm{d}s} = -\beta_a I_\lambda + \beta_a B_T - \beta_s I_\lambda + \frac{\beta_s}{4\pi}\int_\Omega P(\Omega, \Omega') I_\lambda(\Omega') \mathrm{d}\Omega', \tag{3.3}$$

where the phase function $P(\Omega, \Omega')$ represents the probability of light scattered from direction Ω' into direction Ω. To obtain the RTE for the plane-parallel atmosphere, the extinction coefficient is defined by $\beta_e = \beta_a + \beta_s$, the single scattering albedo is defined by $\widetilde{\omega} = \frac{\beta_s}{\beta_e}$, and the total optical thickness τ at a height z is defined as

$$\tau(z) = -\int_z^{\mathrm{TOA}} \beta_e(z') dz', \tag{3.4}$$

where $z = \mu s$ and $\mu = \cos\Theta$. Using these definitions, the RTE for the plane-parallel atmosphere is given by

$$\mu \frac{\mathrm{d}I_\lambda}{\mathrm{d}\tau} = I_\lambda - J, \tag{3.5}$$

where $J = (1 - \widetilde{\omega}) B_T + \frac{\widetilde{\omega}}{4\pi}\int_\Omega P(\Omega, \Omega') I_\lambda(\Omega') \mathrm{d}\Omega'$ is the so-called source function and $\mathrm{d}\tau = -\mu \beta_e \mathrm{d}s$. An illustration of the chosen coordinates and the plane-parallel atmosphere is shown in figure 3.4. The radiation in the Earth's atmosphere can be separated by its wavelength into two regimes. One that has wavelengths longer than 4 µm where the thermal emission from the Earth's surface and atmosphere dominates the energy budget and one with wavelengths shorter than 4 µm where the solar radiation dominates. As GOSAT measures a wavelength interval ranging from roughly 0.7 µm to 2.1 µm, thermal emission can be omitted in good approximation. A detailed discussion of the atmospheric radiative transfer can be found for instance in Chandrasekhar (1960) or Liou (2002).

3.5.3. Solving the radiative transfer equation

Equation 3.5 can be solved by multiplying $e^{-\frac{\tau}{\mu}}$ and using partial integration:

$$I_\lambda(0, \Omega) = I_\lambda(\tau^*, \Omega) e^{-\frac{\tau^*}{\mu}} + \int_0^{\tau^*} J(\tau) e^{-\frac{\tau}{\mu}} \frac{\mathrm{d}\tau}{\mu} \tag{3.6}$$

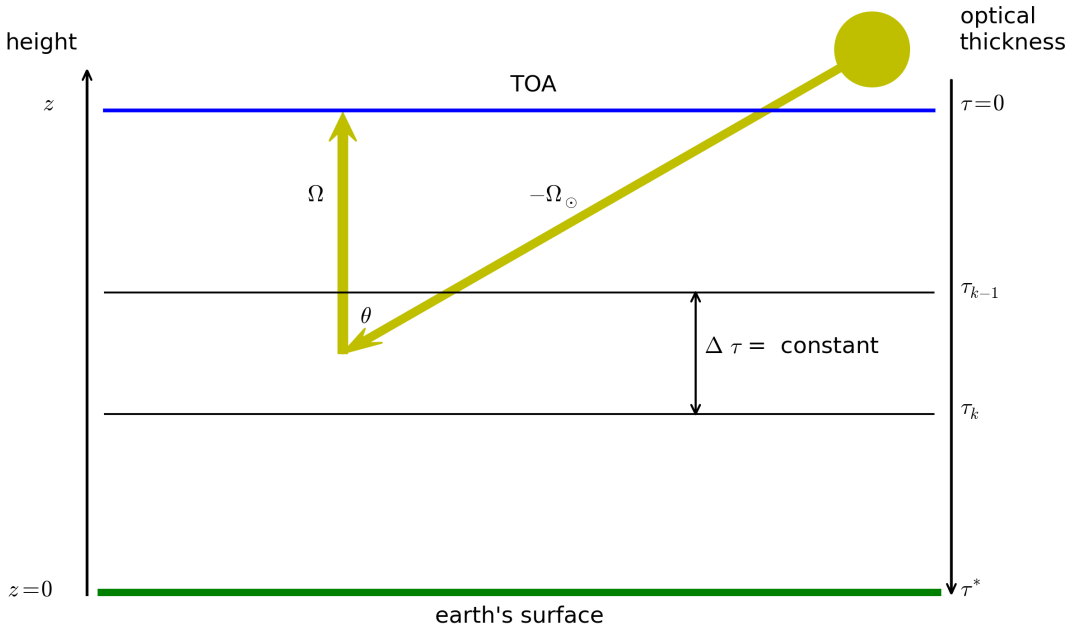

Figure 3.4.: The plane-parallel atmosphere. This scheme of the atmosphere illustrates the chosen coordinates and the layer splitting nomenclature. The solid angles Ω and -$\Omega_\odot$ denote the direction of the scattered and incident beam, respectively. θ is the scattering angle. The height coordinate τ is zero at the top of the atmosphere (TOA) and increases to τ^* at the Earth's surface. The atmosphere is divided into layers with constant τ from the upper to the lower boundary of the layer. Within each layer the single scattering albedo and the phase function are assumed to be constant.

This solution yields the upward directed monochromatic radiance at the TOA $I_\lambda(0, \mu, \phi)$ depending on the radiance at the Earth's surface $I_\lambda(\tau^*, \mu, \phi)$ reduced by the transmittance $t = e^{-\frac{\tau^*}{\mu}}$ and enhanced by the sources integrated along the light path $\int_0^{\tau^*} J(\tau) e^{-\frac{\tau}{\mu}} \frac{\mathrm{d}\tau}{\mu}$. The latter prohibits a straight forward calculation of the right side of equation 3.6. If $J = 0$ in equation 3.6, the extinction of the radiance would be only driven by the optical thickness. This case is called Beer-Lambert law. As the dominating light source in the Earth's atmosphere is the solar flux $F_\odot$ under the solid angle $-\Omega_\odot$, the radiance that is reflected by the Earth's surface is given by

$$I_\lambda(\tau^*, \mu, \phi) = \frac{A}{\pi} F_\odot \mu_\odot e^{-\frac{\tau^*}{\mu_\odot}}, \tag{3.7}$$

where A denotes the albedo. The source function can be split into a single scattering part and a multiple scattering part such that $J = J_{ss} + J_{ms}$ and is given by:

$$\int_0^{\tau^*} J(\tau) e^{-\frac{\tau}{\mu}} \frac{\mathrm{d}\tau}{\mu} = \int_0^{\tau^*} \frac{\widetilde{\omega}(\tau)}{4\pi} F_\odot P(\tau, \Omega, -\Omega_\odot) e^{-\frac{\tau}{\mu_\odot}} e^{-\frac{\tau}{\mu}} \frac{\mathrm{d}\tau}{\mu} + \tag{3.8}$$

$$\int_0^{\tau^*} \int_0^{2\pi} \int_{-1}^{1} \frac{\widetilde{\omega}(\tau)}{4\pi\mu} I(\tau, \mu', \phi') P(\tau, \mu, \phi, \mu', \phi') e^{-\frac{\tau}{\mu'}} \mathrm{d}\tau \mathrm{d}\mu' \mathrm{d}\phi' \tag{3.9}$$

The dependence on the height coordinate τ is treated by splitting the atmosphere in K layers of homogeneous optical thickness as indicated in figure 3.4.

The μ dependence in the multiple scattering part is handled by splitting the directions into M streams. The remaining ϕ dependence is handled with a Fourier expansion in N orthogonal Legendre polynomials. RemoTeC solves the resulting system of equations with a Gauss-Seidel iteration technique for $K = 36$ layers, $M = 16$ streams, and $N = 900$ Fourier components. See Schepers et al. (2014) and references therein.

3.5.4. Calculating the derivatives of the radiance

RemoTeC calculates the derivatives of I by means of the so-called forward adjoint perturbation theory that requires an operational formulation of the RTE:

$$\mathbf{L}I = S, \tag{3.10}$$

where the source S determines the intensity field I and $\mathbf{L}$ is the radiative transport operator. The source S is

$$S = \mu_{\odot} F_{\odot} \delta(\tau)\delta(\Omega - \Omega_{\odot}) \tag{3.11}$$

and $\mathbf{L}$ is given by (Ustinov, 2001; Landgraf et al., 2002):

$$\mathbf{L} = \int_{4\pi} \left[\left(-\frac{\partial}{\partial \tau} + \beta_e(\tau) \right) \delta(\Omega - \widetilde{\Omega}) - \frac{\beta_s(\tau)}{4\pi} P(\tau, \widetilde{\Omega}, \Omega) - \frac{A}{\pi} \delta(\tau - \tau^*)\Theta(\mu)|\mu|\Theta(-\widetilde{\mu})|\widetilde{\mu}| \right] \mathrm{d}\widetilde{\Omega} \circ \tag{3.12}$$

Note that the boundary conditions here are chosen such that the surface reflection is part of the transport operator: $I(0, -\Omega) = 0$ and $I(\tau^*, \Omega) = 0$. The observables (e.g. Flux, radiance, etc.) are calculated by the inner product:

$$\mathbf{O} = \langle R|I \rangle = \int_0^{\tau^*} \int_{4\pi} RI \mathrm{d}\tau \mathrm{d}\Omega, \tag{3.13}$$

where R is the response function. Setting the response function $R = \delta(\tau)\mu\Theta(\mu)$ one can calculate the upward directed flux at the TOA:

$$\mathbf{O} = \int_0^{2\pi} \int_0^1 \mu I(0, \mu, \phi) \mathrm{d}\mu \mathrm{d}\phi = F^{\uparrow}(\tau = 0) \tag{3.14}$$

For a convenient calculation of the derivatives, the pseudo forward RTE is defined by:

$$\mathbf{L}_{\Psi}\Psi = S_{\Psi}, \tag{3.15}$$

where $S_{\Psi}(\tau, \Omega) = R(\tau, -\Omega)$. In the scalar case $\mathbf{L}_{\Psi} = \mathbf{L}$ and $\Psi(\tau, \Omega) = I^{\dagger}(\tau, -\Omega)$. $\Psi(\tau, \Omega)$ is called importance because no light from the point (τ, Ω) has any influence on the measurement of $\mathbf{O}$ if $\Psi(\tau, \Omega)$ is zero.

The observables $\mathbf{O}$ depend on the atmospheric state and can be calculated using perturbation theory (Ustinov, 1991; Walter et al., 2004):

$$\mathbf{O}(x) = \mathbf{O}(x_0) + \left\langle I^{\dagger}(\tau, \Omega) \middle| \Delta \mathbf{L} I \right\rangle + \left\langle I^{\dagger}(\tau, \Omega) \middle| \Delta S \right\rangle + O(\Delta x^2), \tag{3.16}$$

with $\Delta\mathbf{L}$ and $\Delta\mathbf{S}$ denoting the changes in $\mathbf{L}$ and $\mathbf{S}$ and $x = x_0 + \Delta x$, where x_0 is an unperturbed atmospheric state parameter. Accordingly, the derivative of the observable $\mathbf{O}$ with respect to x is given in first order approximation by:

$$\frac{\partial \mathbf{O}(x)}{\partial x} = -\left\langle I^{\dagger}(\tau, \Omega) \middle| \frac{\partial \mathbf{L}}{\partial x} I \right\rangle + \left\langle I^{\dagger}(\tau, \Omega) \middle| \frac{\partial S}{\partial x} \right\rangle \tag{3.17}$$

Solutions of equation 3.17, for instance, for absorbing trace gas profiles are calculated by Landgraf et al. (2001); Hasekamp and Landgraf (2002), for surface properties by Landgraf et al. (2002), and for aerosol properties by Hasekamp and Landgraf (2005). All these publications deal with the first term on the right hand side of equation 3.17 as the second term is zero for the mentioned atmospheric parameters. This study extends the source of the RTM causing a non vanishing second term of equation 3.17. This is discussed in section 5.2.

3.6. The inversion scheme

To retrieve information about the atmospheric state, an inversion scheme is needed. Subsection 3.6.1 gives an overview on prevalent inversion methods used for atmospheric retrievals. Subsection 3.6.2 discusses a sensitivity study resulting in an improved setup of the RemoTeC inversion setup.

3.6.1. The prevalent inversion methods

An atmospheric inversion is a method to retrieve the target quantities from measurements. In particular, the inversions described here retrieve the atmospheric abundance of CO_2 and CH_4 from spectroscopic measurements. Formally, the measurements are linked to the atmospheric state with the equation

$$\vec{y} = \vec{F}_{true}(\vec{x}_{true}) + \vec{\epsilon}_y, \tag{3.18}$$

where $\vec{y}$ contains all measurements, $\vec{\epsilon}_y$ denotes the measurement errors, $\vec{x}_{true}$ is the atmospheric state and the forward model $\vec{F}_{true}$ represents the involved physical processes. As the measurements are radiances, $\vec{F}_{true}$ contains the radiance source and the radiative transport. Section 3.5 presents the forward model $\vec{F}$ that RemoTeC uses. It is a compromise between accuracy and computational cost. When using this forward model, equation 3.18 changes to

$$\vec{y} = \vec{F}(\vec{x}, \vec{b}) + \vec{\epsilon}_F + \vec{\epsilon}_y, \tag{3.19}$$

where $\vec{\epsilon}_F$ denotes the introduced forward model errors, and $\vec{x}$ and $\vec{b}$ represent the parametrized atmosphere. $\vec{b}$ contains the auxiliary parameters that are known to sufficient accuracy by external information sources. For instance, these are temperature profiles or oxygen concentration. Finally, $\vec{x}$ contains the parameters which the measurements contain information about and that are needed to obtain best accuracy in the target retrieval.

A Taylor expansion around $\vec{x}_0$ linearizes $\vec{F}(\vec{x}, \vec{b})$:

$$\vec{F}(\vec{x}, \vec{b}) = \vec{F}(\vec{x}_0, \vec{b}) + \mathbf{K}(\vec{x} - \vec{x}_0) + O(\vec{x}^2), \tag{3.20}$$

where $\mathbf{K} = \frac{\partial \vec{F}}{\partial \vec{x}}$ is the Jacobian matrix and $O(\vec{x}^2)$ are terms of higher order which are neglected in the linear approximation. For convenience, the errors and the auxiliary parameters b are reconsidered after solving the problem.

The formal solution for $\vec{x}$ of the problem $\vec{y} = \vec{F}(\vec{x}_0) + \mathbf{K}(\vec{x} - \vec{x}_0)$ would be

$$\vec{x} = \vec{x}_0 + \mathbf{K}^{-1}\left(\vec{y} - \vec{F}(\vec{x}_0)\right). \tag{3.21}$$

This is solvable if $\mathbf{K}$ is quadratic and all rows are linearly independent. In practice, that is not the case. This kind of problem is called ill posed. Subsequently, the inversion scheme needs a more sophisticated approach. Moreover, it is necessary to handle different information content and uncertainties in the measurements.

Assuming Gaussian distribution of the measurements, the probability $P(\vec{y}|\vec{x})$ of measuring $\vec{y}$ when the expected value is $\vec{F}(\vec{x})$ is given by

$$P(\vec{y}|\vec{x}) = \frac{1}{|\mathbf{S}_y|^{\frac{1}{2}}\sqrt{2\pi}^N} \exp\left[-\frac{1}{2}\underbrace{\mathbf{S}_y^{-\frac{1}{2}}(\vec{y}-\vec{F}(\vec{x}))^2}_{\chi^2}\right], \tag{3.22}$$

where N denotes the number of elements in $\vec{y}$ and $\mathbf{S}_y$ is the measurement error covariance. Having a set of measurements, one can maximize $P(\vec{y}|\vec{x})$ to estimate the most likely state $\vec{x}$ such that $\vec{F}(\vec{x})$ is consistent with the set of measurements $\vec{y}$. Maximizing P means to minimize the cost function

$$\chi^2 = \mathbf{S}_y^{-\frac{1}{2}}(\vec{y}-\vec{F}(\vec{x}))^2 \tag{3.23}$$

$$= (\vec{y}-\vec{F}(\vec{x}_0)-\mathbf{K}(\vec{x}-\vec{x}_0))^T\mathbf{S}_y^{-1}(\vec{y}-\vec{F}(\vec{x}_0)-\mathbf{K}(\vec{x}-\vec{x}_0)) \tag{3.24}$$

This χ^2 method or maximum likelihood method leads to an estimate of the atmospheric state $\hat{\vec{x}}$:

$$\hat{\vec{x}} = \vec{x}_0 + (\mathbf{K}^T\mathbf{S}_y^{-1}\mathbf{K})^{-1}\mathbf{K}^T\mathbf{S}_y^{-1}(\vec{y}-\vec{F}(\vec{x}_0)). \tag{3.25}$$

Using Bayes theorem, it is possible to calculate the probability $P(\vec{x}|\vec{y})$ of having an atmospheric state $\vec{x}$ given the measurement $\vec{y}$. It is given by

$$P(\vec{y}|\vec{x}) = \frac{P(\vec{x}|\vec{y})P(\vec{x})}{P(\vec{y})}. \tag{3.26}$$

Where $P(\vec{x})$ is the prior possibility density function of the state $\vec{x}$ and $P(\vec{y})$ is the prior possibility density function of the measurement, which in the scope of this consideration is a normalization factor. Analogue to equation 3.22 $P(\vec{x})$ is given by

$$P(\vec{x}) = \frac{1}{|\mathbf{S}_a|^{\frac{1}{2}}\sqrt{2\pi}^N} \exp\left[-\frac{1}{2}\mathbf{S}_a^{-\frac{1}{2}}(\vec{x}-\vec{x}_a)^2\right], \tag{3.27}$$

with $\mathbf{S}_a$ denoting the a priori covariance and N being the number of elements in $\vec{x}$. $\vec{x}_a$ contains a priori information about the atmospheric state. It is convenient to choose $\vec{x}_a$ as the point of expansion for the Taylor series from equation 3.20. Following the procedure from equation 3.22 to 3.25, the estimate of the atmospheric state $\hat{\vec{x}}$ in this optimal estimation approach is

$$\hat{\vec{x}} = \vec{x}_a + (\underbrace{\mathbf{K}^T\mathbf{S}_y^{-1}\mathbf{K}+\mathbf{S}_a^{-1}}_{\mathbf{S}_x})^{-1}\mathbf{K}^T\mathbf{S}_y^{-1}(\vec{y}-\vec{F}(\vec{x}_a)), \tag{3.28}$$

where $\mathbf{S}_x$ is the a posteriori error covariance matrix, containing the variances $\sigma(x_i) = \sqrt{\mathbf{S}_{x,ii}}$. Chapter 6 uses the error correlation coefficients $\rho(x_{ij}) = \frac{\mathbf{S}_{x,ij}}{\sigma(x_i)\sigma(x_j)}$. The equations 3.18 and 3.19 can be used to rearrange $\hat{\vec{x}}$ such that different error sources are quantified:

$$\hat{\vec{x}} = \vec{x}_a + \underbrace{\mathbf{GK}}_{\mathbf{A}}(\vec{x}_{true}-\vec{x}_a) + \mathbf{G}\vec{\epsilon}_F + \mathbf{G}\vec{\epsilon}_y, \tag{3.29}$$

where $\mathbf{G} = \mathbf{S}_x^{-1}\mathbf{K}^T\mathbf{S}_y^{-1}$ is the gain matrix and $\mathbf{A} = \mathbf{GK}$ is the averaging kernel. Both matrices are used for the retrieval characterization. The measurement noise error is $\mathbf{G}\vec{\epsilon}_y$,

see chapter 4 for quantitative values. The averaging kernel provides the information content of a measurement. Especially, the trace of the averaging kernel of a target gas profile $tr(\mathbf{A})$ equals the amount of independent information in this profile. This is called degrees of freedom for signal (DFS). More detail about the different inversion methods can be found in Rodgers et al. (2000).

To make best use of the a priori information and to use most information from the measurements, RemoTeC uses the Philipps-Tikhonov retrieval regularization. Hasekamp and Landgraf (2001) present a detailed description of its implementation in RemoTeC and a validation of this approach. The basic idea is to find the atmospheric state $\hat{\vec{x}}$ that is not only consistent with the measurements but also a) is the most realistic one and b) contains most information from the measurement. Following the optimal estimation procedure described above, this is achieved by substituting the inverse of the a priori covariance matrix $\mathbf{S}_a^{-1}$ by another matrix $\gamma^2\mathbf{H}$ such that the cost function is given by:

$$\|(y - F(x))^T\mathbf{S}_y^{-1}(y - F(x))\| + \|\gamma^2(x - x_a)^T\mathbf{H}(x - x_a)\|, \tag{3.30}$$

where the regularization parameter γ determines the relative weight of the two terms. The $\hat{\vec{x}}$ that minimizes this cost function is

$$\hat{\vec{x}} = \vec{x}_a + (\mathbf{K}^T\mathbf{S}_y^{-1}\mathbf{K} + \gamma^2\mathbf{H})^{-1}\mathbf{K}^T\mathbf{S}_y^{-1}(\vec{y} - \vec{F}(\vec{x}_a)). \tag{3.31}$$

For different parameters, RemoTeC realizes three different representations of $\mathbf{H}$. The simplest representation is to set $\mathbf{H} = \mathbf{0}$. This means the retrieval is performed without any constraint which is the maximum likelihood approach, see equation 3.25. RemoTeC uses this representation for all parameters except the target gas concentrations and the aerosol parameters. By choosing $\mathbf{H} = \mathbf{L}^T\mathbf{L}$, with $\mathbf{L} = \mathbf{1}$ the regularization term constrains the measurement term to the a priori state vector. This is called the 0^{th} order Phillips-Tikhonov retrieval. The 1^{st} order Phillips-Tikhonov retrieval chooses $\mathbf{L}$ to be the first order difference operator, so in case of a target gas profile the regularization term constrains the measurement term to the profile shape of the a priori state vector.

Besides $\mathbf{H}$, γ needs to be chosen. The so-called L-curve method provides an objective criterion for choosing γ. When plotting the regularization term over the measurement term for different γ's a L-shaped curve is the result. The γ corresponding to the kink of this L-shaped curve is the optimal one to minimize equation 3.30, see for instance Hasekamp and Landgraf (2001).

3.6.2. Improved Phillips-Tikhonov setup for RemoTeC

RemoTeC used to use the 0^{th} order Phillips-Tikhonov retrieval combined with a γ estimated for each spectrum via the L-curve method for the target gas and the aerosol retrieval. This retrieval setup is called 'PT' retrieval. A sensitivity study in the scope of this work showed that the scatter in the XCO_2 record is substantially reduced with a modified regularization setup.

The sensitivity study used roughly two years of GOSAT data that where available at that time. These GOSAT soundings where compared to six TCCON[2] stations with a simple coincidence criterion based on geolocation and time. For the illustration of the impact of the regularization, this chapter presents a substantially enhanced data set of 40

[2]The Total Carbon Column Observing Network (TCCON) is a network of ground-based FTIR spectrometers which is used to validate satellite based CO_2 retrievals, see chapter 4.

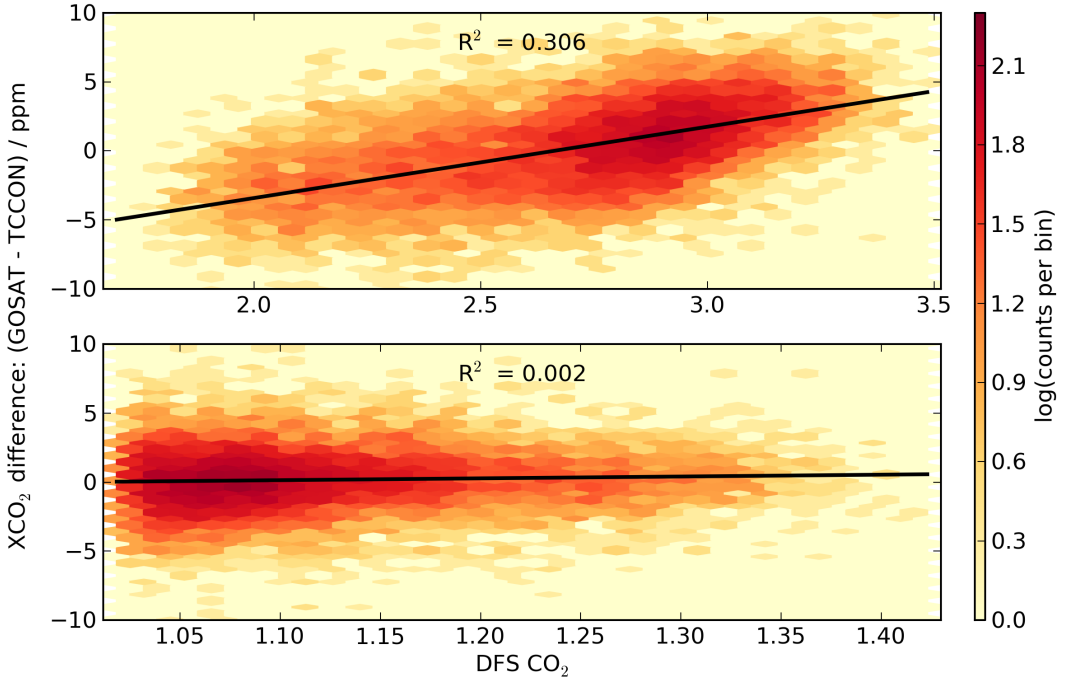

Figure 3.5.: XCO_2 difference between GOSAT and TCCON correlated to DFS for CO_2. The two dimensional histogram shows the single measurement differences of the GOSAT and TCCON soundings. The top panel contains the GOSAT data set which is retrieved with the former 0^{th} order Phillips-Tikhonov setup. The lower panel contains the new 'ad hoc' regularization method. The black line represents a linear regression. The corresponding Pearson correlation coefficient R^2 is given in each panel. The data set contains all GOSAT measurements within a 40 month time period that are coincident with measurements observed from nine TCCON stations, see chapter 4.

month GOSAT soundings compared to nine TCCON stations identified with a sophisticated model based coincidence criterion described in chapter 4. This data set is processed with a RemoTeC version using the former regularization setup but containing several other updates included in the RemoTeC version discussed in this work. These updates are for instance finer resolved meteorological data bases and some changes in the state vector parametrization. However, the filter setup of the used RemoTeC version is not optimized for the former regularization setup leading to a slightly pessimistic performance.

Figure 3.5 show the GOSAT XCO_2 retrieval difference with respect to coincident TCCON soundings in correlation with DFS for CO_2 for two different retrieval setups. The upper panel of figure 3.5 shows that the range of DFS for CO_2 is roughly between 2.0 and 3.5 for the former PT retrieval. These are more DFS than expected for the measurement sensitivity. Thus, the sensitivity study tested a stricter retrieval regularization that decreases the DFS and thereby decreases the measurement noise error. The result is shown in the lower panel of figure 3.5.

This was realized with a RemoTeC setup that keeps using the 0^{th} order Phillips-Tikhonov retrieval for the aerosol parameters but used the 1^{st} order Phillips-Tikhonov retrieval for the target gas profiles. Unfortunately, the L-curve does not have such a clear kink in this setup, causing the L-curve method to fail in choosing an appropriate γ for each individual

spectrum. Consequently, the γ is chosen ad hoc such that the DFS for the complete data set ranges from 1 to 1.4 which is expected to suit the measurement height sensitivity.

This inversion scheme substantially reduces the scatter in the RemoTeC XCO_2 record and has a minor positive impact on the RemoTeC XCH_4 record. The scatter is the standard deviation of the single measurement difference of coincident GOSAT and TCCON soundings. This reduced scatter is illustrated by four XCO_2 and XCH_4 time series at the Lamont TCCON site for the former PT retrieval scheme and the new retrieval scheme called 'ad hoc' retrieval. The overall statistics for the chosen setups here yields a CO_2 scatter reduction from 2.79 ppm (PT) to 2.0 ppm (ad hoc) which is somewhat pessimistic for the PT setup due to the unoptimized filters.

The new ad hoc inversion scheme is reported by Guerlet et al. (2013b) and used for instance by Guerlet et al. (2013a) and several inversion studies, e.g. Basu et al. (2014); Reuter et al. (2014).

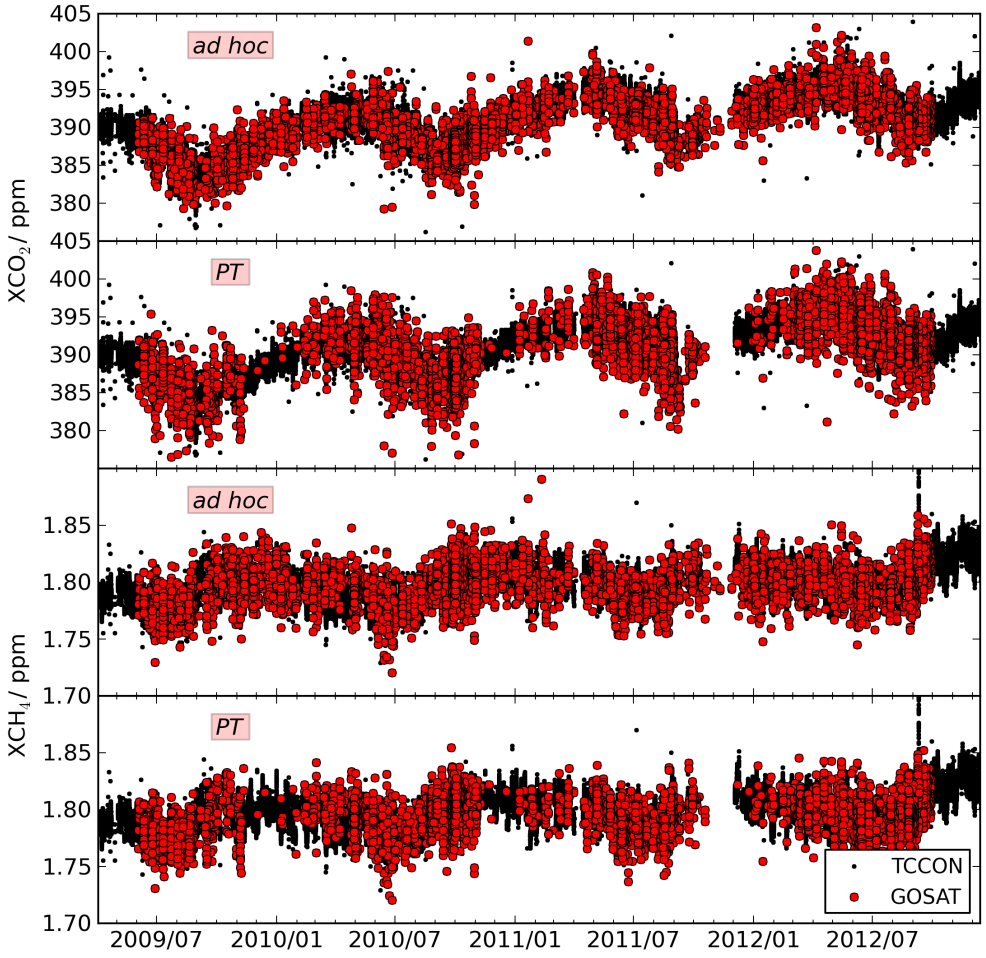

Figure 3.6.: XCO_2 and XCH_4 time series around the TCCON site Lamont (USA) for two RemoTeC inversion setups in the upper two and lower two panels, respectively. Shown are all TCCON soundings (black) within the regarded time period and all collocated GOSAT soundings (red). The respective upper panels contain the time series of the ad hoc inversion scheme whereas the respective lower panels show the PT inversion setup. Note that the filters are not optimized for the former PT inversion setup which might cause its winter data gap. Chapter 4 gives more detail for the ad hoc data set and describes the measurement collocation criterion.

4. RemoTeC full physics baseline performance

The previous chapters introduced the greenhouse gases CO_2 and CH_4 and their spectroscopic measurements with the GOSAT satellite exhibiting issues in the O_2 A-band measurements. Further, the RemoTeC retrieval algorithm was presented. This chapter deals with the full physics RemoTeC XCO_2 and XCH_4 retrieval which is referred to as Baserun in this study. In particular, section 4.1 compares the Baserun's accuracy and precision against the Total Carbon Column Observing Network (TCCON) and thereby gives an overview of quality checks applied to evaluate RemoTeC setups. In addition, this chapter discusses the possibility to exclude the O_2 A-band from the retrieval as suggested by Butz et al. (2009) in section 4.2.

4.1. Validation

This section describes the validation source in subsection 4.1.1, the applied coincidence criteria in subsection 4.1.2, the quality yard sticks in subsection 4.1.3, the bias correction in subsection 4.1.4, and, finally, in subsection 4.1.5 the validation limitations.

4.1.1. TCCON

TCCON is a network of ground-based FTIR spectrometers providing high precision measurements of the trace gases CO_2, CO, N_2O, CH_4, H_2O, HDO, and HF (Wunch et al., 2011a). TCCON stations are inter calibrated among each other and absolutely calibrated against airborne flask measurements. This makes TCCON a widely used validation source for GOSAT XCO_2 and XCH_4 measurements (Wunch et al., 2011b; Morino et al., 2011; Parker et al., 2011; Guerlet et al., 2013b; Nguyen et al., 2014) and for comparisons between different retrieval concepts, see for example O'Dell et al. (2012); Crisp et al. (2012); Oshchepkov et al. (2013).

The TCCON network currently comprises roughly 20 sites from which nine stations are chosen as validation sites in this study. For instance, the Lamont (USA) TCCON station provides measurements for the complete regarded time period, whereas some stations, for

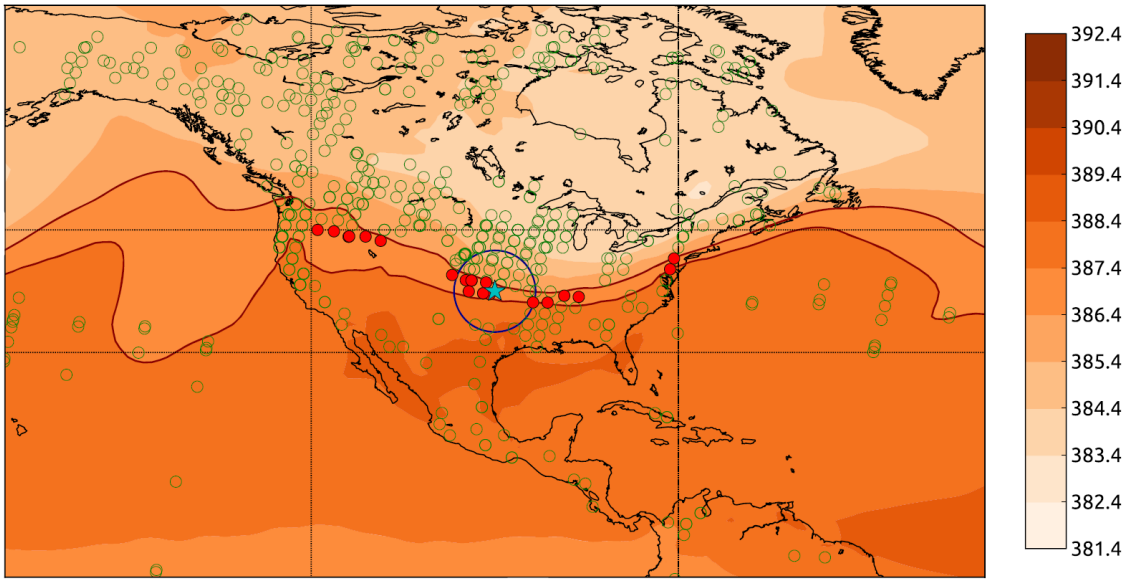

Figure 4.1.: This illustration of the current RemoTeC coincidence criterion for GOSAT and TCCON soundings is taken from Guerlet et al. (2013b). The color scale indicates modeled XCO_2 concentrations in ppm around the TCCON station Lamont (blue star). The filled red circles show collocated GOSAT soundings whereas the green circles show non-collocated GOSAT soundings. The dark blue circle around Lamont includes all soundings within a 5° latitude or longitude distance.

instance Karlsruhe (Germany), provide measurements only in the second half of the considered time period. Sites that just yield a couple of spectra suitable for validation are neglected due to low statistical significance.

4.1.2. Collocation criterion

To validate the GOSAT soundings in a statistically robust way, a procedure is needed to find TCCON-GOSAT measurement pairs that are representative for each other. The optimal case would be that both measurements were probing the same airmass at the same time. Sampling the same airmass would avoid influence by local sources and sinks and in particular transport. The same sampling time is important as the diurnal cycle of for instance temperature and photosynthetically active radiation yield a diurnal cycle in the XCO_2 and XCH_4.

For each GOSAT sounding the collocation criterion decides whether there is a TCCON site that measures a representative airmass. Reported collocation criteria are for instance a spatial distance of 5° latitude or longitude radius or a rectangle with similar or larger dimension (Wunch et al., 2011b; Guerlet et al., 2013b). Further, Wunch et al. (2011b) reports an airmass temperature driven criterion regarding the temperature at a 700 hPa level. A combination of the two is discussed by Nguyen et al. (2014). Here, a sophisticated transport model based criterion is used which is reported by Guerlet et al. (2013b) and illustrated in figure 4.1.

The basic idea is that a TCCON XCO_2 measurement is representative for XCO_2 measurements in the surrounding area if both are located within the same model estimated XCO_2 field. The model estimated XCO_2 field is given on a weekly basis on a 1° by 1° latitude and longitude grid and comprises all spots with the same XCO_2 model estimate compared to

the TCCON site with an uncertainty of 0.5 ppm or less. Furthermore, the field is limited to a continuous connected area within a box around the TCCON site with the dimension 15° latitude and 50° longitude. The model used to estimate XCO_2 is described by Basu et al. (2013) and is updated with XCO_2 measurements from RemoTeC version 2.0 having only minor differences to the one compared here.

Having identified collocated measurements, the coincidence criterion checks whether both measurements were performed in a sufficiently small time interval which is typically chosen to be two hours (Wunch et al., 2011b; Guerlet et al., 2013b; Nguyen et al., 2014).

4.1.3. Quality measures

Figure 4.2 shows the collocated GOSAT XCO_2 measurements along with the TCCON measurements as time series for two TCCON sites. For the northern hemisphere station Lamont (USA) shown in the upper panel, the seasonal cycle of XCO_2 is clearly visible. The Wollongong TCCON site located in Australia, shown in the lower panel, reveals a low continuous increase in XCO_2.

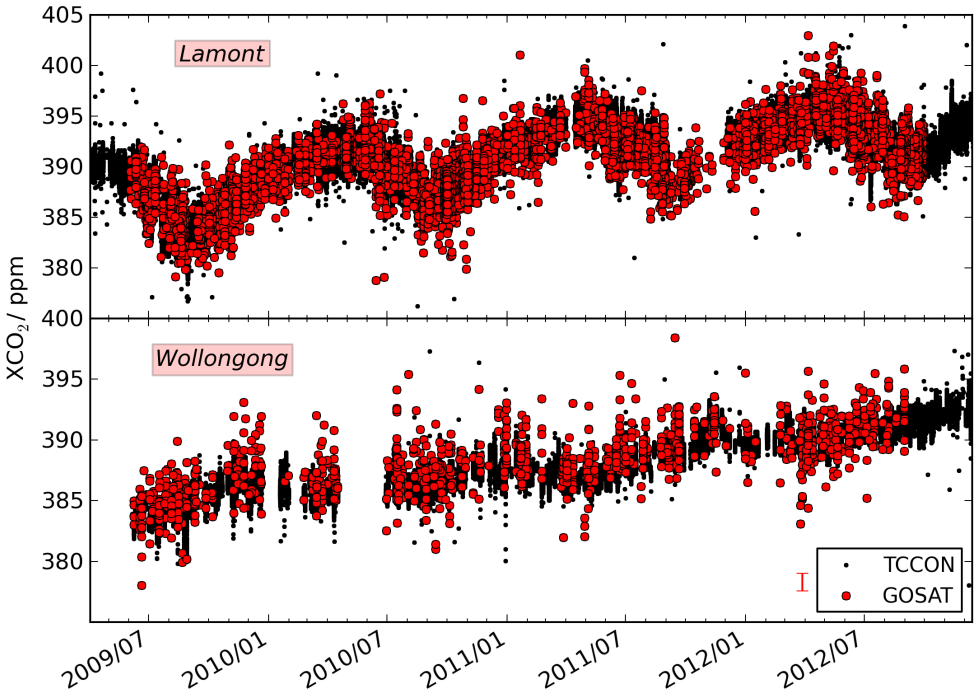

Figure 4.2.: XCO_2 time series for two TCCON stations. The strong seasonal cycle of the northern hemisphere station at Lamont (upper panel) forms a clear contrast to the southern hemisphere station at Wollongong (lower panel). The error bar next to the legend represents the noise error averaged for all TCCON collocated spectra of this dataset.

For each considered TCCON site and each coincident sounding pair, the single measurement differences called measurement errors are calculated. The station bias is the sum of these measurement errors. The standard deviation of these measurement errors is called the scatter. Table 4.1 lists these quantities per TCCON station for XCO_2 and XCH_4 along

Table 4.1.: TCCON statistics. Listed are the number of collocated and coincident spectra. The bias and the scatter of XCO_2 and XCH_4 are the sum and the standard deviation of the single measurement differences, respectively. The noise values are the averaged detector noise error estimates. The lower row lists the most important quantities to inter-compare different retrieval setups. These are the bias deviation, the total number of spectra and the mean scatter. The average is calculated with equal weight per station to avoid domination by the Lamont TCCON station.

TCCON	**Number**		**XCO_2** [ppm]			**XCH_4** [ppb]		
site	**coincident**	**collocated**	**bias**	**scatter**	**noise**	**bias**	**scatter**	**noise**
Bialystok	700	1146	-0.14	1.87	0.77	-1.20	13.54	7.77
Bremen	371	1046	-0.28	2.12	0.81	-1.57	14.50	8.04
Karlsruhe	926	1332	-0.56	2.22	0.78	0.40	13.83	7.75
Orleans	473	1391	-0.51	2.01	0.78	-0.47	13.02	7.74
Garmisch	738	1193	0.48	2.09	0.77	4.52	14.08	7.60
Park Falls	2258	2385	0.49	2.25	0.75	2.08	16.12	7.43
Lamont	4490	4678	-0.10	1.96	0.68	1.64	16.67	6.86
Darwin	1517	1517	0.10	1.71	0.54	-4.93	12.07	5.69
Wollongong	1129	1129	0.52	1.97	0.61	-0.47	15.58	6.26
	sum	sum	std. dev.	mean	mean	std. dev.	mean	mean
	12602	15817	0.40	2.02	0.72	2.50	14.38	7.24

with the averaged detector noise error estimate and the number of coincident and collocated spectra. Note that the apparently higher scatter at the Wollongong site in figure 4.2 does not appear in the coincident spectra based statistic listed in the table as the figure contains not only the coincident but all collocated spectra.

The lowest row of table 4.1 composes the key statistical quantities that serve to evaluate different RemoTeC setups against each other. The most important quantity is the deviation of the bias among the TCCON sites since it is a measure for regional biases. In addition, the total number of spectra is a very important measure as it indicates how many spectra suffer from convergence problems with the implemented inversion scheme. Further, the mean scatter, representing the single measurement precision, and the mean noise error are given. To avoid domination by single sites providing much more data than others, all quantities are first calculated per TCCON station and than further processed with equal weights.

The fact that the mean scatter is larger than the mean noise error suggests that the GOSAT retrieval includes some systematic errors. These systematic errors might correlate with geophysical or retrieval parameters and appear statistical in a geophysical data set. To identify such correlations, the differences with respect to TCCON are plotted versus a couple of geophysical and retrieval parameters and combinations of these. Figures 4.3 and 4.4 show these error correlation plots for a selection of 15 parameters for XCO_2 and XCH_4, respectively.

The upper panel, of the figures 4.3 and 4.4, respectively, shows the error correlation with the three aerosol parameters scattering optical thickness in the O_2 A-band (SOT), the aerosol layer height (height), and the aerosol size distribution parameter (α). The second panel from top contains the airmass factor and two albedo parameters. The blended albedo which is a weighted sum of the 0th order albedo in the O_2 A-band (shown separately) and the 0th order albedo in the '2 micron' band. The middle panel presents three parameters that have particular importance for this study. These are the radiance offset, the mean signal level in the O_2 A-band which are both discussed in detail in section 5.4, and the time

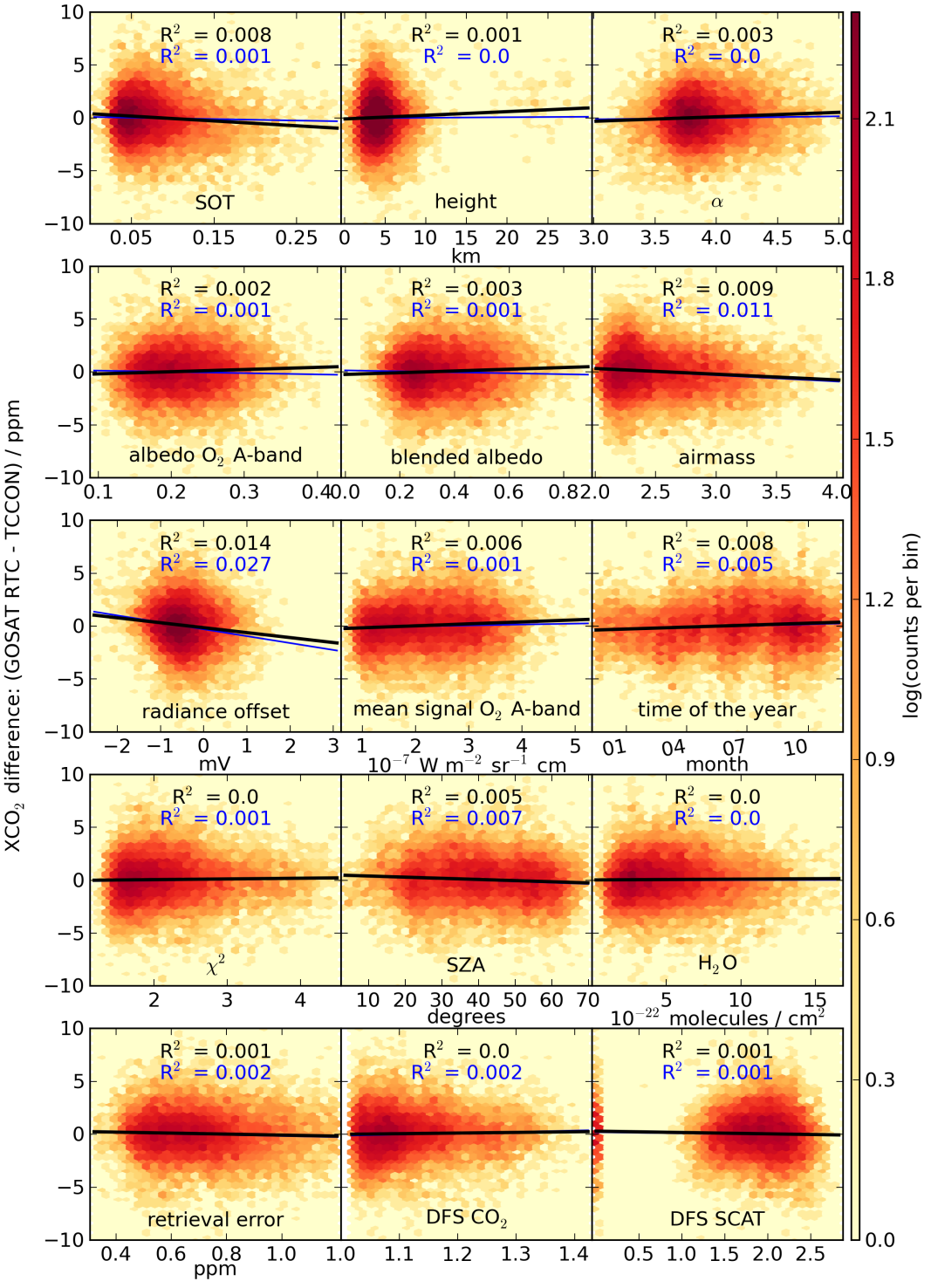

Figure 4.3.: XCO_2 correlation plots. The figure shows a two dimensional histogram of the single measurement difference between the coincident GOSAT and TCCON soundings overplotted with a linear regression (black). The Pearson correlation coefficient R^2 is given for each of the 15 parameters. The result of the bias correction from equation 4.1 is shown in blue. The histogram of the bias corrected data set is shown in the Appendix in figure A.2.

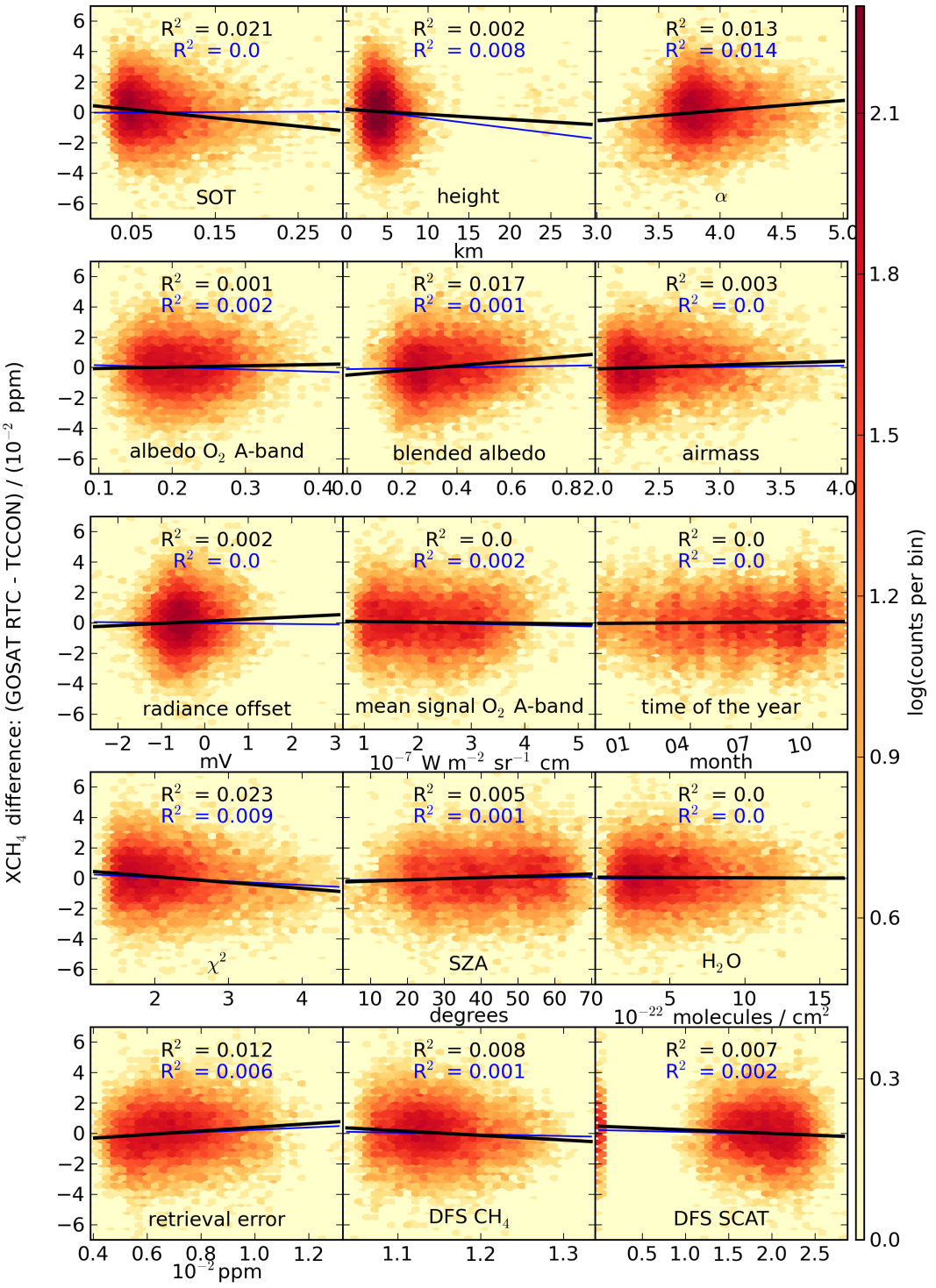

Figure 4.4.: XCH_4 correlation plots. Same illustration as in figure 4.3 but for XCH_4 instead of XCO_2. As the Pearson correlation coefficient indicates, the correlation of the Baserun's target gas abundance with geophysical or retrieval parameters is generally quite low. The result of the bias correction from equation 4.2 is shown in blue. The histogram of the bias corrected data set is shown in the Appendix in figure A.3.

of the year which could indicate seasonal errors occurring due to unaccounted chlorophyll fluorescence. The lower two panels comprise χ^2 calculated from all four retrieval windows, the solar zenith angle (SZA), the total H_2O column, the estimated retrieval noise error, and the degrees of freedom (DFS) for scattering (SCAT) and the DFS of the target gases XCO_2 and XCH_4, respectively.

4.1.4. Bias correction

The XCO_2 and XCH_4 records discussed so far are bias corrected with one global offset. This simple bias correction added 3.38 ppm to each XCO_2 value and added 12.75 ppb to each XCH_4 value. The global biases are calculated for each retrieval setup individually by a pre processing step summing up all differences to TCCON.

Having identified correlations of the XCO_2 and XCH_4 with certain parameters, a sophisticated bias correction can be applied to the data set. This is a common approach that should improve the data used in inverse source and sink models, see for instance Takagi et al. (2014).

Figures 4.3 and 4.4 showed in blue the results of the bias correction

$$\mathrm{XCO}_{2,\mathrm{BC}} = \mathrm{XCO}_2 \cdot \left(1.0057425 - \mathrm{ALB}_{\mathrm{O_2A-band}} \cdot 0.01 + \mathrm{SOT} \cdot 0.015 + \frac{1}{\alpha} \cdot 0.015\right) \quad (4.1)$$

$$\mathrm{XCH}_{4,\mathrm{BC}} = \mathrm{XCH}_4 \cdot (1.0074439 - \mathrm{ALB}_{\mathrm{blended}} \cdot 0.01 + \mathrm{SOT} \cdot 0.04) \quad (4.2)$$

where $XCO_{2,BC}$ and $XCH_{4,BC}$ are the bias corrected XCO_2 and XCH_4 records, respectively. SOT, α, the albedo in the O_2 A-band ($ALB_{O_2A-band}$), and the blended albedo ($ALB_{blended}$) are defined in subsection 4.1.3.

The three parameter based bias correction for XCO_2 reduces the error correlation for instance with the mean signal level in the O_2 A-band. However, it fails in reducing the error correlation for many parameters like the airmass factor, the time of the year, or the solar zenith angle. The two parameter based bias correction for XCH_4 effectively reduces the error correlations with geophysical parameters, for instance the airmass factor, and retrieval parameters like χ^2.

4.1.5. Limitations

The major limitation of the discussed TCCON validation is the low number or complete lack of validation spectra in many parts of the world and for many satellite measurement conditions that are challenging for space based retrievals. The southern hemisphere is covered only by two TCCON sites in Australia. Within the regarded time period no TCCON site measures in the equatorial latitudes between Darwin (Australia, 12° south) and Lamont (USA, 36° north) and no station is placed in continental Eurasia east of Bialystok (Poland, 23° east).

Especially the error correlation with geophysical parameters would be more significant if the validation range in the geophysical parameters as the ground scene albedo or aerosol load would cover most of the globally occurring variation. The limitations due to TCCON ground scene albedo coverage are discussed by Guerlet et al. (2013b).

Another limitation for a complete characterization of the data set is that many parameters other than the illustrated ones and combinations of these parameters could be investigated. The choice of parameters is experience driven.

4.2. Is it possible to avoid the O_2 A-band?

Based on a simulation study, Butz et al. (2009) proposed that a retrieval skipping the O_2 A-band and only using the 2 micron band, which comprises strong CO_2 absorption lines, could perform equally well as the full physics retrieval.

Such a concept, only considering a small spectral range, would enable retrievals with low computational cost and cheap satellite instruments observing XCO_2 with fewer optical devices and detectors than, for instance, the GOSAT instrument. Moreover, it would avoid the GOSAT retrieval problems due to the detector non-linearity in the O_2 A-band and one would not need to deal with complications such as chlorophyll fluorescence.

However, the main information on the Baserun's three aerosol parameters comes from the wide spectral range covered by the 2 micron band and the strongly absorbing O_2 A-band. When skipping the O_2 A-band, most aerosol information would come from the strongly absorbing H_2O and CO_2 lines in the 2 micron band. Accordingly, the number of retrievable aerosol parameters depends on the choice of retrieval windows.

Following the setup from Butz et al. (2009), the performance of the retrieval using only the 2 micron band was evaluated. To compensate the lower information content of a retrieval without the O_2 A-band and to maintain its retrieval quality, further retrieval setups using different retrieval window configurations were tested. Adding other windows to the retrieval setup increases the information on CO_2 via including more CO_2 absorption lines and it increases information about atmospheric scatterers by including more strong absorption lines.

Subsection 4.2.1 gives an overview on the evaluated RemoTeC setups and subsection 4.2.2 shows the results of the best setup which, however, exhibits major drawbacks compared to the Baserun.

4.2.1. Shortcut retrieval setups

Figure 4.5 gives an overview of the investigated windows. The middle panel shows the weak CO_2 absorption band which adds more information on the CO_2 concentration to the retrieval. The lower panel shows three strong CO_2 absorption bands. The window between 4800 and 4900 cm^{-1} is the same as for the Baserun. The two windows at higher wavenumbers contain more CO_2 absorption lines and, in addition, more and stronger H_2O absorption lines. See figure 2.1 for comparison with the Baserun retrieval windows illustrated for the same spectrum.

Unfortunately, the use of these retrieval windows suffer from some spectroscopic issues. The weak CO_2 absorption band around 1.6 µm is supposed to be spectroscopically consistent with the CO_2 absorption lines around 2.06 µm. However, according to Butz et al. (2013), the spectroscopic input parameters for the strong CO_2 window from 4946.0 to 5006.0 wavenumbers are spectroscopically inconsistent with the spectroscopic information for the used weak and strong CO_2 absorption bands. The CO_2 window around 1.96 µm reveals another spectroscopic issue that is a H_2O absorption line at 1.98 µm. With the used spectroscopic data bases this line causes a high residuum and thus a high χ^2. This issue remained even when using the HITRAN 2012 (Rothman et al., 2013) data base.

Due to these spectroscopic issues, both strong CO_2 windows were included in the retrieval with uncoupled CO_2, meaning that the CO_2 information from these windows is independent from the target CO_2 information. This is technically realized by setting the Jacobians

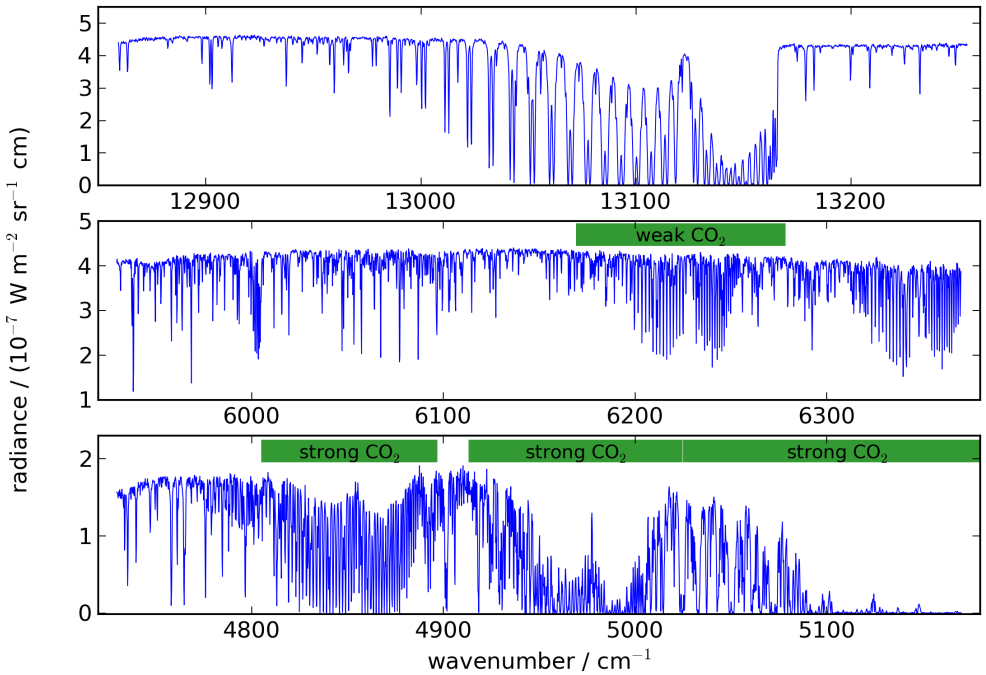

Figure 4.5.: Spectral overview of the shortcut retrieval windows. It is the same spectrum and illustration as in figure 2.1. The O_2 A-band in the upper panel is ignored. The weak CO_2 absorption band in the middle panel and the strong CO_2 absorption band in the lower panel between 4800 and 4900 cm^{-1} are the same as in the Baserun. Additionally, the investigation comprises the two strong CO_2 absorption bands at higher wavenumber in the lower panel.

of the target CO_2 in the two additional windows zero and setting the Jacobians of the interfering CO_2 in the 1.6 µm and 2.06 µm window zero.

For each retrieval setup the retrieval regularization was chosen such that the DFS CO_2 were in a proper range. Furthermore, the filters were optimized for each run individually. Finally, for each retrieval setup the statistic of the differences with respect to TCCON where used to identify the best aerosol parameterization.

4.2.2. Poor performance due to aerosol retrieval

The tested retrieval setup considering only the strong CO_2 absorption window between 4800 and 4900 cm^{-1} performs best with respect to TCCON when only the aerosol optical depth parameter is retrieved and the size distribution parameter α and the aerosol layer height remain fixed at the apriori values 3.5 and 3000 m, respectively. Unfortunately, this retrieval setup results in a high scatter of the data set and very high XCO_2 differences over the Sahara desert which typically exhibits a high aerosol load.

The best retrieval setup is the one using all four retrieval windows shown in figure 4.5. Where the CO_2 absorption lines in the two retrieval windows with wavenumbers higher than 4900 cm^{-1} are uncoupled from the ones in the two standard RemoTeC windows at 1.6 µm and 2 µm. The aerosol retrieval uses the aerosol optical depth parameter and the aerosol layer height parameter while setting the aerosol size distribution parameter $\alpha = 3.5$.

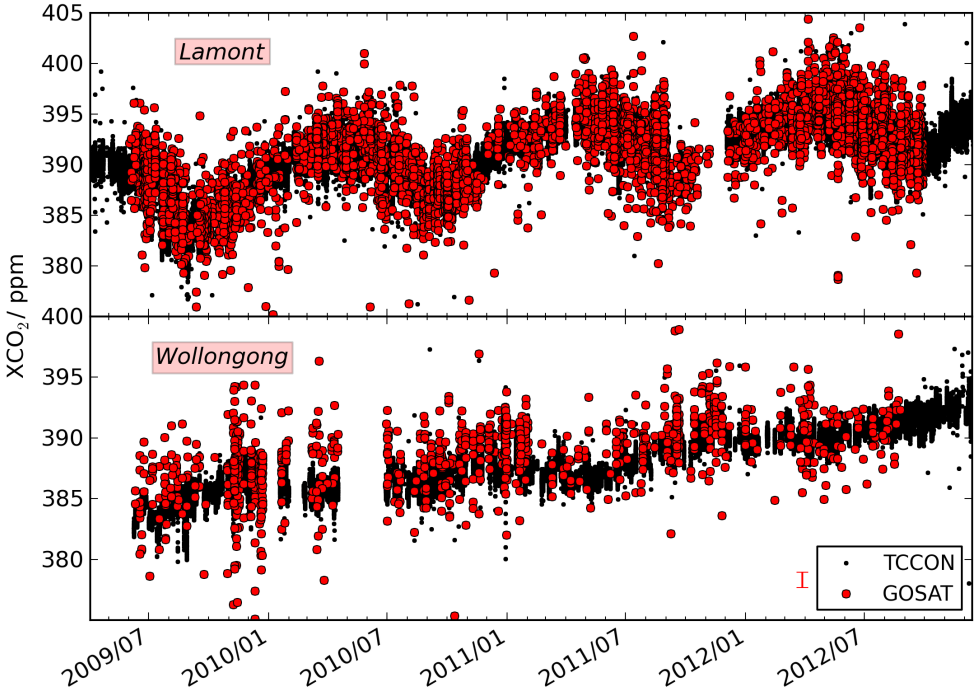

Figure 4.6.: XCO_2 time series for two TCCON stations for the best short cut setup using the four retrieval windows shown in figure 4.5. The illustration is the same as in figure 4.2 showing the results for the Baserun which has obviously less scatter.

The performance with respect to TCCON of this short cut retrieval setup is quite poor compared to the Baserun. This is briefly illustrated in figure 4.6 showing the XCO_2 time series at the two TCCON sites Lamont and Wollongong which can be directly compared to figure 4.2 and the statistics summarized in table 4.2 which can be compared to table 4.1.

TCCON	**Number**		**XCO_2** [ppm]		
site	**collocated**	**coincident**	**bias**	**scatter**	**noise**
Bialystok	1541	902	-0.17	3.06	0.71
Bremen	1442	485	-0.57	2.96	0.73
Karlsruhe	1808	1232	-1.12	3.25	0.70
Orleans	1776	610	-0.74	3.47	0.69
Garmisch	1653	1042	0.42	3.04	0.68
Park Falls	2859	2738	0.58	3.29	0.68
Lamont	4232	4027	0.30	2.82	0.57
Darwin	1817	1817	0.44	2.73	0.46
Wollongong	1013	1013	0.87	2.79	0.50
	sum	sum	std. dev.	mean	mean
	18141	13866	0.64	3.05	0.64

Table 4.2.: TCCON statistics for the short cut retrieval. The same statistical quantities are given as in table 4.1. The bias deviation among the TCCON stations and the scatter of the data set are significantly higher for the short cut record.

Figure 4.7 shows the difference between XCO_2 retrieved with the Baserun and XCO_2 retrieved with the short cut retrieval plotted versus the scattering optical thickness retrieved in the Baserun. The higher the scattering optical thickness the higher is the difference. As the Baserun performance with respect to TCCON does not reveal such high errors, this indicates that the reason for the lack in accuracy and precision of the short cut method is most likely due to unaccounted aerosol scattering in the atmosphere.

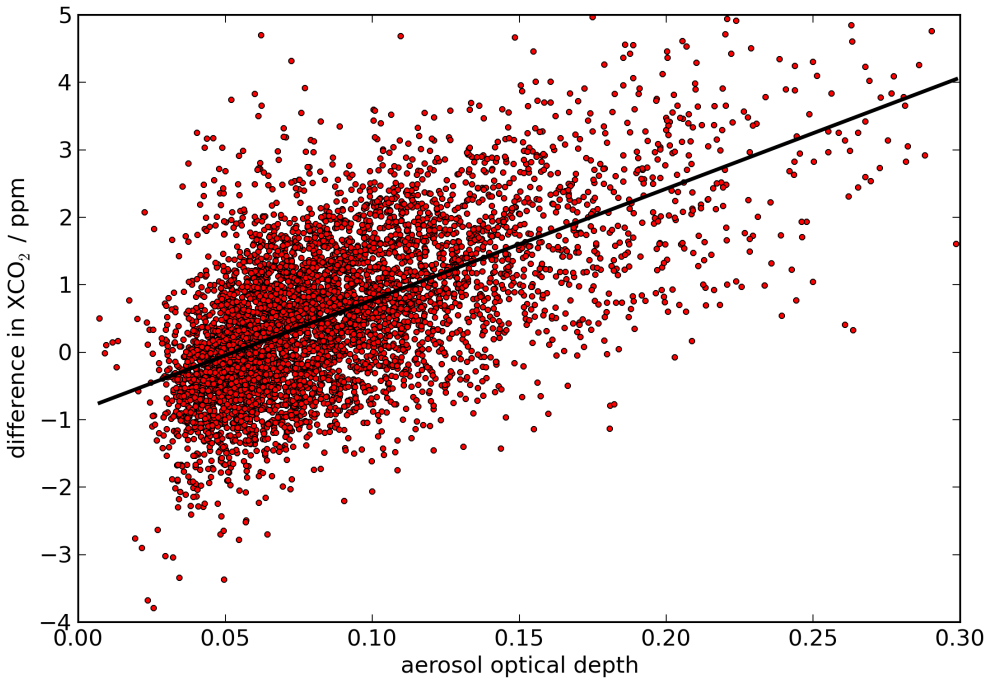

Figure 4.7.: Correlation of the XCO_2 difference (short cut - Baserun) with scattering optical thickness in O_2 A-band retrieved from the Baserun. The black line represents a linear regression.

This chapter introduced the TCCON validation concepts by applying them to the full physics RemoTeC retrieval setup. Within the regarded time period RemoTeC successfully processes roughly 12,600 TCCON coincident spectra and retrieves XCO_2 with a regional bias of 0.4 ppm and a single measurement precision of 2.0 ppm. RemoTeC retrieves XCH_4 with a regional bias of 2.5 ppb and a single measurement precision of 14.4 ppb. Generally, the differences with respect to TCCON correlate low with geophysical parameters with linear Pearson correlation coefficients R^2 typically below 0.01 and 0.02 for XCO_2 and XCH_4, respectively. Thus, the introduced bias correction has little influence on the retrieval performance. The bias correction for XCO_2 and XCH_4 is based on the correlation of the single measurement differences with respect to TCCON on the parameters albedo and scattering optical thickness. Additionally, the XCO_2 bias correction is based on the aerosol size distribution. Following the suggestion by Butz et al. (2009), this chapter discussed whether the RemoTeC retrieval could exclude the O_2 A-band. Unfortunately, the performance of all investigated setups skipping the O_2 A-band suffers from insufficient information about atmospheric aerosol scattering.

5. Retrieving chlorophyll fluorescence

The previous chapter showed that using the O_2 A-band in the full physics retrieval is crucial to account for aerosol scattering effects in the atmosphere properly. However, using GOSAT's O_2 A-band causes two issues. One issue is the detector non-linearity which in first approximation leads to a radiance offset. This issue can be addressed by a sophisticated calibration of the spectra or by retrieving a radiance offset. Hitherto, the latter approach was used by RemoTeC. However, this latter approach hampers the solution of the other issue that occurs when using the O_2 A-band in the XCO_2 and XCH_4 retrieval. This other issue is the spectrally broad chlorophyll fluorescence signal originating from plant's photosynthesis. As Frankenberg et al. (2012) showed this chlorophyll fluorescence is an error source in the full physics XCO_2 and XCH_4 retrieval if it is neglected.

This chapter gives an overview of chlorophyll fluorescence and its spectral properties in the introductory section 5.1. Section 5.2 shows the necessary changes in the radiative transport model to retrieve this chlorophyll fluorescence and introduces two concepts used here to retrieve fluorescence with their respective benefits. These concepts are called Fraunhofer concept and full physics concept. The latter is discussed in detail in chapter 6. Section 5.4 discusses how to deal with the radiance offset in the GOSAT spectra. Finally, section 5.5 examines the chlorophyll fluorescence record retrieved with the Fraunhofer concept.

5.1. Chlorophyll fluorescence

Subsection 5.1.1 introduces chlorophyll fluorescence. Subsection 5.1.2 discusses spectral signatures of the chlorophyll fluorescence and subsection 5.1.3 interfering spectral effects. Finally, subsections 5.1.4 and 5.1.5 summarize remote sensing aspects and current and future scientific applications, respectively.

5.1.1. What is chlorophyll fluorescence?

Chlorophyll is a class of color pigments found in plants, algae and some bacteria. Plants use these light absorbing color pigments to supply their photo systems PSI and PSII with energy. The pigments have two main absorption maxima corresponding to two excited states. The exact wavelengths of these absorption maxima depend on the chlorophyll type

and the physical and chemical conditions, for instance temperature and dissolver (Wellburn, 1994; Lichtenthaler and Rinderle, 1988). Typically, chlorophylls absorb in the blue spectral range from 400 to 500 nm wavelengths and in the red spectral range between 600 and 700 nm wavelengths. As a result of this, the reflected green light gives the plant leafs' typical green color.

The abrupt change in the reflectance around 700 nm wavelength is called red edge. Several remote sensing techniques use this red edge to estimate plants chlorophyll content and vegetation density (Meroni et al., 2009). Well known data sets retrieved are the leaf area index (LAI) and the normalized and enhanced vegetation index called NDVI and EVI, respectively (Tucker, 1979; Huete et al., 2002). These indices are used by precision farming, forest management, and carbon budget assessments as a measure of the plants' status and gross primary production (GPP). However, the photosynthetic efficiency is only indirectly addressed with these indices because, besides the chlorophyll content itself, GPP depends on various biogeochemical conditions, for instance, availability of photosynthetic active radiation (PAR) and water stress (Lichtenthaler and Miehe, 1997; Papageorgiou, 2004).

The plants' photo systems transform most of the excitation energy provided by the chlorophylls to chemical energy by synthesizing sugars and other biochemical products. This process extracts CO_2 molecules from the ambient air. This is the reason why it is called carbon fixation. However, a small fraction of the excitation energy dissipates into heat and another fraction fluoresces, this means photons with higher wavelength are re-emitted. In plant leafs at physiological temperatures most of the fluorescence is emitted by the 'chlorophyll a' pigment from PSII (Papageorgiou, 1975). Consequently, the fluorescence is directly linked to the energy budget of the photo systems (Baker, 2008). Hence, independently of the chlorophyll content itself the chlorophyll fluorescence provides information about the biome or the plants' state, especially photosynthetic inefficient conditions like water stress (Meroni et al., 2009; Joiner et al., 2011).

5.1.2. Spectral signature of chlorophyll fluorescence

The spectral properties of the fluorescence signal vary among the types of chlorophyll. Different plant species have a different composition of chlorophylls. In addition, the chlorophyll composition for the same species varies with geophysical and biochemical conditions. Driving parameters are the illumination, the temperature, the humidity, and the nutrient availability. Moreover, when measuring a fluorescence spectrum of a sun illuminated canopy the sampling of the plants might differ with measurement geometry. Otherwise, very simple models of the fluorescence spectra, disregarding any of the mentioned variations, are able to estimate photosynthetic activity quite robustly (Frankenberg et al., 2011a; Joiner et al., 2011; Guanter et al., 2012). Frankenberg et al. (2011a) found that the retrieved chlorophyll fluorescence correlates better with GPP than LAI or NDVI.

Figure 5.1 shows two simple fluorescence models (lower panel) around the O_2 A-band measured by GOSAT (upper panel). The light green model are two coadded Gaussians (parametrization taken from Frankenberg et al., 2011a) showing the two fluorescence maxima around 690 nm and 740 nm wavelength. The green model shows a simple linear fluorescence model in the GOSAT measurement range where the radiance at 755 nm is 1.7 times higher than the radiance at 772 nm wavelength. This ratio is empirically found to suit the global GOSAT observations best and is exactly the same as found by Frankenberg et al. (2011a), see section 5.5.

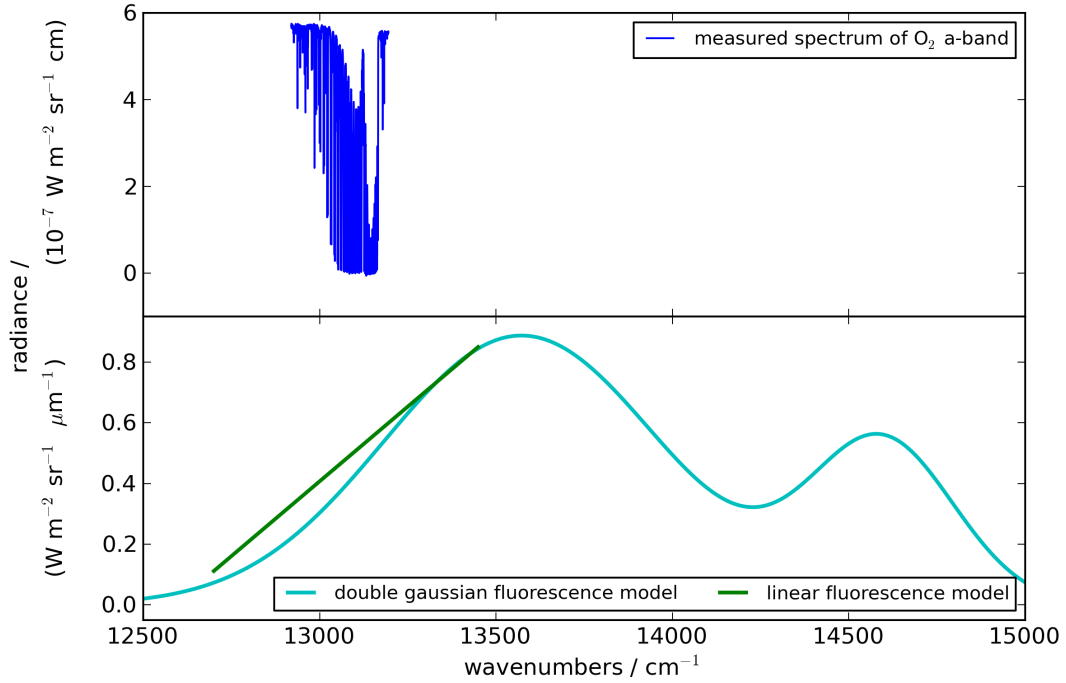

Figure 5.1.: The broad band fluorescence signal relative to the measured O_2 A-band. The upper panel shows a GOSAT O_2 A-band measurement at the top of the atmosphere. The lower panel shows two top of the canopy models of a typical European summer fluorescence signal. The green linear model is shown only in the vicinity of the measurement range. The light blue model contains the two chlorophyll fluorescence emission maxima.

The fluorescence models in figure 5.1 are given at the top of the canopy and are assumed to be isotropic and unpolarized. The fluorescence signal strength is a typical value averaged within the GOSAT footprint over Europe in summer under daylight conditions. The range of reported fluorescence radiance observed by GOSAT is typically below 1% of the back scattered solar intensity that is below 1.5 W m^{-1} sr^{-1} µm^{-1} (Frankenberg et al., 2011a; Joiner et al., 2011; Guanter et al., 2012). However, Meroni et al. (2009) found the range of published fluorescence radiance under daylight conditions to vary widely with maximum values around 17 W m^{-1} sr^{-1} µm^{-1}.

The communities of grating spectrometers and Fourier transform spectrometers use the spectral units wavelength and wavenumber, respectively. Note that this work gives the fluorescence radiance unit always as radiance at 755 nm wavelength in W m^{-1} sr^{-1} µm^{-1}. For direct comparison with current publications, the spectral unit for Fraunhofer lines, fluorescence spectra, and sometimes retrieval ranges are given in wavelength unit. However, the radiance of measured spectra, residua, derivatives etc. are given in the native GOSAT unit W m^{-1} sr^{-1} cm.

To retrieve chlorophyll fluorescence from space the radiative transfer model needs to account several aspects. The fluorescence signal passes the atmosphere once before it reaches a satellite observer. Thus, it is partially absorbed by oxygen when the satellite measures it at the top of the atmosphere. Scattering events in the atmosphere may enhance the light path of the fluorescence signal. Note that the sunlight passes the atmosphere twice and its light path may be shortened or enhanced by scattering events.

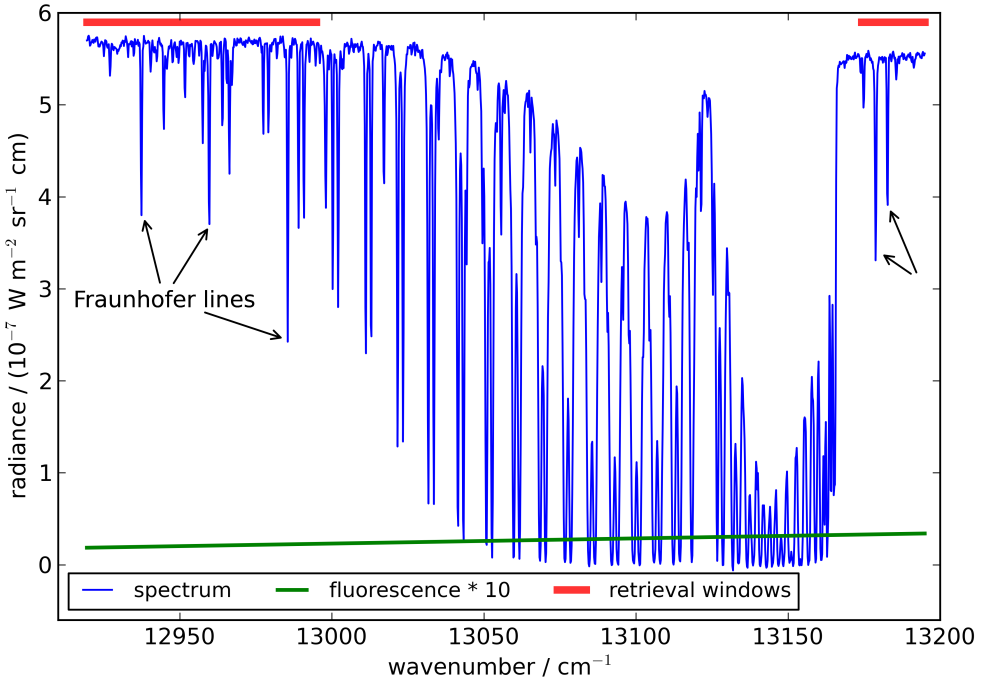

Figure 5.2.: GOSAT measurement of the O_2 a band (blue). The most pronounced Fraunhofer lines are indicated by arrows. The fluorescence radiance (green) is the linear model from figure 5.1 enhanced by a factor of 10. The two wavelength ranges indicated by the red bars represent the retrieval windows used for the chlorophyll fluorescence retrieval by this work and by Frankenberg et al. (2011b).

GOSAT's first band measurement range comprises two types of spectral features. These are the O_2 absorption lines and the Fraunhofer lines, see figure 5.2. The Fraunhofer lines are absorption lines originating from absorption processes in the outer solar atmosphere and are little influenced in the Earth's atmosphere. As discussed later in this chapter, the chlorophyll fluorescence fills these Fraunhofer lines which can be used quite effectively to retrieve chlorophyll fluorescence. The other spectral feature, the O_2 absorption, depends on the O_2 content in the atmosphere and the light path which depends crucially on molecular and particle scattering. As the O_2 concentration is quite constant in the atmosphere and is known apriori, these absorption lines constrain the aerosol parameter retrieval quite effectively.

Being broad band, the chlorophyll fluorescence radiance adds nearly the same amount of photons within and next to a telluric or solar absorption line. Relatively, this effect fills in the absorption lines. See figure 2.2 for an illustration of this effect, the impact of instrument resolution, and the noise level relative to the fluorescence signal.

5.1.3. Interfering effects

In principle, there is another spectral infilling effect that is the rotational Raman scattering. This means that inelastic scattering events alter the wavelength of the photons. As there are more photons in the continuum level of the signal, there are more photons scattered into an absorption line than out of it. Sioris et al. (2003) found that the fluorescence

signal fills in Fraunhofer lines much more efficiently than rotational Raman scattering for nadir looking satellites. Indeed, Joiner et al. (2011) found rotational Raman scattering to be not relevant for retrieving chlorophyll fluorescence using the infilling effect in the strong Fraunhofer line at 770.1 nm measured by GOSAT. For a solar zenith angle of 45° and the spectral resolution of GOSAT the effect of rotational Raman scattering is a factor 10-100 smaller than the fluorescence radiance signal (Vasilkov et al., 2012).

5.1.4. Remote sensing of chlorophyll fluorescence

Plascyk (1975) proposed to use the infilling effect of Fraunhofer lines to remotely sense the chlorophyll fluorescence radiance to detect geochemical anomalies or onsets of crop diseases. Stoll et al. (1999) proposed the fluorescence explorer satellite mission (FLEX) to provide new and interesting Earth observation data. The review by Meroni et al. (2009) gives an overview of remote sensing techniques and records.

The GOSAT satellite is the first satellite mission that provides spectra with high resolution of the Fraunhofer lines in the vicinity of the O_2 A-band. Joiner et al. (2011) presented a chlorophyll fluorescence retrieval based on a narrow retrieval range around the strong Fraunhofer line around 770.1 nm wavelength. They assumed the radiance offset and atmospheric absorption and scattering to be negligible and used a maximum likelihood inversion scheme, see section 3.6 for details about inversion schemes.

Frankenberg et al. (2012) corrected GOSAT spectra for radiance offset effects and successfully retrieved chlorophyll fluorescence using two small retrieval windows containing several Fraunhofer lines and few telluric absorption lines. See figure 5.2 for an illustration of the used retrieval windows. To model the solar spectrum, they used a non scattering radiative transfer model, neglecting atmospheric scattering events of the solar light, with an optimum estimation inversion scheme. They did a correction of the radiance offset showing a similar mean signal dependence as found in this work, which is shown in figure 5.4. However, they neglected the measurements from the P-polarized radiance, possibly, because the time dependence of these data is too strong, see figure 5.6. The fluorescence radiance was not included in the radiative transfer model itself but simply added to the modeled solar spectrum before convolving it with the instrumental line shape. They modeled the fluorescence spectrum with two slope parameters and calculated the O_2 absorption via Beer-Lambert's law (see section 3.5.2).

Guanter et al. (2012) presented a GOSAT chlorophyll fluorescence record circumventing the radiative transfer problem using an empirical method based on empirical orthogonal functions (EOF). Furthermore, spectra from the moderate spectral resolution from the SCanning Imaging Absorption spectroMeter for Atmospheric CHartographY (SCIAMACHY) satellite (Burrows et al., 1995) and the Global Ozone Monitoring Instrument 2 (GOME-2) (Munro et al., 2006) provide information about chlorophyll fluorescence as they cover a wide spectral range, as reported by Joiner et al. (2012, 2013).

5.1.5. Scientific applications

A good correlation between the fluorescence radiance and GPP is shown in Frankenberg et al. (2012) and Parazoo et al. (2013). Parazoo et al. (2013) showed that chlorophyll fluorescence can also be used as a tracer for inter annual variation in GPP. Lee et al. (2013) assessed Amazonian forest productivity and water stress using GOSAT chlorophyll

fluorescence retrievals. Guanter et al. (2014) reported that the chlorophyll fluorescence retrievals especially over agricultural regions yield higher GPP estimates potentially improving carbon cycle models.

In future, more and sophisticated measurements might enable studies on smaller scales and validate and improve models of the interaction between chlorophyll fluorescence and photosynthetic activity of plants as presented by Van der Tol et al. (2009a,b). For instance, the launched OCO-2 instrument will provide nearly 100-fold more measurements of high resolution O_2 A-band spectra than GOSAT which might allow to address regional effects (Frankenberg et al., 2014). Guanter et al. (2015) reported that the TROPOMI instrument on board Sentinel-5-Precursor has a high potential to convey valuable observations. Also the FLEX mission, if realized, might give more insight into the chlorophyll fluorescence (Stoll et al., 1999; Guanter et al., 2010).

5.2. Implementation in RemoTeC

To retrieve a chlorophyll fluorescence record, it is possible to set up a relatively simple radiative transfer model and retrieval approach, see section 5.1. However, this work aims at accounting for the chlorophyll fluorescence radiance in the XCO_2 retrieval. Thus, a physical description of the radiative transfer of the emitted fluorescence radiance is needed.

To this end, equation 3.11 from section 3.5 must be extended. The discussion in section 3.5 considered the source S to comprise only the solar radiation as source: $S = S_\odot$. This study adds a surface emitted radiance S_{Fl} to the source such that

$$S = S_\odot + S_{Fl} = \mu_\odot F_\odot \delta(\tau)\delta(\Omega - \Omega_\odot) + \delta(\tau - \tau^*)|\mu|\Theta(\mu)I_{Fl} \tag{5.1}$$

The derivative of the observable **O** with respect to the atmospheric parameter x was given in equation 3.17. Choosing the atmospheric parameter x to be the chlorophyll fluorescence ($x = I_{Fl}$), the derivative is given by:

$$\frac{\partial I(0,\Omega)}{\partial I_{Fl}} = -\left\langle I^\dagger(\tau,\Omega)\middle|\frac{\partial \mathbf{L}}{\partial I_{Fl}}I\right\rangle + \left\langle I^\dagger(\tau,\Omega)\middle|\frac{\partial S}{\partial I_{Fl}}\right\rangle \tag{5.2}$$

The chlorophyll fluorescence contributes to the source S but is not influencing the radiative transfer represented by **L**. Thus, the first term on the right hand side of equation 5.2 is zero. With $\frac{\partial S}{\partial I_{Fl}} = \delta(\tau - \tau^*)|\mu|\Theta(\mu)$ equation 5.2 yields

$$\frac{\partial I(0,\Omega)}{\partial I_{Fl}} = \left\langle I^\dagger(\tau,\Omega)\middle|\frac{\partial S}{\partial I_{Fl}}\right\rangle \tag{5.3}$$

$$= \int_0^{\tau^*}\int_{4\pi} I^\dagger(\tau,\Omega)\delta(\tau - \tau^*)|\mu|\Theta(\mu)\mathrm{d}\Omega\mathrm{d}\tau \tag{5.4}$$

With $\Psi(\tau,\Omega) = I^\dagger(\tau,-\Omega)$ being the pseudo forward radiance field from equation 3.15 the derivative is finally given by:

$$\frac{\partial I(0,\Omega)}{\partial I_{Fl}} = \int_{4\pi}\Psi(\tau^*,-\Omega)\mu\Theta(\mu)\mathrm{d}\Omega \tag{5.5}$$

This is the downward directed flux of Ψ at the Earth's surface. With these calculations RemoTeC is able to retrieve the chlorophyll fluorescence emitted at the Earth's surface. These modifications are reported by Schepers et al. (2014) together with other updates of LINTRAN.

5.3. Retrieval concepts

Having updated the radiative transfer model of RemoTeC, the retrieval of fluorescence is processed in multiple steps. Two retrieval concepts are implemented in the scope of this study. One setup is a full physics approach updating the Baserun. This setup's radiative transfer model accounts for the surface radiance source. The other setup is a simple approach to retrieve chlorophyll fluorescence only. This setup uses Fraunhofer lines and neglects aerosol scattering events. For both retrievals a preprocessing step is necessary to correct for the detector specific radiance offset. This correction procedure depends on the used spectral range and is therefore different for the two retrieval setups.

Why using a retrieval setup that omits the O_2 absorption lines? In principle, a retrieval has less noise and more information on chlorophyll fluorescence if it uses the complete spectral measurement range. However, when using the complete O_2 A-band the radiative transfer needs to take atmospheric scattering events into account whereas a retrieval that only uses the Fraunhofer lines can neglect atmospheric particle scattering, see section 5.1. If the retrieval includes aerosol parameters, which account for Mie scattering, they are highly correlated with the retrieved fluorescence parameter. To motivate this, figure 5.3 shows the derivatives of the radiance with respect to five different parameters. These are the radiance offset, the fluorescence radiance (see section 6), and the three aerosol parameters that are introduced in chapter 3. Section 6.3 gives more details about the correlations in the complete O_2 A-band. Further advantages of a simple Fraunhofer line retrieval are a) due to relaxed clear sky filters much more data are retrieved, b) the retrieval is much faster which makes it easier to find an approach for the radiance offset correction, and c) the used fluorescence model that fits the GOSAT observations best can be adjusted in a shorter iteration cycle.

The current section focuses on the simple chlorophyll fluorescence retrieval based on Fraunhofer lines. This retrieval takes only Rayleigh scattering into account and neglects atmospheric aerosol or cirrus scattering. It uses relaxed clear sky filters and includes a multistage radiance offset correction, see section 5.4. The spectral range comprises two windows left and right of the O_2 A-band and is the same as used in Frankenberg et al. (2012) which is illustrated in figure 5.2. As the GOSAT instrument measures the O_2 A-band separately for P- and S-polarized radiance the retrieval consists of four independent retrievals. Section 3.3 gives an overview on the RemoTeC setup for the two used retrieval implementations in comparison.

5.4. The problem of radiance offset in GOSAT measurements

As described in chapter 2 both GOSAT detectors covering the O_2 A-band have a non-linear behavior. As the TANSO-FTS instrument is a Fourier Transform Spectrometer a signal non-linearity results in a broad band signal in the spectrum. Subsequently, in first approximation there are two broad band structures in the O_2 A-band a) a measurement artifact that is the radiance offset and b) the chlorophyll fluorescence signal. A retrieval of both parameters is bound to be correlated. The JAXA data processing tries to reduce the effect of the detector non-linearity. However, there is a remaining radiance offset that depends on wavelength, signal level, time, and gain setting. All these dependencies are different for both detectors and need to be corrected to obtain a fluorescence retrieval that is independent of these artifacts.

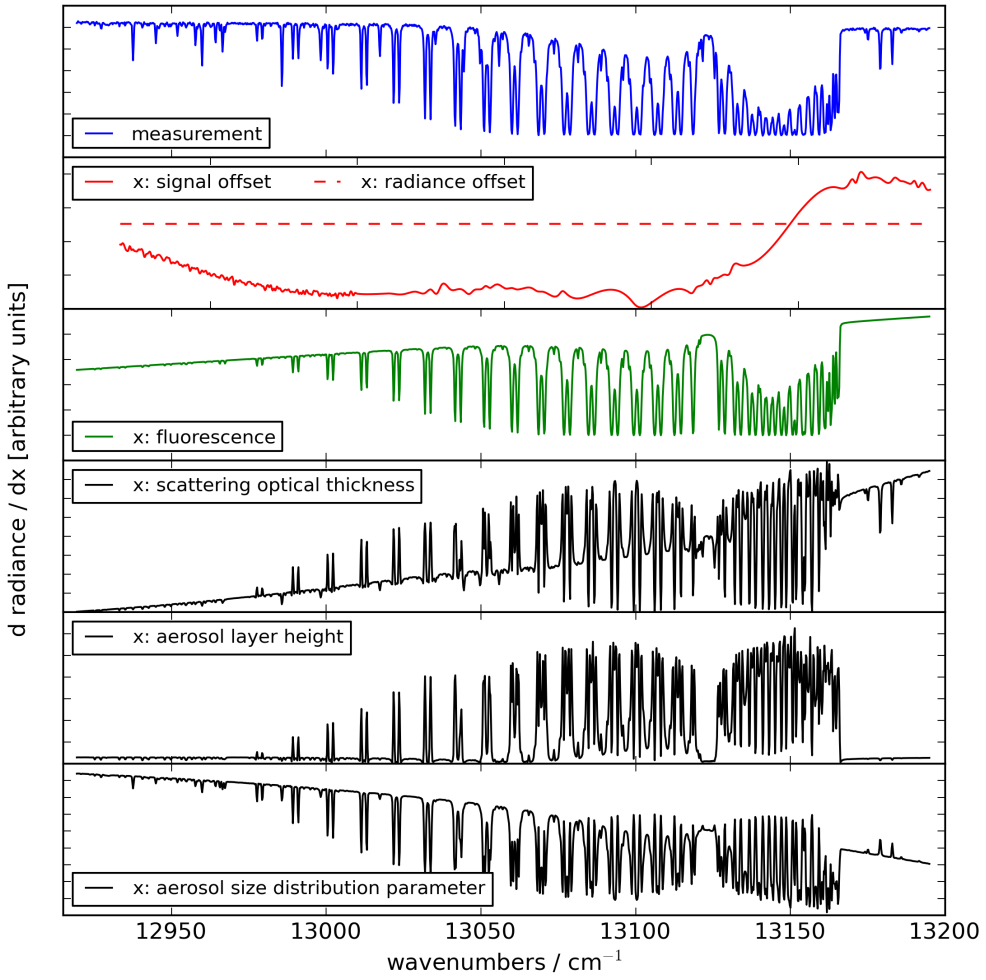

Figure 5.3.: Five derivatives of the measured radiance (top panel) in the O_2 A-band. The derivative with respect to the radiance offset retrieved as Volt signal offset (red solid line) depends on the spectroscopic calibration, whereas the derivative with respect to the radiance offset retrieved in radiance unit (dashed red line) does not depend on the radiance, see section 5.4 for details about the radiance offset. The derivative with respect to the fluorescence radiance (green) has two dependences a) the oxygen absorption lines as it transmits the atmosphere once and b) the fluorescence emittance model (underlying slope). The three subsequent panels show the derivatives with respect to the aerosol parameters. Note that they depend on the oxygen absorption lines and that they depend on the Fraunhofer lines as well. The derivatives for wavenumbers higher than 13170 cm^{-1} show clearly that this is different for the fluorescence Jacobian.

5.4.1. Correcting dependence of radiance offset on mean spectral signal

In the former RemoTeC version 2.0 the radiance offset was retrieved as an offset on the calibrated spectra in radiance units (Guerlet et al., 2013b). It compensated for broad band effects like the detector non-linearity and chlorophyll fluorescence. However, the non-linearity of the detector or the detector electronics affects the measurement in the uncalibrated state. To correct for these measurement artifacts properly, the radiance off-

set is now retrieved on the uncalibrated spectra in Volt units. See figures 5.3 and 6.1 for derivatives of the radiance with respect to the radiance offset and a world map of retrieved radiance offset, respectively. Chapter 2 discussed the origin and concepts of the radiance offset, chapter 4 discussed the retrieval quality in comparison to RemoTeC version 2.0.

The radiance offset fit accounts for the detector non-linearity. However, it also compensates the chlorophyll fluorescence signal to some extend. To avoid the loss of chlorophyll fluorescence information, the radiance offset is not fitted in the chlorophyll fluorescence retrieval setup. Instead, the radiance offset is empirically corrected with preprocessed information. This ensures that the chlorophyll fluorescence parameter does not comprise any correlation with a radiance offset fit parameter or the non-linearity.

To find a correction for the radiance offset, a data set is needed that contains no chlorophyll fluorescence signal. Furthermore, it needs to cover the complete time and all variability in the signal strength. The data set chosen here contains all spectra measured over Antarctica and all ocean glint spectra. All these spectra are measured in the high gain setting. Spectra for the medium gain setting are mostly taken over deserts. As the amount of medium gain data that can be used to do all necessary correction steps is too low, such spectra are not considered in this work.

Having identified the data set, the next step is to determine the radiance offset dependence on the mean signal. The correction procedure subtracts the found radiance offset from each individual spectrum corresponding to its mean signal. This is done individually for both polarizations and for both retrieval windows. The upper panel of figure 5.4 shows the dependence of the radiance offset on the mean signal for this data set. The lower panel shows the result of this correction step. The figure shows only the correction of one window and one polarization direction, the Appendix A lists the other cases.

In a preprocessing step a lookup table is generated which is used for interpolation later in the correction procedure. It lists the mean radiance offset per mean signal interval. The mean signal interval is chosen to be $\frac{1}{50}$th of the covered mean signal range. In figure 5.4 showing the radiance offset of the S-polarized 755 nm window this mean signal interval is approximately 10^{-8} W m^{-2} sr^{-1} µm^{-1}. The mean signal is calculated separately for each polarization within the two used retrieval windows.

The correction procedure is based on the Antarctica and ocean data only but it is applied to all land data. Thus, it has to rely on statistics being significant. RemoTeC filters out each spectrum that has a mean signal that is out of the mean signal range where a significant number of spectra from the correction data set is available. The minimum number of spectra to calculate a mean signal value is 150 spectra for the S-polarized radiance and 50 for the P-polarized radiance.

In the main processing, that is the retrieval itself, the mean signal is again calculated separately for each polarization within both retrieval windows. Then the correction routine linearly interpolates twice a) for the center of both correction windows the radiance offset according to their mean signal value from the lookup table, and as the radiance offset is wavelength dependent b) for each wavelength in the retrieval window using the centers of both windows as interpolation points. This calculated radiance offset is then subtracted from the spectrum before the following retrieval process. To evaluate the success of this correction procedure, it is applied to the Antarctica and ocean data again. As can be seen in the lower panel of figure 5.4 it works properly. The same is valid for the other retrieval window and the polarization cases, see Appendix A.

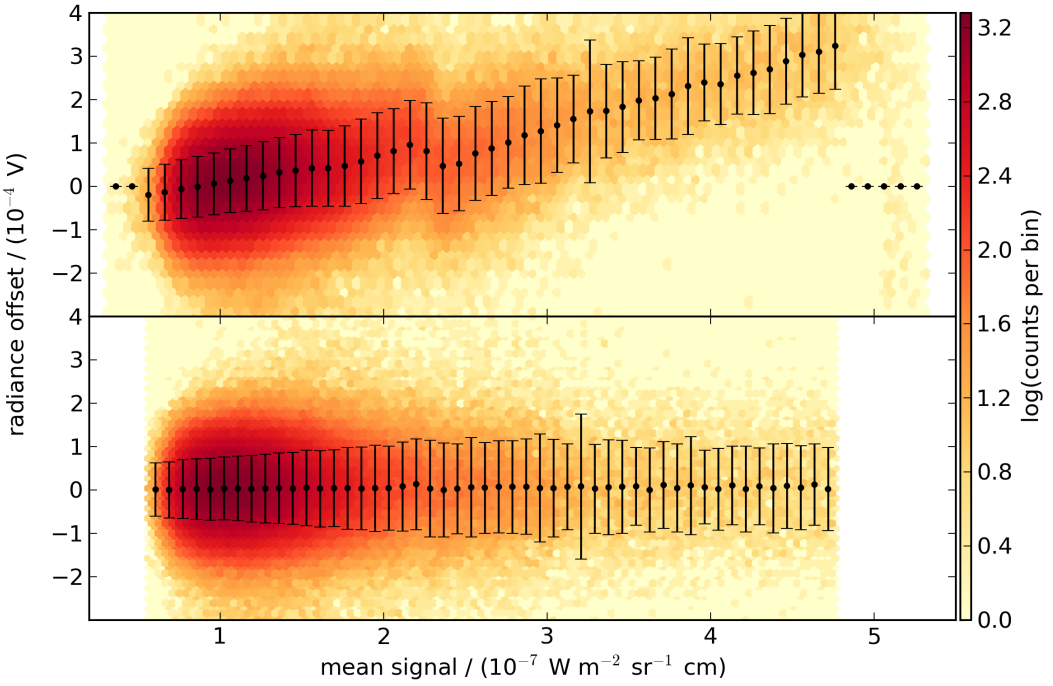

Figure 5.4.: Radiance offset dependence on mean signal before correction (upper panel) and after correction (lower panel). The spectra used in this retrieval are all GOSAT spectra taken over Antarctica and oceans. Thus, they are considered to be free of chlorophyll fluorescence signals. The radiance offset is retrieved in the 755 nm window for the GOSAT detector measuring S-polarized radiance. The two dimensional histogram is over plotted by the mean radiance offset within a small mean signal range and its standard deviation. The small mean signal range is $\frac{1}{50}$th of the complete mean signal range. Due to statistical relevance the mean value is set to zero in case less than 150 spectra are averaged. Spectra having a mean signal outside of the statistical relevant correction range are filtered out in the correction procedure.

5.4.2. Time dependence of the radiance offset

Having applied this correction on the radiance offset, the complete high gain land data set was processed and plotted as time series, see figure 5.5 for details about the S-polarized record from retrieval window 755 nm and figure 5.6 for a comparison among all four records. The time series contains the global geophysical variation of chlorophyll fluorescence. The clearly visible yearly cycle is reasonable due to the global inhomogeneous land distribution. The northern hemisphere has a larger land area and thus a more pronounced seasonal cycle of carbon fixation through photosynthesis and carbon release through respiration.

Besides that seasonal cycle, another temporal dependence is visible which is an exponential decay over the years. There is no reason or evidence that any global exponential decay is a real signal in the global chlorophyll fluorescence signal. Thus, this temporal behavior is solely driven by a remaining time dependence in the radiance offset. Most likely, this is caused by a degradation of GOSAT's detectors or the corresponding electronics.

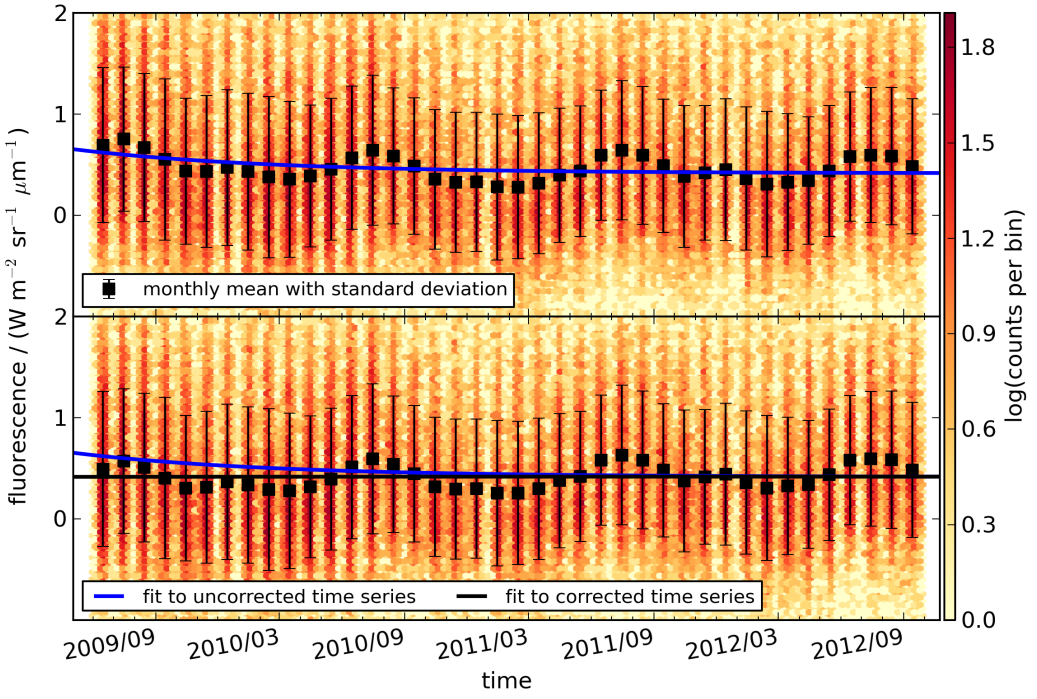

Figure 5.5.: The time dependence of the global fluorescence record before correction (upper panel) and after correction (lower panel). An exponential function $f(t) = ae^{b(t-t_0)} + c$ is fitted to the data. The blue line is fitted to the uncorrected data and is replotted in the lower panel to visualize the impact of the time dependence correction on the data. The black line fitted to the corrected data shows the time independence of the finally corrected fluorescence record. As in figure 5.4 the record shown here is retrieved in the 755 nm window measured in S-polarized radiance. See figure 5.6 for a comparison with the other three records.

A first correction approach was to split the correction described above into several correction steps for several time intervals. To capture the time dependence properly, the time intervals would need to be on the order of monthly or at maximum seasonal scale. However, such correction steps suffer from little data amount and thus lack robust statistics.

To correct the global fluorescence time series, the next attempt was to adjust the spectral calibration with a factor decaying exponentially with time. This adaption of the spectral calibration revealed that it is not the same time dependence for the two detectors and also the two retrieval windows have a different temporal behavior. Furthermore, the time dependence was found to be an offset and not a scaling on the radiance offset.

Finally, the radiance offset correction procedure described in the previous subsection is modified with a time dependent offset $f(t) = ae^{b(t-t_0)} + c$. The exponential function $f(t)$ contains the two free parameters a and b that are individually determined for each retrieval window and polarization. The parameter c is chosen such that $f(t_{max}) = 0$ at the end of the time period. Thus, the radiance offset correction is modified strongest in the beginning of the time record. In the end of the time series the radiance offset correction is driven by the mean signal and the considered wavelength range only. Table 5.1 lists the parameters a and b. See the result of this correction in the lower panel of figure 5.5 and figure 5.6.

Polarization	Window [µm]	a/ (10^{-5} V)	b/ (10^{-3} /d)
S	755	2.27	-3.45
S	772	4.79	-3.19
P	755	3.04	-5.15
P	772	2.96	-3.84

Table 5.1.: Parameters for the time dependent offset of the radiance offset. The exponential time dependent offset is given by $f(t) = ae^{b(t-t_0)} + c$ where c is determined by $f(t) = 0$ in 2012 September 15 and t_0 is the 14th December 2008.

Kuze et al. (2012) reported about the signal non-linearity causing the radiance offset in the level zero to level one processing. They found the radiance offset to depend on mean signal level, time, and temperature. In the level two data shown here, the dependence on mean signal and time are both significant. The stronger time dependence of the P-polarized measurements reported by Kuze et al. (2012) is clearly visible in figure 5.6. The reported dependence on temperature, which could lead to a seasonal or orbit phase dependence in the fluorescence record, is not detected by the RemoTeC retrievals.

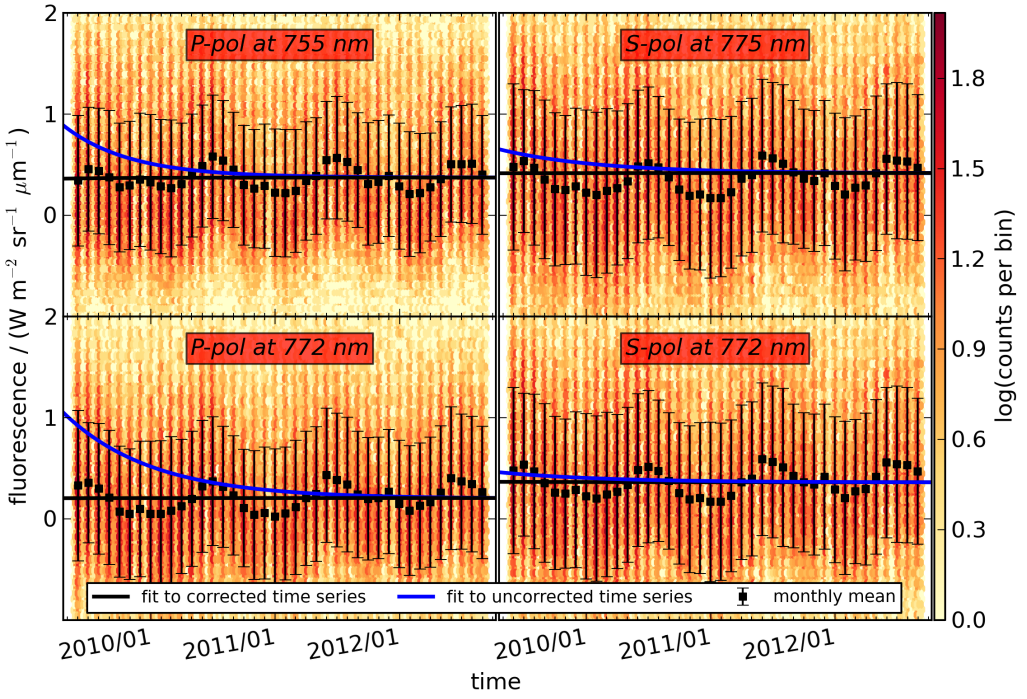

Figure 5.6.: Time series of all four, finally corrected, global chlorophyll fluorescence retrievals in comparison, using the same illustration as figure 5.5 lower panel. These four independent retrievals show a good consistency among each other, only the retrieval of the P-polarized retrieval window around 772 nm has low biased values compared to the other three. The strong time dependence of the P-polarized data set is expected according to Kuze et al. (2012).

5.5. The retrieved chlorophyll fluorescence record

Subsection 5.5.1 discusses the used top of the canopy chlorophyll fluorescence model. Subsection 5.5.2 considers the noise of the retrieved chlorophyll fluorescence record. Finally, subsection 5.5.3 illustrates the spatial and temporal patterns found in the chlorophyll fluorescence record and its correlation to GPP.

5.5.1. The spectral model of the top of canopy emitted chlorophyll fluorescence

As introduced earlier, the GOSAT chlorophyll fluorescence record is retrieved independently from four data sets. These are the measurements of the two detectors and the two considered wavelength ranges. Figure 5.6 shows the global time series of all four retrievals to be quite consistent among each other. This consistency depends strongly on the chosen fluorescence model. The chlorophyll fluorescence model describes the wavelength dependence of the fluorescence radiance.

Due to several processes that are necessary to evaluate the fluorescence model on its consistency between the four GOSAT data sets, only three models where tested here. For testing the three models, the amount of data was randomly reduced tenfold. Two of the models are shown in figure 5.1. One tested model is a double Gaussian model. Its parameterization is given in Frankenberg et al. (2012). This model is supposed to give a realistic top of the canopy fluorescence spectrum. In this double Gaussian model the fluorescence radiance at 755 nm wavelength is roughly 2.7 times higher than the radiance at 772 nm. For the chlorophyll fluorescence retrieval Frankenberg et al. (2012) used a linear fluorescence model. They reported the ratio $\frac{\text{radiance at 755 nm}}{\text{radiance at 772 nm}} = 1.7$ to achieve the best consistency among the two wavelength ranges. This simple linear fluorescence model is also tested here and is shown in figure 5.1. Finally, a modified double Gaussian model was tested that was broadened such that the ratio $\frac{\text{radiance at 755 nm}}{\text{radiance at 772 nm}}$ is 1.7.

The double Gaussian model taken from Frankenberg et al. (2012) supposed to give a realistic top of the canopy fluorescence spectrum yields a strong negative bias in the fluorescence record retrieved in the window around 772 nm with respect to the record retrieved in window around 755 nm. The modified double Gaussian model yields a somewhat better consistency between the two wavelength regimes but introduced some inconsistency between the two polarizations. The best agreement among the four retrievals was achieved by the simple linear fluorescence model. The four resulting chlorophyll fluorescence records are shown in figure 5.6. This simple linear fluorescence model is therefore used also in the full physics based retrieval concept, see chapter 6.

5.5.2. Noise in the chlorophyll fluorescence record

As already motivated in figure 2.2 in section 2.3 the noise in the fluorescence record is quite high. For both used retrieval windows, the scatter in the data is found to be roughly the same.

The expected detector noise error for each of the four independent data sets is on average 0.81 W m^{-2} sr^{-1} μm^{-1}. The final chlorophyll fluorescence data set averaging all four independent records has on average the noise error 0.41 W m^{-2} sr^{-1} μm^{-1}. Compared to typical summer chlorophyll fluorescence radiance in the tropics or central Europe this is around 30% or 70%, respectively.

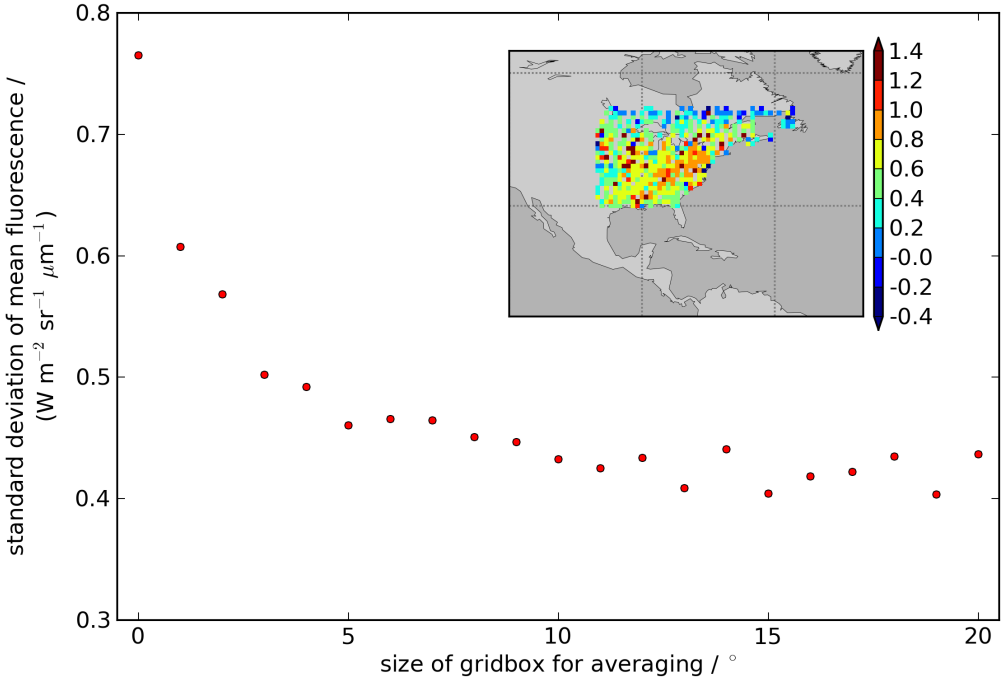

Figure 5.7.: Spatial averaging reduces the standard deviation in the fluorescence signal. The map inset shows the fluorescence radiance measurements in $Wm^{-1}sr^{-1}\mu m^{-1}$ over the analyzed north American region using averages within 1° by 1° grid boxes. The standard deviation of the mean fluorescence in the complete area is calculated for grid box sizes between 1° and 20°. The value at 0° grid box size is the standard deviation of all individual measurements without any averaging.

Due to its high noise, the chlorophyll fluorescence retrieval needs to be averaged. The temporal average interval is chosen to be monthly to capture the temporal variability. To choose a proper spatial scale for averaging the fluorescence signal, the reduction in the standard deviation of the fluorescence in a region was plotted in dependence on the averaging grid box size, see figure 5.7. The standard deviation of the fluorescence signal in the shown north American region within the 40 month time interval was calculated without averaging and for different grid box sizes between 1° and 20° both latitude and longitude. The standard deviation clearly decays strongly up to a grid box size of 5° by 5°. A similar result was found for the tropical American region. The spatial averaging in this work is chosen to be 4° by 4° to enable a direct comparison with other reported fluorescence records.

In Chapter 6 it is discussed that the expected noise is lower for a retrieval that uses the complete O_2 A-band. However, the errors in such a retrieval are dominated by systematic effects.

5.5.3. The spatiotemporal patterns of chlorophyll fluorescence and its correlation to GPP

The upper panel of figure 5.8 shows a world map of the chlorophyll fluorescence record retrieved in the 40 month period from June 2009 till September 2012. Strongly pronounced chlorophyll fluorescence signals are retrieved in the highly vegetated tropics. The mountain areas in north and south America as well as the Himalayan region reveal no detectable fluorescence signal. Further, the ice covered surfaces in Antarctica and Greenland yield zero fluorescence within the discussed uncertainty. Note that this is a yard stick for the radiance offset correction as an uncorrected record would retrieve substantial fluorescence signals over ice surfaces which typically exhibits a high signal level in the O_2 A-band.

The lower panel of figure 5.8 shows the temporal evolution of the chlorophyll fluorescence signal for zonal means. Within a latitudinal interval of 4° all fluorescence spectra are averaged within one month and plotted for the 40 months time series. The maximum chlorophyll fluorescence signal in the tropics oscillates around the equator with the solar zenith. In the northern hemisphere between 30° and 70° the chlorophyll fluorescence signal peaks in June and July. Due to the plane parallel assumption in the radiative transfer model, spectra which are measured with solar zenith angles higher than 70° are filtered out, see Chapter 3. As a result, in northern and southern hemisphere winter no measurements are available in latitudes higher than roughly 50° north and south, respectively.

The retrieved chlorophyll fluorescence record is directly correlated to GPP model data from the Jena Max Planck Institute (Jung et al., 2011). Figure 5.9 shows the fluorescence record versus the GPP model data. The chlorophyll fluorescence data are sampled spectrum per spectrum with the GPP data. As the GPP data are available only until end 2011 the spectra from 2012 are simply treated as if they where measured in 2011.

This chapter discussed the direct link between the chlorophyll fluorescence radiance and the plant's photosynthetic activity. Due to this link, remote sensing of chlorophyll fluorescence radiance provides insight into the major natural sink of the carbon cycle that is photosynthetic gross primary production (GPP). On the other hand, if the chlorophyll fluorescence radiance is neglected in the radiative transfer, it is an error source for remote sensing atmospheric CO_2 and CH_4 abundances. Previous studies already retrieved chlorophyll fluorescence and correlated it to GPP. However, none of these studies included a physics based radiative transport model of the chlorophyll fluorescence. Here, this chapter presents the necessary modifications of RemoTeC's radiative transfer model (RTM) which enable the RTM to calculate the light path of the surface emitted chlorophyll fluorescence radiance in a multiple scattering atmosphere. Further, an empirical radiance offset correction procedure for high gain GOSAT spectra is discussed. Finally, this chapter showed that the physics based retrieved chlorophyll fluorescence record is highly correlated with GPP and is well in line with other published data, for instance by Frankenberg et al. (2011b). The results presented in this chapter therefore support and validate the published ones.

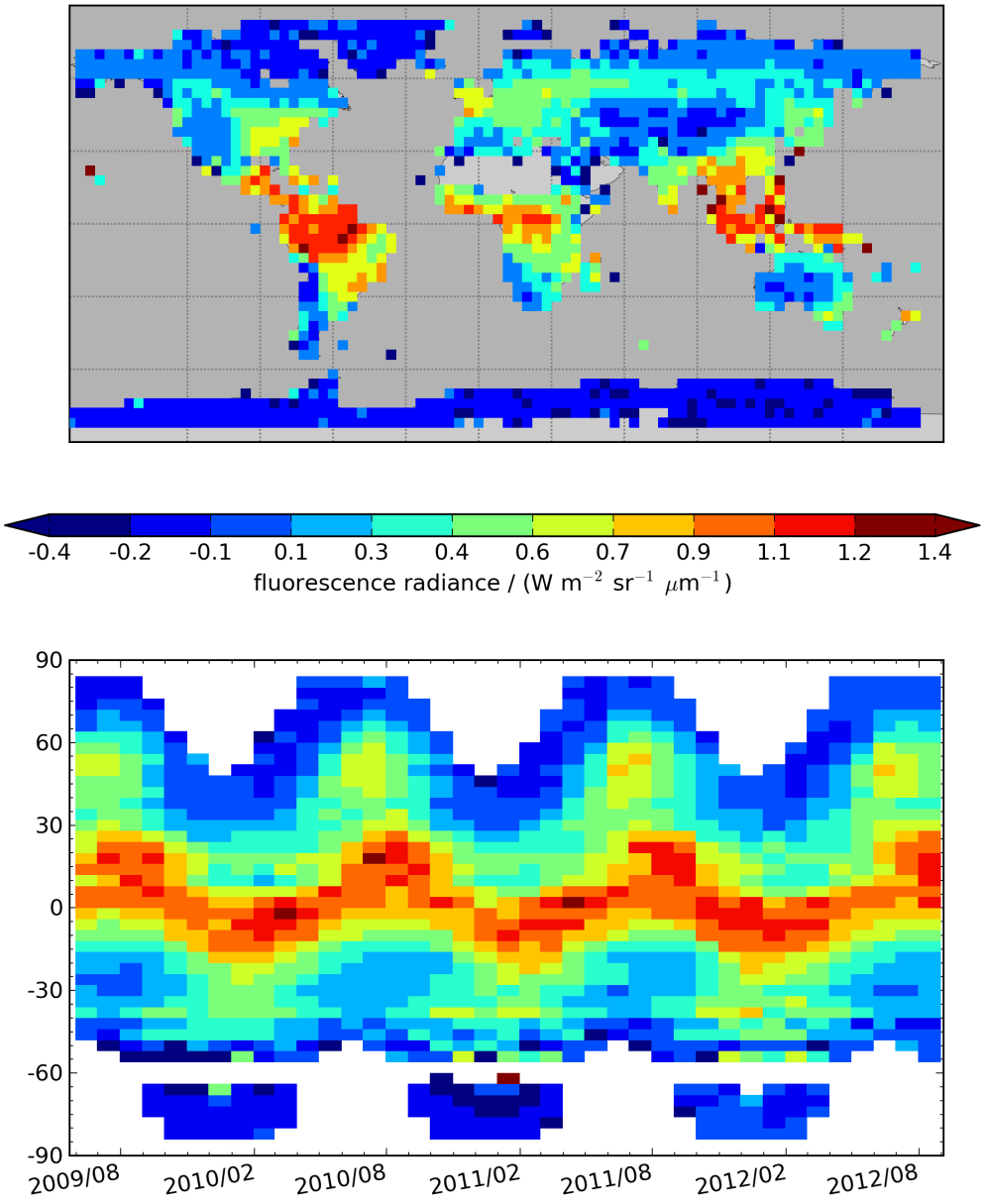

Figure 5.8.: The chlorophyll fluorescence record. The **upper panel** shows a world map where all measurements of the 40 months data set are averaged within each 4° by 4° grid box. The pattern shows a strong chlorophyll fluorescence signal in the highly vegetated tropical areas as well as two pronounced regions in the northern hemisphere in eastern America and western Europe. Note that the spectra measured over ice covered surfaces are around zero which is not the case for a fluorescence retrieval not accounting for radiance offset effects due to high mean signal levels. The **lower panel** shows a zonal mean time series. Shown are the zonal means within 4° latitudes per month. The high photosynthetic activity around the equator oscillates with the zenith of the sun. In the northern hemisphere a clear seasonal cycle of almost no detectable activity in winter and chlorophyll fluorescence signals in summer reaching up to 0.7 $Wm^{-1}sr^{-1}\mu m^{-1}$ is visible.

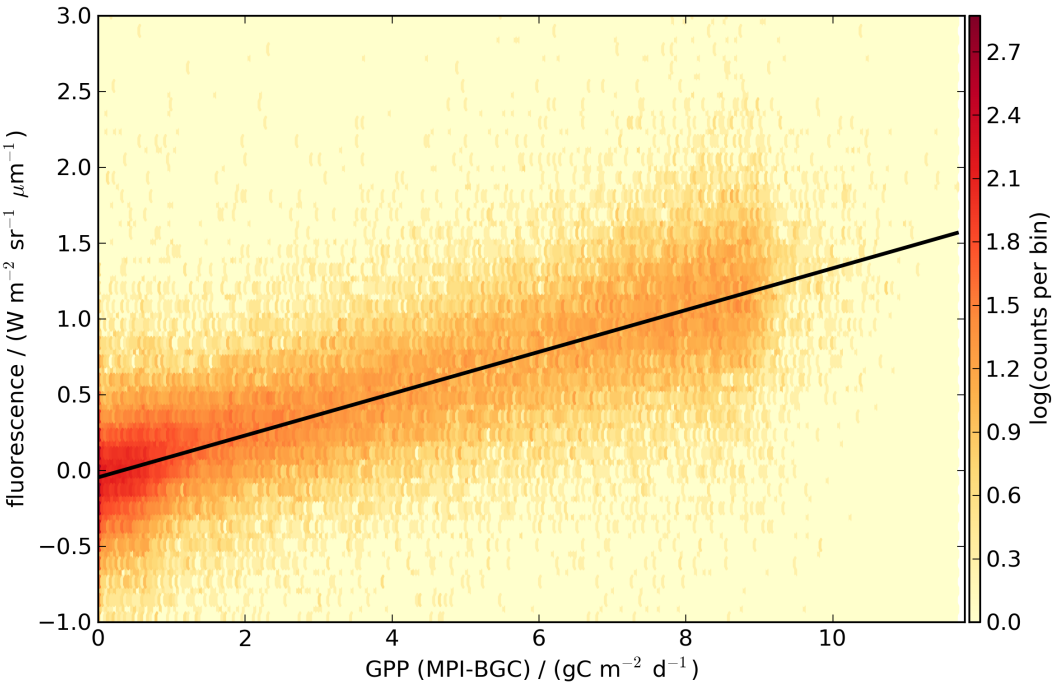

Figure 5.9.: The fluorescence record is correlated with the gross primary production (GPP) data from MPI-BGC model. Shown is a histogram of all fluorescence data sampled with GPP model data over plotted by a linear regression line (black). The GPP model data for 2012 are repeated from 2011 as the data set is only available until end 2011.

6. Chlorophyll fluorescence in the full physics retrieval

For XCO_2 and XCH_4 retrievals using the O_2 A-band it is an error source to neglect chlorophyll fluorescence (Sioris et al., 2003; Frankenberg et al., 2012). Frankenberg et al. (2012) reports, based on a simulation study, an error in XCO_2 of up to 1.0 ppm if a radiance offset is fitted but chlorophyll fluorescence of 1.5% of the contiduum level is neglected in the retrieval. For assessments of the carbon cycle, this is delecate as most fluorescence occurs at geolocations where strong XCO_2 sinks are located, for instance, in the Amazonian tropical forest.

The previous chapter showed how to account chlorophyll fluorescence in the radiative transport model of RemoTeC and presented the Fraunhofer retrieval concept that retrieves chlorophyll fluorescence by accounting for the radiative transport and correcting for detector non-linearity. This chapter discusses the impact of accounting for chlorophyll fluorescence in the full physics RemoTeC retrieval setup. Section 6.1 resumes the radiance offset issue. A residuum fit is introduced in section 6.2. Section 6.3 discusses remaining issues of the chlorophyll fluorescence record retrieved by the new full physics retrieval called Fluorun. A comparison to the chlorophyll fluorescence retrieved with the Fraunhofer concept is given in section 6.4. The impact on the XCO_2 and XCH_4 retrieval and the performance compared to TCCON is examined by section 6.5. Finally, section 6.6 analyzes the influence of the apriori XCO_2 and XCH_4 profiles on the TCCON validation.

6.1. Radiance offset in the full physics retrieval

The radiance offset is an intensity dependent feature in the GOSAT spectra caused by non-linearity of the detectors and the electronics. Details are given in section 2.3 and 5.4. The derivatives of the radiance offset parameter and the chlorophyll fluorescence parameter with respect to the radiance were shown in figure 5.3. Although these two derivatives exhibit quite a different spectral behavior, they are both correlated to some extend. This can be seen empirically in the radiance offset world map in figure 6.1 which is retrieved with the full physics approach. Comparing the spatial pattern of the radiance offset to the spatial pattern of the chlorophyll fluorescence retrieved with the Fraunhofer retrieval concept in figure 5.8, it is obvious that the radiance offset fit compensates at least a part of the chlorophyll fluorescence signal.

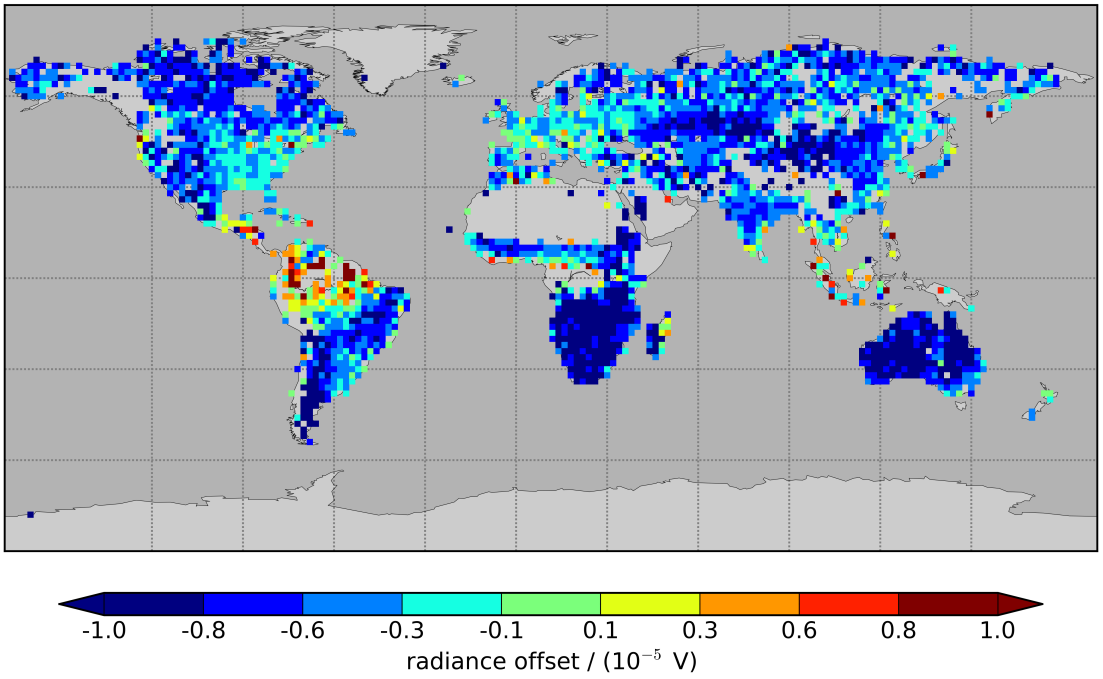

Figure 6.1.: Radiance offset world map retrieved by the full physics Baserun. Shown are averages of 40 months per 2° by 2° grid box high gain land soundings. The pattern reveals that the radiance offset parameter clearly compensates chlorophyll fluorescence to some extend.

Now, the two small wavelength regimes from the Fraunhofer retrieval concept are extended to the complete O_2 A-band. The presented correction strategy, from section 5.4 might not be applicable to the full physics retrieval because the radiance offset depends on wavelength and the full physics retrieval uses a wider wavelength range. Accordingly, the correction procedure first needs to be tested for the full physics retrieval, using the complete O_2 A-band. Unfortunately, it introduces strong dependencies of the retrieved XCO_2 with several geophysical parameters. In short, the considered wavelength range requires its own dedicated radiance offset correction procedure.

Subsequently, again a data set of spectra which contain no fluorescence signal is needed. For the Fraunhofer retrieval concept the Antarctica and ocean data set was suitable. For the full physics retrieval such a data set would not work, as the retrieval of the fluorescence parameter is strongly correlated with aerosols. Thus, the correction data set must be free of chlorophyll fluorescence and, additionally, it must be free of aerosols.

Butz et al. (2013) presented a tool to find a set of aerosol free ocean glint data. This relies on the fact, that the ground albedo determines the ratio of lightpath shortening to lightpath enhancement due to aerosols. Butz et al. (2013) found that, due to low albedo over ocean surfaces for any direction except for the glint geometry, the lightpath shortening is dominant over the ocean. This is used to extract a clear sky data set which is called upper edge data set and contains roughly 14,000 spectra.

The upper two panels of figure 6.2 show the retrieved radiance offset versus the mean signal for the upper edge ensemble without correction and with the applied Fraunhofer concept

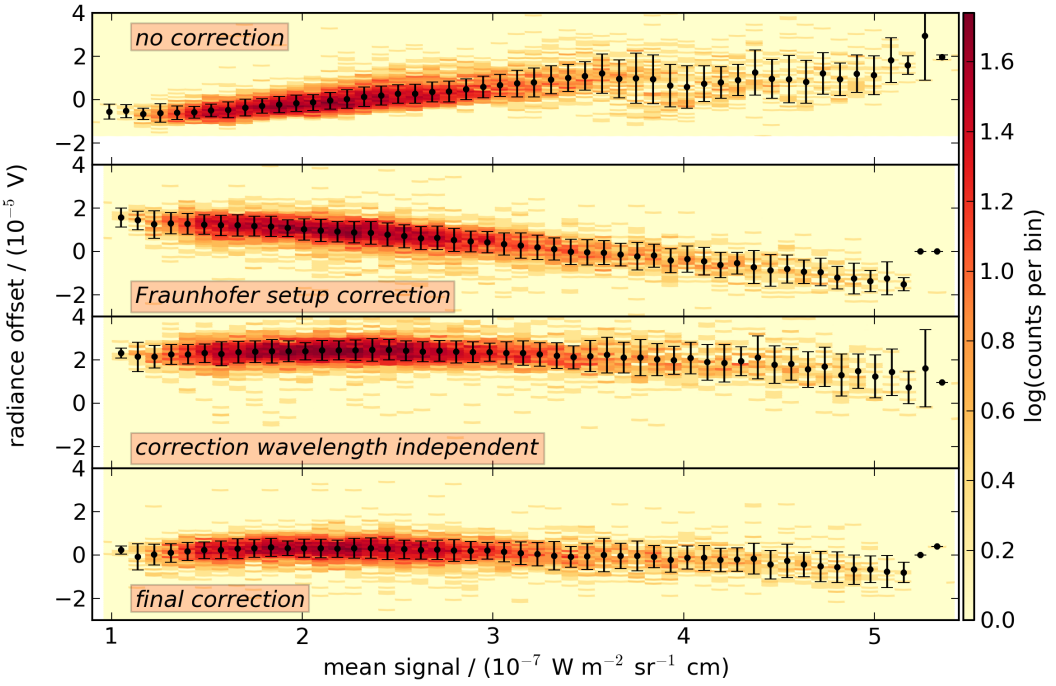

Figure 6.2.: Illustration of the adjustments of the radiance offset correction procedure for the full physics setup using the complete O_2 A-band. As in figure 5.4 the data set is plotted in a two dimensional histogram overplotted by averages of small mean signal ranges. The figure shows different retrievals of the upper edge ensemble which is in good approximation free of chlorophyll fluorescence and free of aerosols. The top panel shows the data set without any correction. The second panel from top shows the effect of the correction that was used in the Fraunhofer setup. It smoothes the dependency of the radiance offset on the mean signal level. However, a clear trend is remaining. This trend is reduced by changing the correction to a wavelength independent correction as can be seen in the third panel from top. However, a bias of roughly $2 \cdot 10^{-5}$V remains. The final correction procedure additionally subtracts this bias which results in a full physics retrieval record that is sufficiently independent on mean signal level shown in the bottom panel.

correction, respectively. Indeed, the Fraunhofer concept correction smoothes the graph from the upper panel. However, a significant negative slope is induced by this correction.

The two small windows, used in the Fraunhofer retrieval, feature different mean signal levels. Accordingly, the correction procedure included a linear interpolation between the tabulated mean signal levels at 772 and 755 nm wavelength. Thus, this correction step alters the uncalibrated spectrum with a wavelength dependent offset. Contradictory, the full physics radiance offset retrieval parameter is a simple offset without any wavelength dependence. These mismatching implementations of the wavelength dependency are the major reasons for the poor performance of the correction procedure derived from the Fraunhofer retrieval concept being applied one by one to the full physics retrieval.

The tabulated mean signal levels for both polarizations and both Fraunhofer retrieval windows, embracing the O_2 A-band, are based on broad statistics because they are calculated from all ocean glint and all Antarctica data. Accordingly, the tabulated values are assumed

to constrain the mean signal level of the O_2 A-band correctly. To match the wavelength independent implementation of the full physics radiance offset parameter, the correction procedure is adjusted. The linear slope, which is subtracted from the uncalibrated spectra, is substituted by a constant. The constant is simply the mean signal value interpolated from the lookup table to the middle of the O_2 A-band. The effect is seen in the third panel from top in figure 6.2. It clearly remedies the dependency of the retrieved radiance offset with the mean signal. However, a small offset of roughly 0.02 mV remains. This is subtracted in an additional, final, correction step. The result is shown in the lowest panel in figure 6.2.

The described correction procedure accounts for the detector non-linearity by a calibration of each spectrum based on the spectrum's mean signal level. Thus, the new correction procedure addresses the radiance offset signal at its origin which is the detector non-linearity. In contrast, the former RemoTeC setup used to retrieve a radiance offset which is in first approximation the result of the detector non-linearity. However, the new correction procedure relies on robust statistics and is only established for GOSAT's high gain spectra.

6.2. The chlorophyll fluorescence parameter interferes with spectroscopic residua or instrument artifacts

Applying the full physics radiance offset correction, the chlorophyll fluorescence retrieval yields the spatial pattern demonstrated in figure 6.3. Generally, there are some patterns similar to what is expected from the Fraunhofer chlorophyll fluorescence retrieval, for instance, in the northern USA. Otherwise, there are regions where the pattern is completely unexpected, for instance, in India and south west Asia. Moreover, the absolute values of the fluorescence retrieval parameter are off the expected range. The complete range is negative and seems to be biased by 1.2 W m^{-2} sr^{-1} μm^{-1}. This is a clear indication that the fluorescence retrieval parameter compensates information in the residuum which is not a signal from chlorophyll fluorescence.

The residuum of the O_2 A-band averaged over all spectra from the upper edge ensemble reveals significant structures, see figure 6.4. Most likely, they originate from erroneous spectroscopy. The average upper edge residuum can be fitted in the retrieval process, without fitting information needed for the aerosol or fluorescence fit, because this averaged residuum is free of aerosols and fluorescence. If some residual structures remain after fitting the first averaged residuum, this residuum fit process can be repeated with higher order residua. As the Earth orbits the Sun and the satellite orbits the Earth, the resulting Doppler shifts comprises seasonal dependencies. Such seasonal variations are not captured by a single order residuum fit. See figure 6.4 for the residua of the first three orders.

This residuum fit must reduce the χ^2 of the retrieval. Indeed, this is demonstrated in figure 6.5. The upper panel shows the χ^2 calculated in the O_2 A-band retrieval window for the upper edge ensemble without applying the residuum fit. The lower panel presents the substantially reduced χ^2 for the same ensemble, but the retrieval included the residuum fit. No seasonal variation is detectable in the lower panel proving the three order residuum fit to capture all seasonal variations.

The full physics retrieval, including the residuum fit, yields the chlorophyll fluorescence record that is illustrated in the world map in figure 6.6. The significant effect of the residuum fit on the chlorophyll fluorescence parameter in the full physics retrieval manifests in the signal range. Correcting for a residual structure by the residuum fit results in

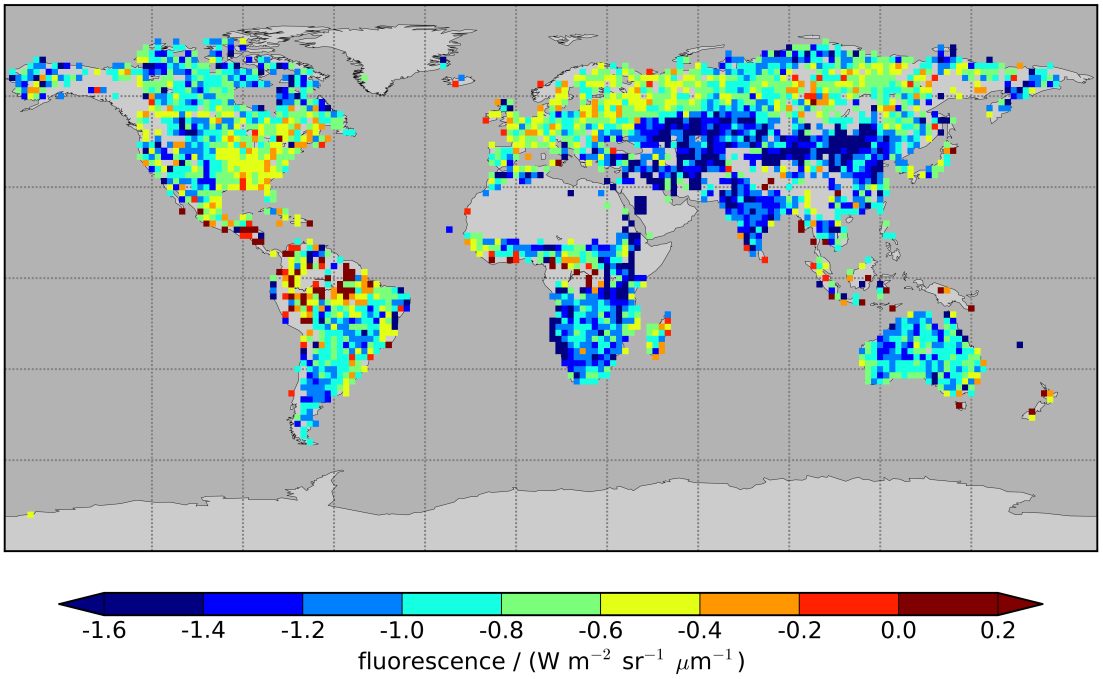

Figure 6.3.: The chlorophyll fluorescence record of the full physics retrieval where the radiance offset is not fitted but corrected. Shown are averages of 40 months per 2° by 2° grid box. Despite higher scatter and some differences the pattern is roughly in agreement with the fluorescence record derived with the Fraunhofer retrieval from figure 5.8. However, the signal range reveals that this fluorescence record does not reflect physical chlorophyll fluorescence radiance as these must on average exhibit positive values. Only due to noise error it can be negative.

realistic chlorophyll fluorescence signals over these parts of the world where high chlorophyll fluorescence signals are expected. The significant change in the retrieved fluorescence parameter caused by the residuum fit demonstrates the fluorescence parameter's high sensitivity to spectroscopic errors in the O_2 A-band.

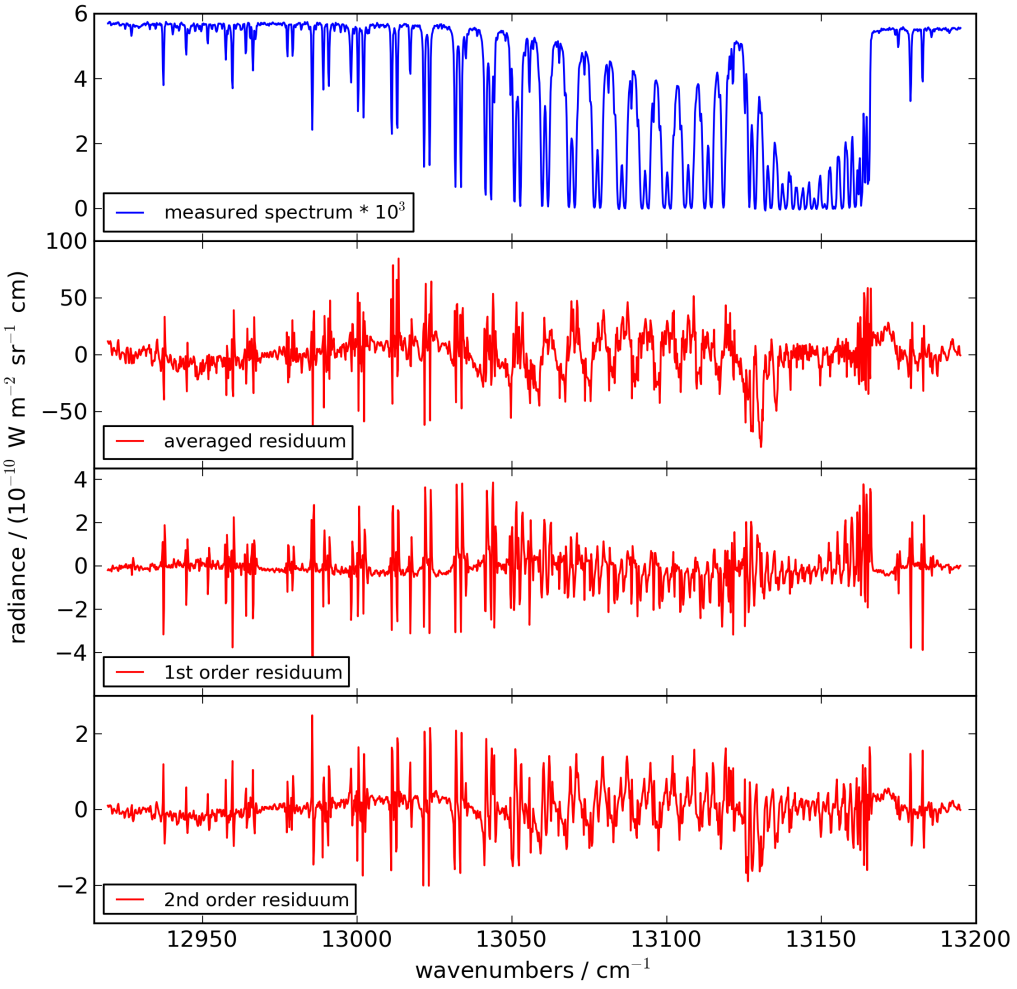

Figure 6.4.: Residua in the O_2 A-band. The top panel shows a single spectrum from the upper edge data set, see section 3.4. The panel underneath shows the averaged residuum of the complete upper edge data set retrieved with a full physics approach correcting the radiance offset and not fitting fluorescence. As this data set is considered to be free of aerosols and chlorophyll fluorescence, this 0th order residuum is only induced by errors in the spectroscopy or uncorrected instrument artifacts. The subsequent panel shows again an averaged residuum of this data set but this retrieval additionally fits the 0th order residuum. Thus, this is the 1st order residuum which is more than one order of magnitude smaller. This procedure is repeated once more resulting in the 2nd order residuum in the lowest panel which is smaller than the 1st order residuum by a factor of roughly 2. Higher order residuals might occur due to seasonal variation in the Doppler shift of the Earth-Sun or the Earth-satellite system.

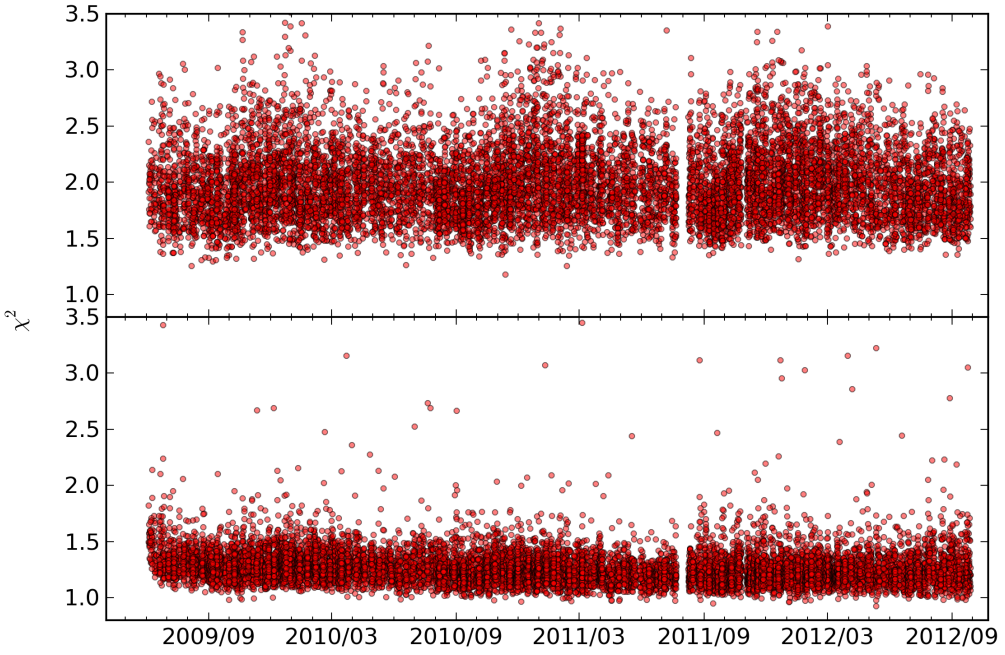

Figure 6.5.: χ^2 reduction through the residuum fit. Plotted is a time series of the χ^2 in the O_2 A-band. The upper panel shows the time series of the upper edge ensemble without fitting the mean residuum. The lower panel shows a substantially reduced χ^2 time series for the same ensemble where the retrieval approach includes the fit of all three mean residuals shown in figure 6.4. The lower χ^2

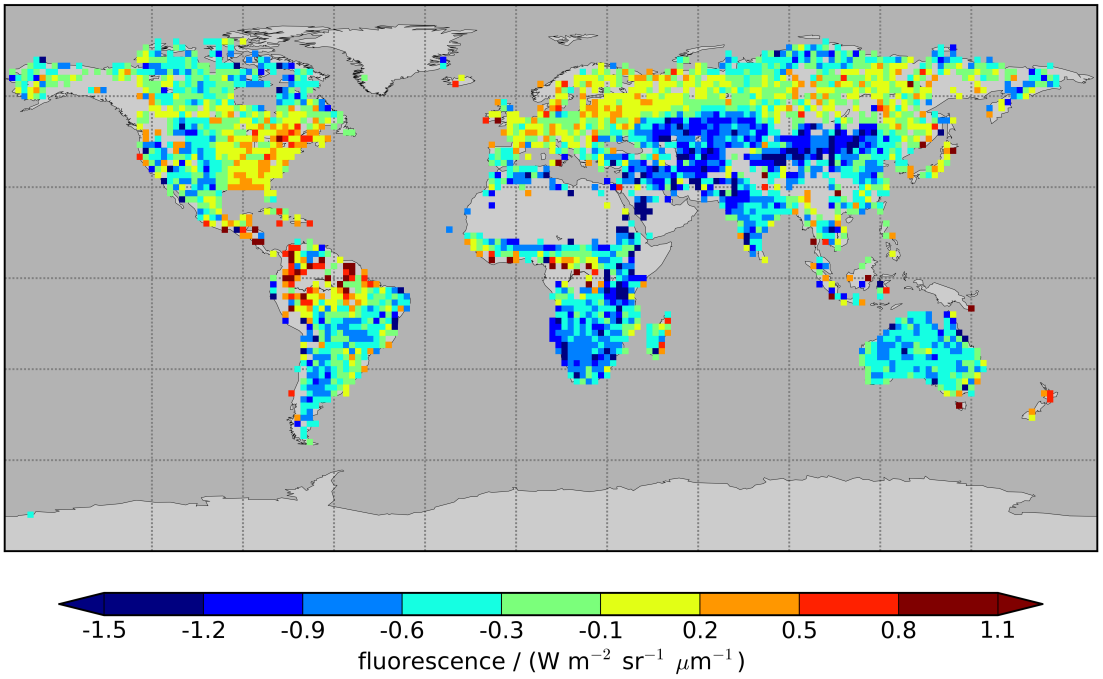

Figure 6.6.: Chlorophyll fluorescence world map retrieved with the full physics retrieval setup including the residuum fit. For regions where high fluorescence values are expected according to figure 5.8, the full physics approach largely retrieves realistic chlorophyll fluorescence values. However, if no fluorescence signal is evident, the full physics fluorescence parameter retrieves quite negative values.

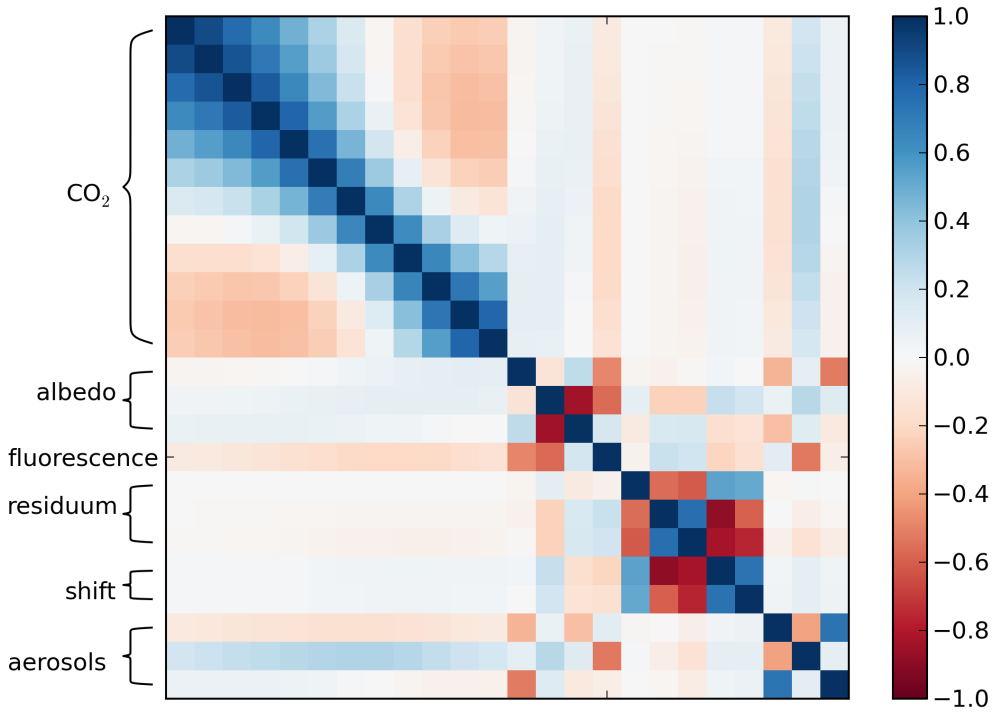

Figure 6.7.: Single spectrum correlation coefficients matrix of 24 state vector elements (columns and rows are equal). Shown are twelve CO_2 layers followed by the O_2 A-band parameters which comprises three albedo parameters, the fluorescence parameter, three residuum parameters, and two Doppler shift parameters to correct for the spectral and the solar shift. Finally, there are the three aerosol parameters representing the aerosol amount, layer height and size distribution. The fluorescence correlation coefficients show a clear anti-correlation with the aerosols height and the albedo.

6.3. Issues of the full physics chlorophyll fluorescence record

The full physics concept, which corrects the radiance offset and retrieves three orders of spectroscopic or instrument artifact residual structures, partially results in realistic chlorophyll fluorescence signals. However, the full physics chlorophyll fluorescence record exhibits quite negative values in parts of the world where no significant chlorophyll fluorescence signal is evident. This may be caused by correlation to other parameters. To motivate this empirically, figure 6.7 shows the correlation coefficient matrix for one spectrum with typical summer fluorescence intensity and a medium aerosol optical thickness of 0.1. See section 3.6 for the calculation of the correlation coefficients. The system of aerosol parameters, albedo, and fluorescence is clearly correlated. Hence, the fluorescence parameter can compensate for aerosol effects and vice versa.

To some extend, the negative values of the chlorophyll fluorescence are caused by an insufficient radiance offset correction. Figure 6.8 shows a time series of the full physics chlorophyll fluorescence retrieval of the upper edge ensemble and the complete high gain land data set in the upper and lower panel, respectively. The upper edge ensemble is assumed to be free of aerosols and chlorophyll fluorescence. Thus, it is used for the radiance offset correction, see figure 6.2. Accordingly, this data set should scatter around

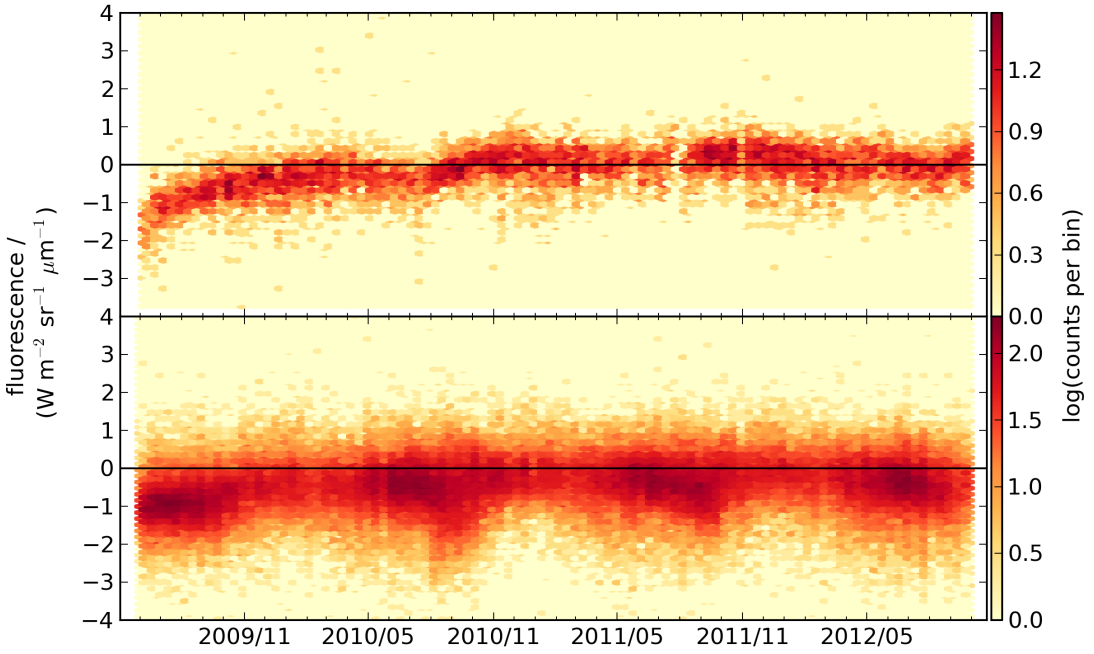

Figure 6.8.: Time series of the full physics fluorescence for the upper edge ensemble in the upper panel and the entire land data set in the lower panel. The time dependence of the full physics retrieval is different from the time dependence in the Fraunhofer retrieval caused by distinctive time dependence in the used spectral ranges. Up to September 2010 the upper edge ensemble fluorescence is on average below zero. As the time dependence of the S- and P-polarization detector is different a proper correction would require an analysis of retrievals with only one of the two radiance measurements. This is not part of this study which might cause a somewhat pessimistic full physics chlorophyll fluorescence record. Anyway, even when disregarding the first 15 months the chlorophyll fluorescence parameter on average is too negative.

zero. As can be seen in the upper panel of figure 6.8, this is not the case throughout the time series. The mean level of the chlorophyll fluorescence signal rather evolves with time. Especially, the first 15 month of the time period are erroneous. The temporal evolution of the radiance offset depends on the polarization and, additionally, it depends on the wavelength regime. This was shown in figure 5.6 for both polarizations and the two small Fraunhofer retrieval windows. The full physics retrieval uses both polarizations together and extended the wavelength range. Thus, a more sophisticated radiance offset correction scheme might improve the full physics chlorophyll fluorescence retrieval.

However, the land data set plotted in the lower panel of figure 6.8 reveals that the chlorophyll fluorescence parameter are on average too negative. This is evident even in the later time period where the temporal behavior of the radiance offset has no influence on the correction procedure. Thus, the correction procedure might affect the chlorophyll fluorescence record but can explain only little of the negative data range.

To avoid negative chlorophyll fluorescence values, which have no physical meaning, one idea was to restrict the retrieval to positive values. This was tried by adjusting the inversion scheme. First, fitting the logarithm of the fluorescence was tested as it is a mathematically

easy method to restrict the fluorescence to positive values. However, the fluorescence is close to zero which results in a highly non-linear retrieval. Unfortunately, this approach is unacceptable because most spectra fail to converge.

Furthermore, a truncation of the chlorophyll fluorescence retrieval parameter was tested. The retrieval truncated the fluorescence at zero in case the inversion would set it, according to the Jacobians, negative in the 6th or higher iteration. However, again most spectra fail to converge. Indeed, a retrieval setting one parameter other than the Jacobians suggest is inconsistent. In short, no alternative successful regularization was found.

6.4. The full physics chlorophyll fluorescence record in comparison to the Fraunhofer retrieval's fluorescence

To properly analyze the full physics fluorescence retrieval as well as the interdependent cycles of chlorophyll fluorescence and XCO_2, a region is needed which should match two conditions. First, the region needs a pronounced photosynthetic activity at least during a part of the year and, second, it's geophysical conditions, especially cloud cover, should enable a reasonable amount of quality checked spectra by both the full physics and the Fraunhofer retrieval. The first condition is met by all equatorial regions as well as eastern North America and western Europe. Unfortunately, the tropics have many clouds. Consequently, the second condition is met by North America and western Europe but enforces large averaging areas in the tropics. To this end, three regions are examined: a North American region within 100°W to 55°W and 30°N to 52°N, a European region within 16°W to 50°E and 30°N to 60°N and the tropics from 23°S to 23°N. A detailed discussion of the carbon cycle in the regions is given in chapter 7. Here, a comparison of the two chlorophyll fluorescence records is given for the North American region.

The seasonal cycle of the fluorescence over North America is clearly visible in the Fraunhofer retrieved fluorescence as shown in the lower panel in figure 6.9. The top panel of figure 6.9 demonstrates the relatively poor result of the full physics fluorescence signal. Each data point is an average of the fluorescence within one month and a grid box within the North American region. The data amount is different for the two retrieval setups which complicates a robust comparison. The grid size is chosen to be 4° by 4° and 10° by 10° for the Fraunhofer retrieval and the full physics retrieval, respectively. Given these grids, the number of spectra in each grid box is on the same order for both retrievals. The amount averages to 26 and 33 spectra for the Fraunhofer and the full physics retrieval, respectively. Grid boxes containing less than three spectra per month are neglected. For the Fraunhofer retrieval in total 41,785 spectra are used to calculate 1,630 monthly grid box averages containing up to 121 spectra. On average, the mean standard deviation of each monthly average is 0.52 W m^{-2} sr^{-1} μm^{-1}. For the full physics case 9,506 spectra are used to calculate 290 monthly grid box averages containing up to 168 spectra. The mean standard deviation of each monthly average is 0.41 W m^{-2} sr^{-1} μm^{-1}. The estimated noise error of the full physics setup is 0.16 W m^{-2} sr^{-1} μm^{-1} whereas the Fraunhofer retrieval averages to a noise error of 0.41 W m^{-2} sr^{-1} μm^{-1}.

The reduced noise error of the full physics retrieval results directly from the higher information content provided by the wider spectral range. However, the full physics fluorescence record suffers from low amount of data compared to the Fraunhofer record. Moreover, the bad performance of the full physics retrieval indicates that it, additionally, suffers from higher systematic errors.

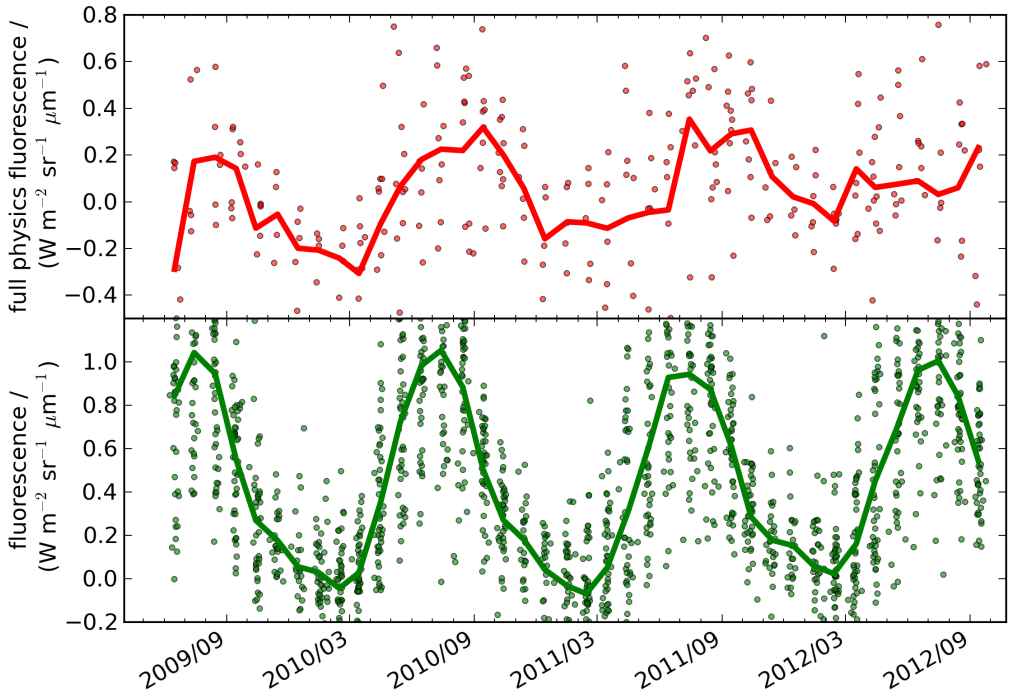

Figure 6.9.: Time series of fluorescence over a north American region. The top panel shows the fluorescence signal retrieved with the full physics setup gridded on 10° by 10°. The lower panel shows the Fraunhofer fluorescence values gridded on 4° by 4°. With these grid box sizes the number of spectra within each grid box is on the same order for both data sets. Each data point represents the monthly average of one grid cell. The corresponding time for a grid cell, for instance, which comprises one spectrum per day is in the middle of the month. As a result, the lower panel displays a vertically striped structure. The seasonal cycle of the photosynthetic activity captured by the Fraunhofer setup is recognized only partially by the full physics setup.

Table 6.1.: The same TCCON statistics as in table 4.1 but calculated for the Fluorun retrieval. The major differences are a reduced standard deviation of the bias and the higher number of spectra that converged and passed all quality checks.

TCCON	**Number**		**XCO_2 / ppm**			**XCH_4 / ppb**		
site	**collocated**	**coincident**	**bias**	**scatter**	**noise**	**bias**	**scatter**	**noise**
Bialystok	1122	709	0.14	1.92	0.76	-0.00	14.17	7.65
Bremen	1019	360	-0.35	2.29	0.8	-1.56	14.70	7.94
Karlsruhe	1352	950	-0.63	2.17	0.77	0.33	13.55	7.65
Orleans	1416	480	-0.02	2.12	0.77	1.02	12.66	7.62
Garmisch	1201	749	0.38	2.17	0.76	4.32	14.03	7.50
Park Falls	2708	2545	0.45	2.32	0.72	2.02	16.06	7.23
Lamont	5452	5218	-0.28	2.14	0.65	-0.26	17.06	6.68
Darwin	1870	1870	0.10	1.79	0.52	-4.43	11.97	5.60
Wollongong	1500	1396	0.22	1.88	0.58	-1.44	15.13	6.02
	sum	sum	std. dev.	mean	mean	std. dev.	mean	mean
	17640	14381	0.34	2.09	0.70	2.31	14.37	7.10

6.5. Impact of chlorophyll fluorescence on full physics retrieval

The full physics Fluorun, in contrast to the Baserun, corrects for the detector non-linearity and remaining spectroscopic issues via radiance offset correction and residuum retrieval. Further, the Fluorun retrieves the chlorophyll fluorescence. To evaluate the Fluorun's performance, this section applies the analyzing tools introduced in chapter 4 to it. Especially, this section focuses on the comparison to the Baserun's performance. However, first an overview of the impact shall be given.

The changes in the full physics setup map into a substantial change in both XCO_2 and XCH_4. Figure 6.10 shows two world maps revealing a change of up to 3 ppm XCO_2 and 14 ppb XCH_4 which is on the order of 1 % of the total abundance for both gases. The spatial pattern is correlated to the photosynthetic activity. The retrieval accounting for fluorescence finds lower abundances for the gases in regions with high photosynthetic activity.

The impact is higher than expected by the simulation study reported by Frankenberg et al. (2012) who found an error in XCO_2 of up to 1.0 ppm if a radiance offset and aerosols are fitted but chlorophyll fluorescence of 1.5% of the contiduum level is neglected in the retrieval.

How does this change of the full physics retrieval map into the TCCON evaluation? Table 6.1 lists the general TCCON statistics with details for each TCCON station considered in this evaluation. The same quantities are calculated and listed for the Baserun in chapter 4 in table 4.1. The lowest row summarizes the table. To directly compare both retrievals, these summaries are compiled in table 6.2 again.

Generally, three statistical quantities in these tables are most important. First, this is the number of converged spectra which passes all quality flags because a sparse data availability is a bottleneck for robust results. Second, it is the bias deviation among the TCCON sites as it represents the regional biases. Small regional biases jeopardize CO_2 surface flux inversions. Third, the single measurement precision is represented by the mean scatter of the data set.

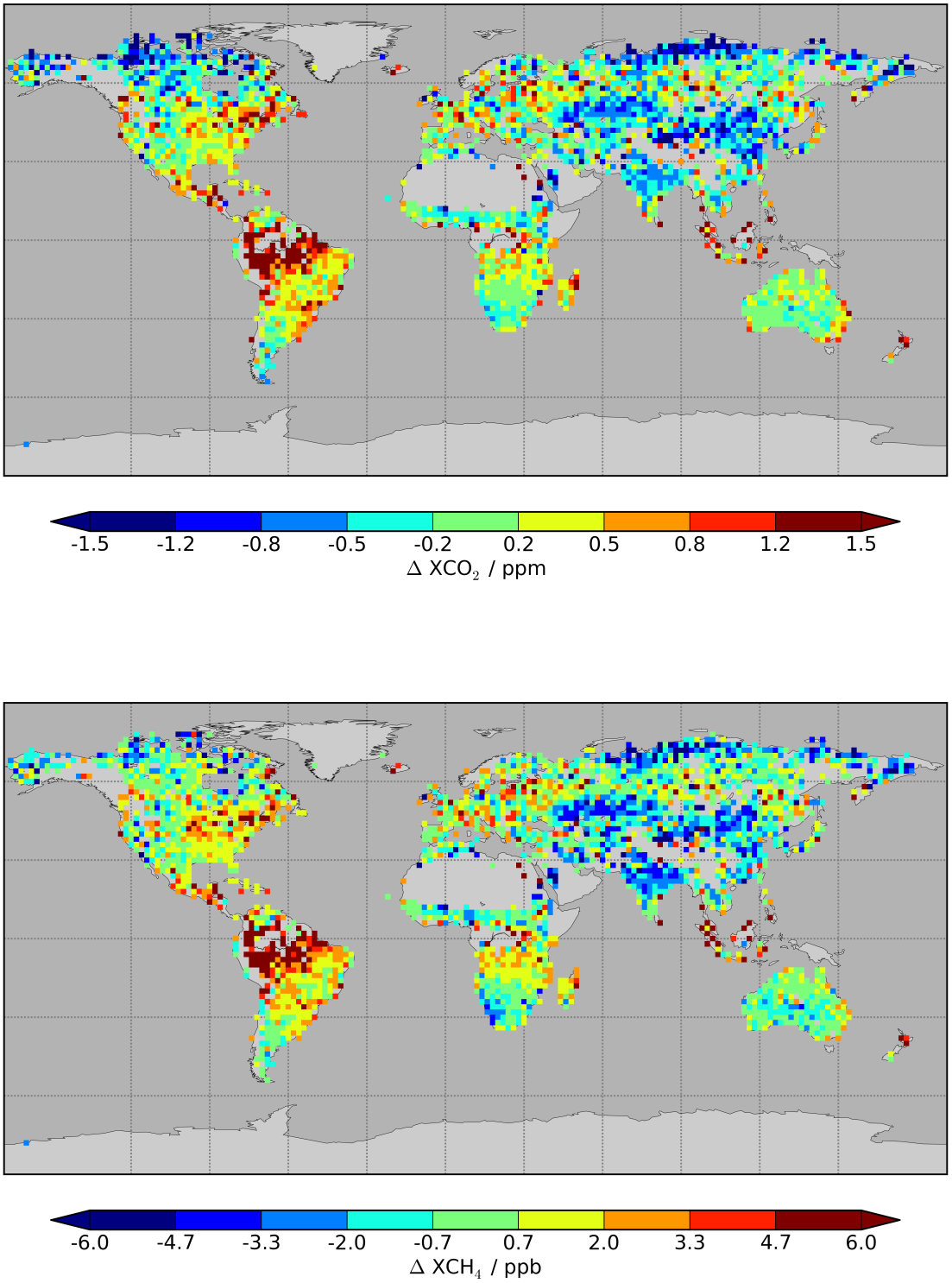

Figure 6.10.: World map of differences in XCO_2 (upper panel) and XCH_4 (lower panel) gridded on 2° by 2°. For each spectrum that passed all quality filters of both retrievals the difference is calculated. These differences are averaged within the grid box for the complete 40 month time period. The red colors indicate a higher gas abundance for the Baserun compared to the Fluorun retrieval. The regions with highest differences are quite similar for both gases and clearly correlated with regions featuring high chlorophyll fluorescence signals.

Table 6.2.: TCCON statistics. Comparison of the key statistical quantities for the Baserun and the Fluorun. The deviation of the bias among the TCCON stations is listed in column **b. dev.**. The two upper rows contain all data of the data set. The middle rows are cosampled such that only spectra are accounted in the statistics which converged and passed all quality filters of both retrieval setups. The lower two rows summarize the statistics for the bias corrected versions of the Baserun and the Fluorun.

retrieval	**Number**		**XCO_2** / ppm			**XCH_4** / ppb		
	collocated	**coincident**	**b. dev.**	**scatter**	**noise**	**b. dev.**	**scatter**	**noise**
Baserun	15817	12602	0.40	2.02	0.72	2.50	14.38	7.24
Fluorun	17640	14381	0.34	2.09	0.70	2.31	14.37	7.10
Baserun	14058	11244	0.41	1.98	0.72	2.14	14.17	7.21
Fluorun	14058	11244	0.32	2.02	0.72	2.06	14.20	7.20
Baserun bc	15817	12602	0.41	2.00	0.72	2.18	14.28	7.24
Fluorun bc	17640	14381	0.30	1.96	0.70	2.01	14.22	7.12

Accounting for chlorophyll fluorescence improves two important parameters. The number of converged spectra is increased. Additionally, the bias deviation slightly reduces for XCO_2 and XCH_4. However, the mean scatter remains virtually the same for XCH_4 and slightly deteriorates for XCO_2. To avoid sampling biases, the statistics was recalculated counting only those spectra which converge and pass all quality checks of both retrievals. The summary is listed in the middle section of table 6.2. Accordingly, the statistics changes little with different sampling.

The time series of the GOSAT data at the two TCCON sites Lamont and Wollongong is shown in the first and third panel from top in figure 6.11. This is the same illustration as in figure 4.2 for the Baserun. Additionally, figure 6.11 compares monthly averages of all three data sets at the two TCCON sites in the second and forth panel from top. Following the evolution of the monthly averages, sometimes the Fluorun better matches the TCCON values than the Baserun and sometimes it is vice versa. Compare, for instance, at the Lamont TCCON site the months August and September in the year 2009 to the same months in the year 2010.

A very important tool to identify systematic errors in a retrieval scheme are the error correlation plots already shown previously in this work. The errors are given by the single measurement difference between a collocated GOSAT TCCON measurement pair. This error can be plotted and tested for correlation with any available parameter. One could distinguish between geophysical parameters, instrument and measurement geometry driven parameters, and rather internal retrieval concept parameters. Important geophysical parameters are the aerosol load, the ground scene albedo, the atmospheric humidity, and variation in the surface elevation. Typical instrument and geometry parameters are the solar and viewing zenith angle, the airmass factor, and the signal to noise ratio. Internal retrieval parameters are, for instance, the degrees of freedom (DFS) for scattering or a target gas profile, the retrieval error, and number of iterations in the inversion routine. The development of a retrieval scheme requires careful analysis of such error correlations. Additionally, interdependencies of the mentioned parameters might hint to erroneous or correct implementation of a retrieval parameter.

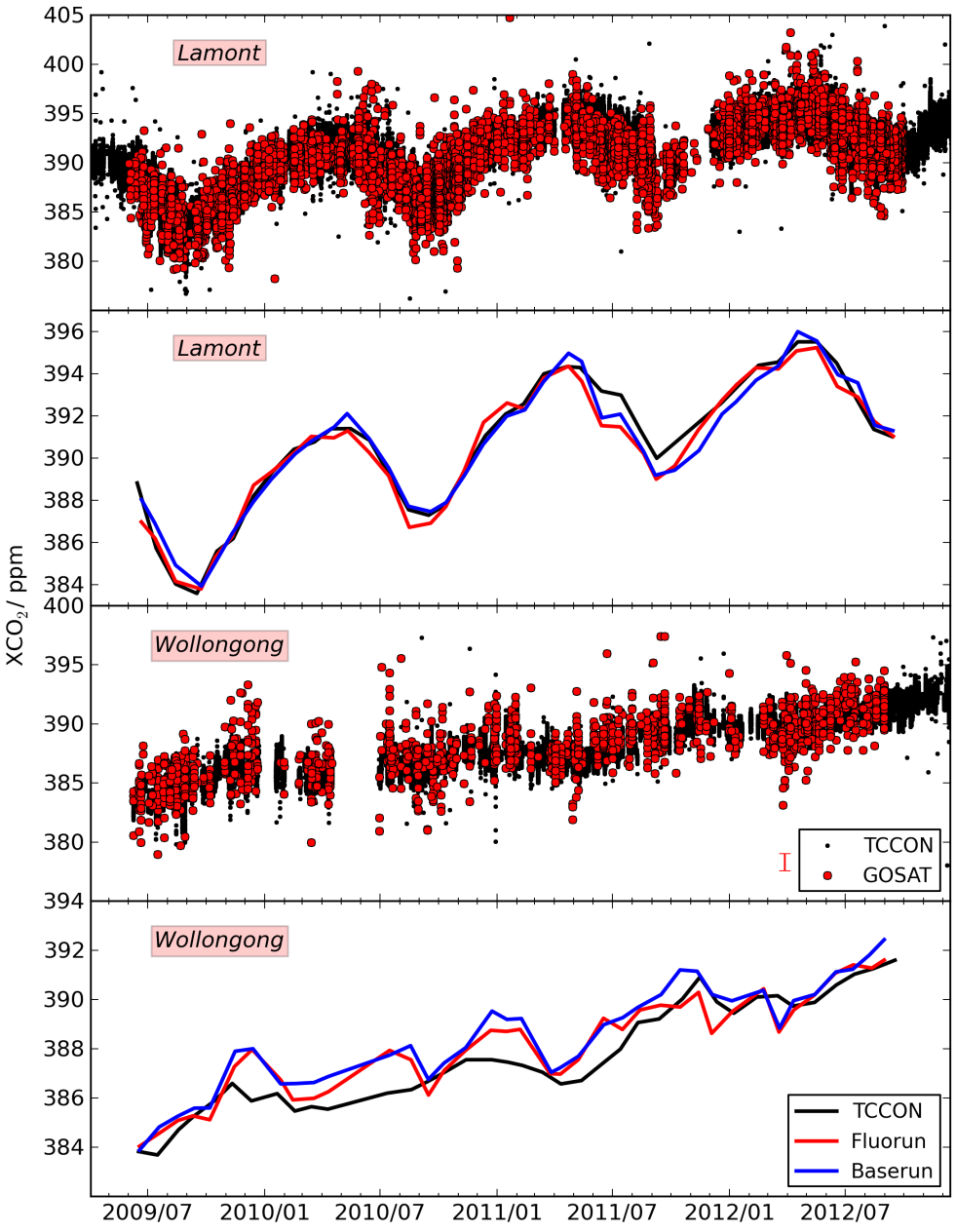

Figure 6.11.: XCO_2 time series for two TCCON stations. The first and third panel from top show single measurement comparisons. The second and fourth panel from top show monthly averages for three data sets. Generally, the GOSAT data (Fluorun, red) reveal a higher scatter compared to the TCCON data which is partially due to noise error, partially due to systematic errors and partially it might be a different sampling of the variability in the XCO_2 signal. The mean noise error of the retrieval is represented by the error bar next to the legend. Looking at the monthly averages it is hardly possible to tell which GOSAT data set matches best with the TCCON data set.

From the examined correlations 15 error correlations are exemplary presented in figure 6.12 and 6.13 as well as similar figures in chapters 3 and 4, and in the Appendix. The choice comprises parameters that are important for the chlorophyll fluorescence retrieval using the O_2 A-band. These are the albedo in the O_2 A-band, the full physics fluorescence parameter, the mean signal in the O_2 A-band, and the time of the year. Additionally, the parameter set comprises the three aerosol parameters, the blended albedo, the airmass factor, χ^2, the solar zenith angle, the H_2O total column number density, the retrieval error, the DFS for CO_2 or CH_4, and, finally, the DFS for scattering. For a description of the parameters see chapter 3.

If a retrieval error correlates to a parameter, due to a systematic retrieval error, the dependency can be determined. To avoid systematic biases which could jeopardize inverse surface flux models, it is common to provide a bias corrected data set to the users, see section 4.1.4.

The Fluorun's bias correction is driven by the parameters O_2 A-band albedo (ALB_{O_2}), scattering optical thickness (SOT), and aerosol layer height (height) and scattering optical thickness and aerosol size distribution (α) for XCO_2 and XCH_4, respectively. The complete formulations are:

$$XCO_{2,BC} = XCO_2 \cdot \left(1.005185 - ALB_{O_2} \cdot 0.015 + SOT \cdot 0.015 - height \cdot 2 \cdot 10^{-7}\right) \quad (6.1)$$

$$XCH_{4,BC} = XCH_4 \cdot (1.02205 + SOT \cdot 0.04 - \alpha \cdot 0.005) \quad (6.2)$$

Where the subscript BC denotes the bias corrected quantities. The height given in meters is divided by its unit.

Figures 6.12 and 6.13 present both the raw data set and the bias corrected data set. Unfortunately, the uncorrected Fluorun data set is stronger correlated than the Baseruns' raw data set. Nevertheless, the bias correction itself remedies the found correlations significantly which is not the case for the Baserun's bias correction. Accordingly, the lowest rows of table 6.2, summarizing the statistic of the bias corrected data sets, reflects only an improvement of the Fluorun's statistics.

Figure 6.14 shows how the bias correction spatially influences the XCO_2 and XCH_4 difference between the Fluorun and the Baserun. Generally, the bias correction masks the chlorophyll fluorescence patterns. The strong differences in the tropics are transfered to the northern hemisphere latitudes. Especially, over North America the Fluorun retrieves lower XCO_2 and XCH_4 abundances than the Baserun.

Taken together, accounting chlorophyll fluorescence is a conceptual improvement of the full physics retrieval which results in a higher number of converging spectra and a slightly reduced regional bias. Indeed, it has a significant impact on the XCO_2 and XCH_4 retrieval. However, the TCCON validation is ambiguous.

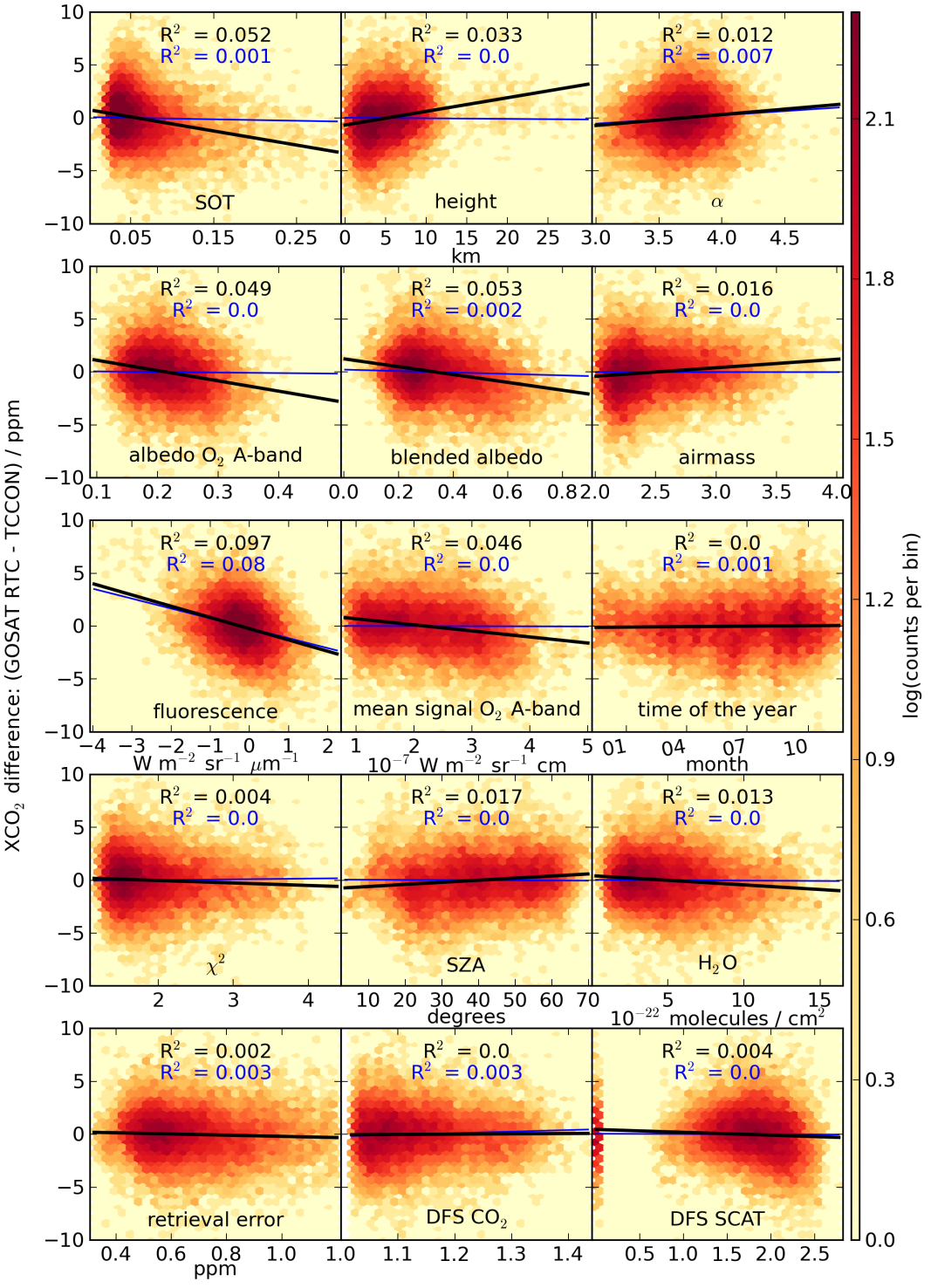

Figure 6.12.: XCO_2 error correlation plots. Two dimensional histogram with linear regression (black) and Pearson correlation coefficient R^2 as shown in figure 4.3 for the Baserun retrieval. The error correlations for the Fluorun shown here are stronger revealing R^2 values up to roughly 0.05 for the albedo and aerosol parameters which is below 0.01 in the Baserun. The bias corrected data, see equation 6.1, exhibit very low correlations as indicated by the blue regression line and R^2. The Appendix lists histograms of the bias corrected data.

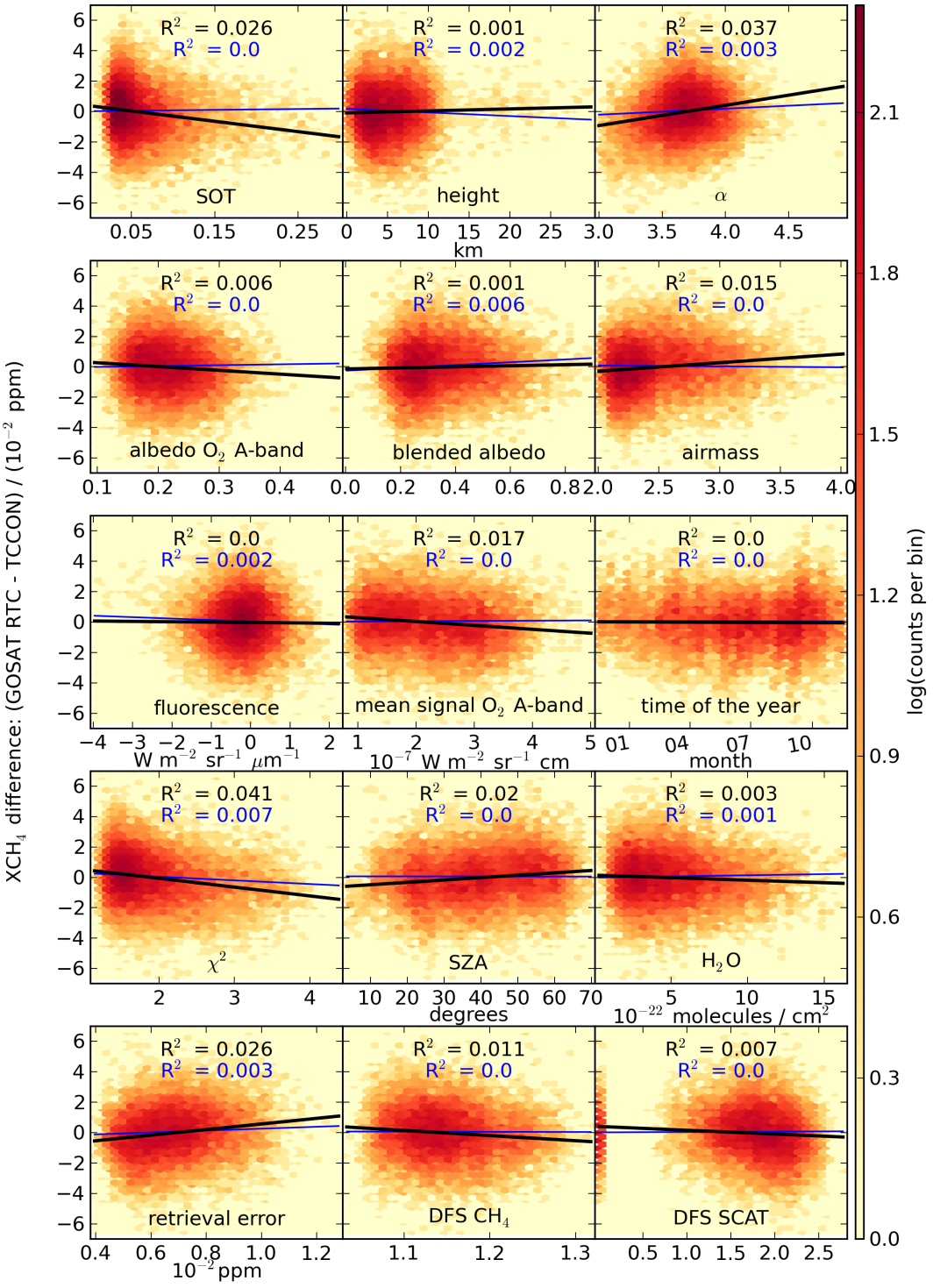

Figure 6.13.: XCH_4 error correlation plots. Same illustration as in figure 6.12 for XCH_4. The error correlations of the Fluorun XCH_4 are not as high as for the Fluorun XCO_2 which is the same behavior for the Baserun XCH_4. The affect of the two parameter based bias correction from equation 6.2 is indicated in blue.

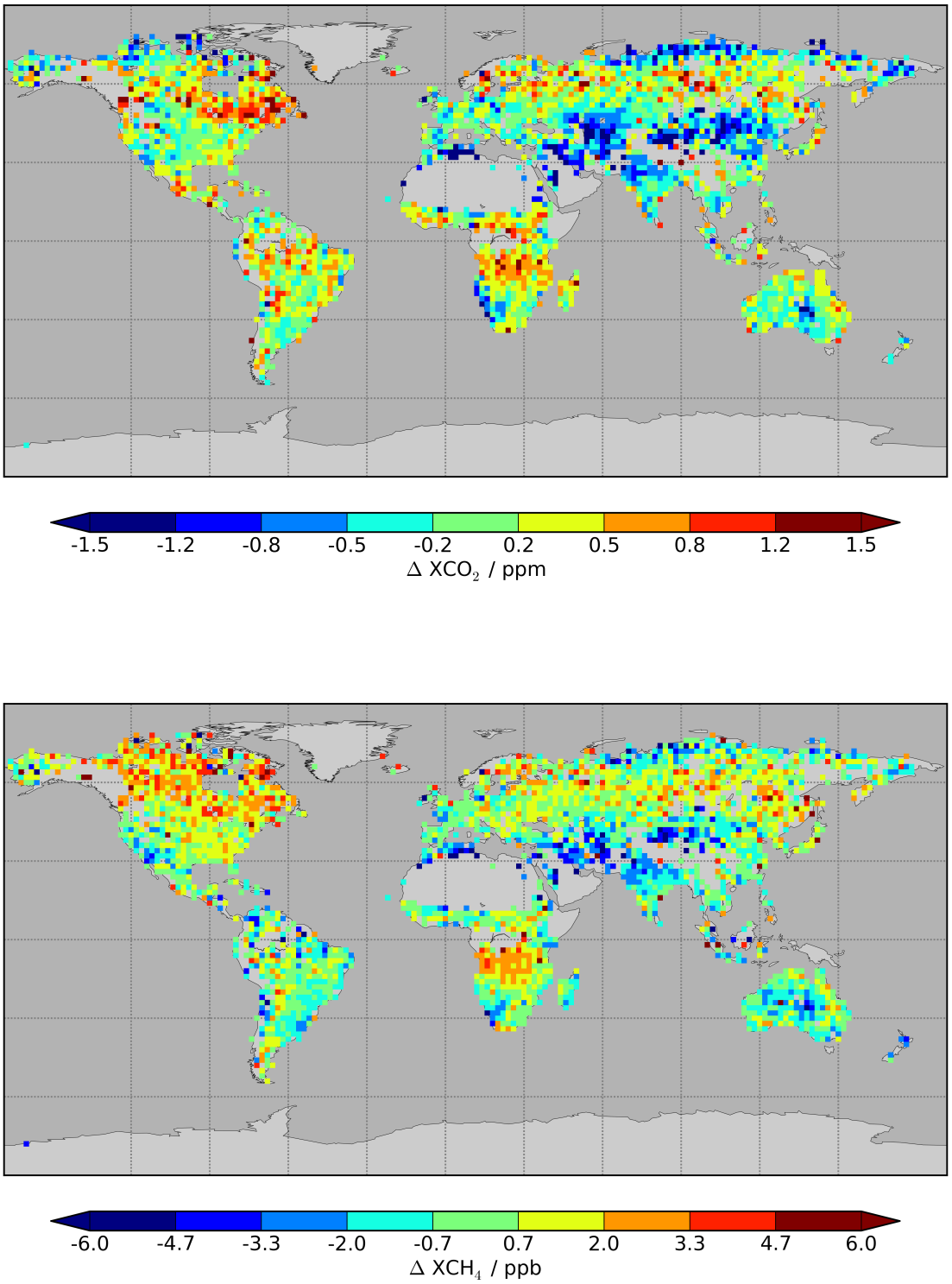

Figure 6.14.: World map of differences as in figure 6.10 after applying the bias correction to the data set. The patterns of high differences are less congruent with the chlorophyll fluorescence patterns. The bias correction shifts parts of the differences to the higher northern latitudes.

6.6. Assessing the impact of apriori CO_2 and CH_4 profiles on the validation.

Generally, the validation of GOSAT soundings with TCCON measurements is convenient. TCCON provides intracalibrated XCO_2 and XCH_4 measurements for many stations around the world. Moreover, both instrument types measure total column dry air mixing ratios from spectroscopic soundings which enables direct comparison. However, differences in the retrieval scheme may result in incomparable quantities.

An overview of the inversion scheme is given in section 3.6. Disregarding the error terms, equation 3.29 can be rearranged to:

$$\hat{\vec{x}}_i = \mathbf{A}_i \vec{x}_{true} + (1 - \mathbf{A}_i)\vec{x}_{a,i} \tag{6.3}$$

Where the subscript i indicates the instrument and retrieval scheme, either it is TCCON or it is RemoTeC. $\vec{x}_{true}$ embodies the true atmospheric state. $\hat{\vec{x}}_i$ denotes the estimated state vector comprising the XCO_2 and XCH_4 values. Further, $\vec{x}_{a,i}$ serves as the first guess in the inversion and comprises the apriori knowledge of the atmospheric state. Finally, $\mathbf{A}_i$ represents the averaging kernel expressing the measurement's sensitivity.

The effects of different apriori target gas profiles and averaging kernels have so far been assumed small. Hitherto, this work calculated the GOSAT RemoTeC difference with respect to TCCON from $\hat{\vec{x}}_{RemoTeC} - \hat{\vec{x}}_{TCCON}$. Instead, now $\hat{\vec{x}}_{RemoTeC}$ is substituted by $\hat{\vec{x}}^*_{RemoTeC}$ with:

$$\hat{\vec{x}}^*_{RemoTeC} = \hat{\vec{x}}_{RemoTeC} - (1 - \mathbf{A}_{RemoTeC})\vec{x}_{a,RemoTeC} + (1 - \mathbf{A}_{RemoTeC})\vec{x}_{a,TCCON} \tag{6.4}$$

This substitution cancels out differences caused by the different apriori CO_2 profiles used in the TCCON and RemoTeC inversions.

Following the TCCON evaluation of the previous section, figures 6.15 and 6.16, again, show the error correlation to the chosen 15 parameters for XCO_2 and XCH_4, respectively. The errors calculated with the RemoTeC apriori being substituted by the TCCON apriori are plotted in the histograms along with the respective linear regression and Pearson coefficient illustrated in black. For direct comparison, the linear regression and Pearson coefficient from figure 6.12 are shown in blue.

Using the TCCON apriori reduces the error correlation of XCO_2 for practically every parameter. However, for XCH_4 the TCCON apriori raises most error correlations. Despite this inconclusive behavior, the impact is on a significant order. Note that for both target gases a small seasonal correlation is induced by the use of the TCCON apriori. Of course, such a behavior is important to analyze because neglecting the chlorophyll fluorescence seasonally affects the measurements.

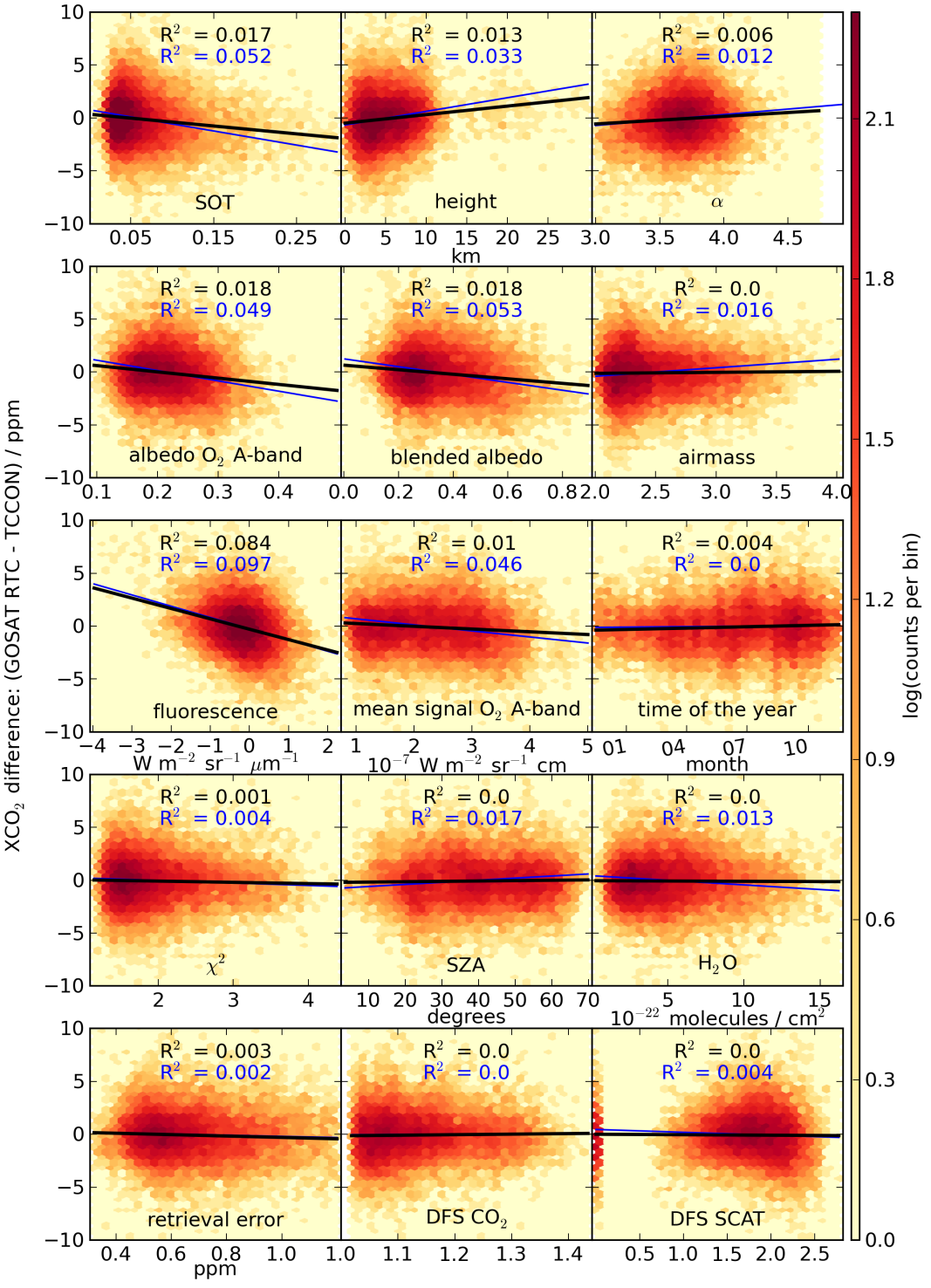

Figure 6.15.: XCO_2 error correlation plot. The impact of the apriori substitution is illustrated in comparison to the original RemoTeC apriori (blue, taken from figure 6.12. The XCO_2 error correlations reduce significant when substituting the RemoTeC apriori by the TCCON apriori. Only a small seasonal dependence is induced as shown in the right histogram of the middle panel called 'time of the year'.

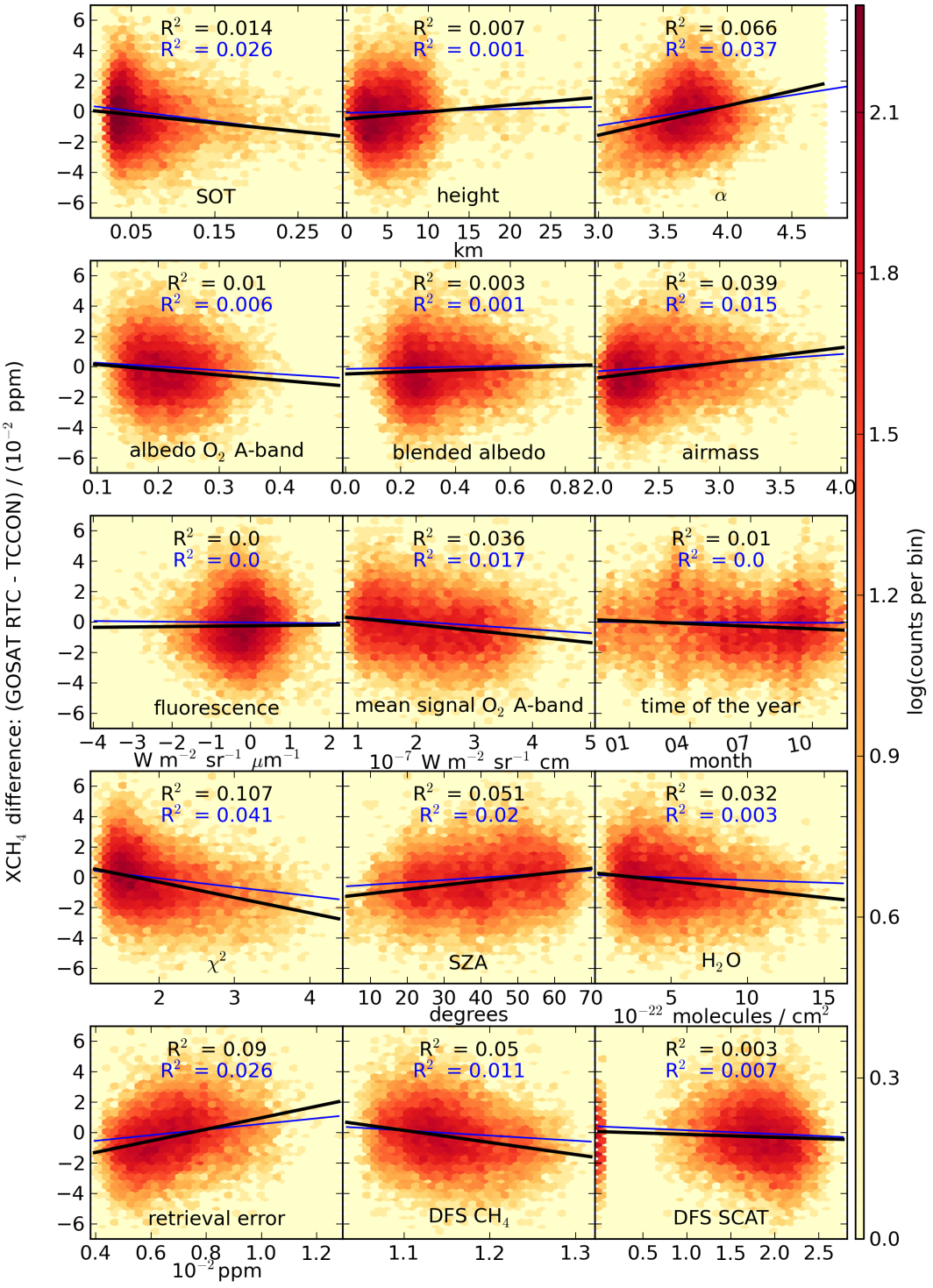

Figure 6.16.: XCH_4 error correlation plot. As in figure 6.15 the data set with RemoTeC apriori (blue) is compared to the data set with TCCON apriori (black). In contrast to XCO_2, the XCH_4 error correlation rather increases when exchanging the RemoTeC apriori by the TCCON apriori.

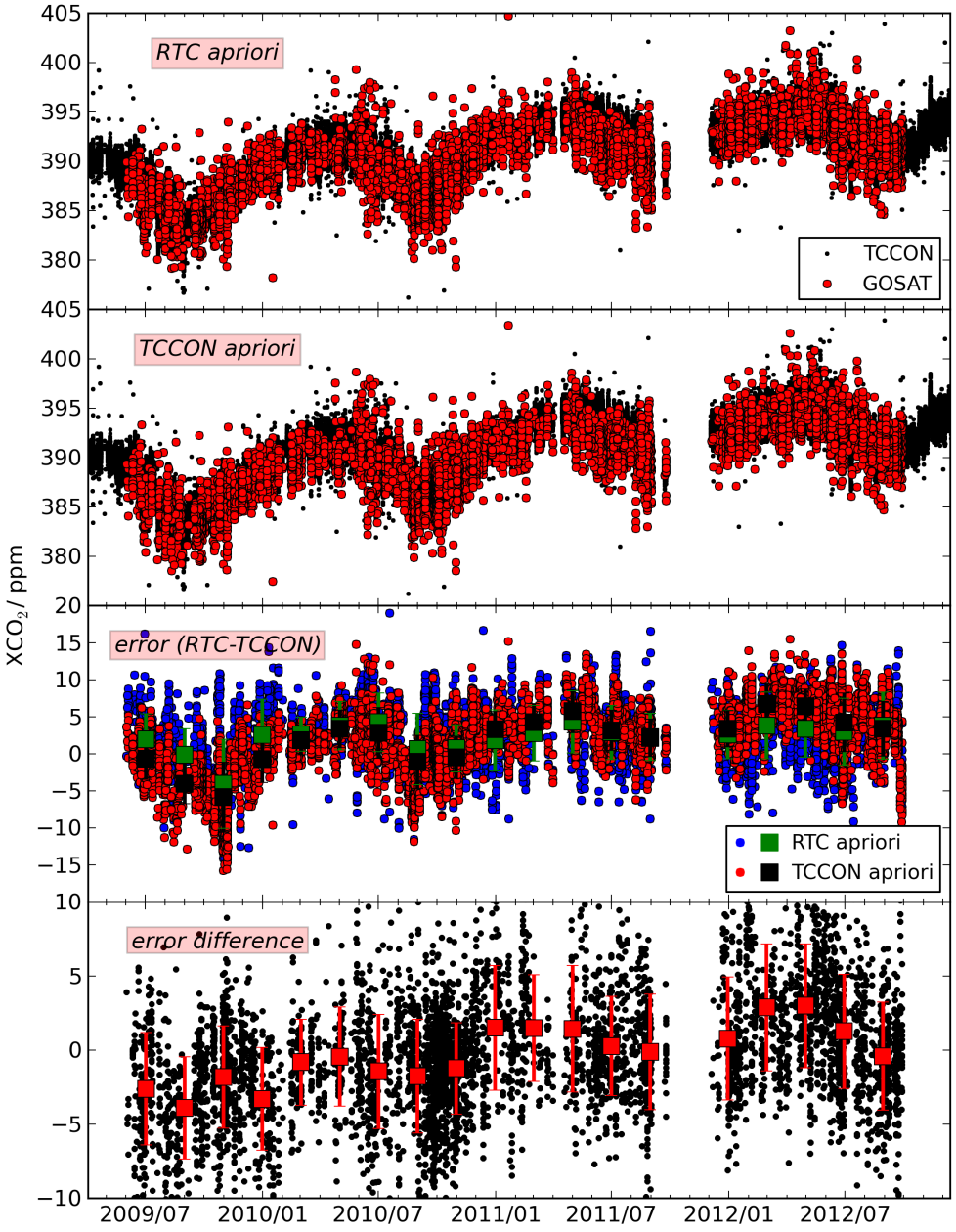

Figure 6.17.: Analyzing the different seasonality of the apriori CO_2 profiles. The upper two panels show the time series of the collocated GOSAT TCCON pairs, which both the RemoTeC apriori and the TCCON apriori, respectively. The third panel from top contains the single measurement errors of both data sets along with running mean values for every two months. The standard error is attached to every running mean. The subsequent panel plots in black the differences between the errors, shown in blue and red in the panel above, again, along with running mean values.

Indeed, this rather small error correlation points to a systematic difference between the distinctive apriori profiles of TCCON and RemoTeC. Figures 6.17 and 6.18 analyze the temporal differences of the RemoTeC and the TCCON aprioris at the Lamont TCCON site for both XCO_2 and XCH_4, respectively. The upper two panels show the time series of collocated GOSAT and TCCON soundings with the RemoTeC apriori profiles and the substituted TCCON apriori profiles. The third panel from top shows the single measurement error for both data sets along with monthly averages and their respective standard deviation. The lower most panel plots the differences of the single measurement errors, again, with monthly averages and their respective standard deviation.

The single measurement errors of the Fluorun with the standard RemoTeC apriori profiles reveal a small seasonal cycle. This is evident for XCO_2 and for XCH_4 which themselves possess a weak seasonal cycle compared to XCO_2. Having exchanged the apriori profiles, the seasonal amplitude of the single measurement error increases. Accordingly, the apriori induced differences comprise a seasonal pattern. In contrast to XCH_4, a trend is detectable for the RemoTeC estimates of XCO_2. In the beginning of the time series, the RemoTeC XCO_2 estimates, including the RemoTeC apriori profiles, rather overestimate the XCO_2 with respect to TCCON measurements. In the end of the time series, RemoTeC rather underestimates the XCO_2 with respect to TCCON measurements.

Is the error seasonality affected by neglecting chlorophyll fluorescence? TCCON measurements are in good approximation not affected by chlorophyll fluorescence signals because TCCON measures direct sunlight. Hence, a change in the error seasonality due to accounting or neglecting chlorophyll fluorescence in the full physics retrieval could be a measure for a successful improvement.

To this end, figure 6.19 compares monthly averaged time series of the GOSAT RemoTeC and TCCON differences, extracted from the third panel of the figures 6.17, 6.18, and the corresponding Baserun figures listed in the Appendix. The top panel plots the monthly mean error of the GOSAT data set using the standard RemoTeC XCO_2 apriori profiles. The second panel shows the same but substituted the RemoTeC XCO_2 apriori profiles by the ones TCCON uses. The lower two panels illustrates the same for XCH_4. Indeed, the seasonality of the mean errors changes. Unfortunately, the difference in the seasonality ignores the retrieval concept contrast of the Baserun and the Fluorun. Of course, the chlorophyll fluorescence intensity around the Lamont TCCON site is relatively low. As a result, the impact of accounting chlorophyll fluorescence in the retrieval is minor. Nevertheless, the difference in the error seasonality applies to the substitution of the apriori profiles. The seasonality of the errors is higher in case the RemoTeC apriori profiles are substituted by the TCCON apriori profiles. Further, the standard deviation of the monthly error average is somewhat reduced by the substitution. For instance, the standard deviation of the monthly Fluorun XCO_2 errors drops on average from 3.74 ppm to 2.77 ppm and the standard deviation of the monthly Fluorun XCH_4 errors drops on average from 20.14 ppb to 16.89 ppb. Note the different y-axis scales for the different panels in figure 6.19.

Conceptually, the apriori profile substitution is an improvement of the TCCON validation as it reduces the systematic difference of the two retrievals, see equation 6.4. However, the seasonality of the error is enhanced. Thus, the different apriori profiles might have masked a systematic discrepancy between TCCON retrievals and RemoTeC GOSAT retrievals.

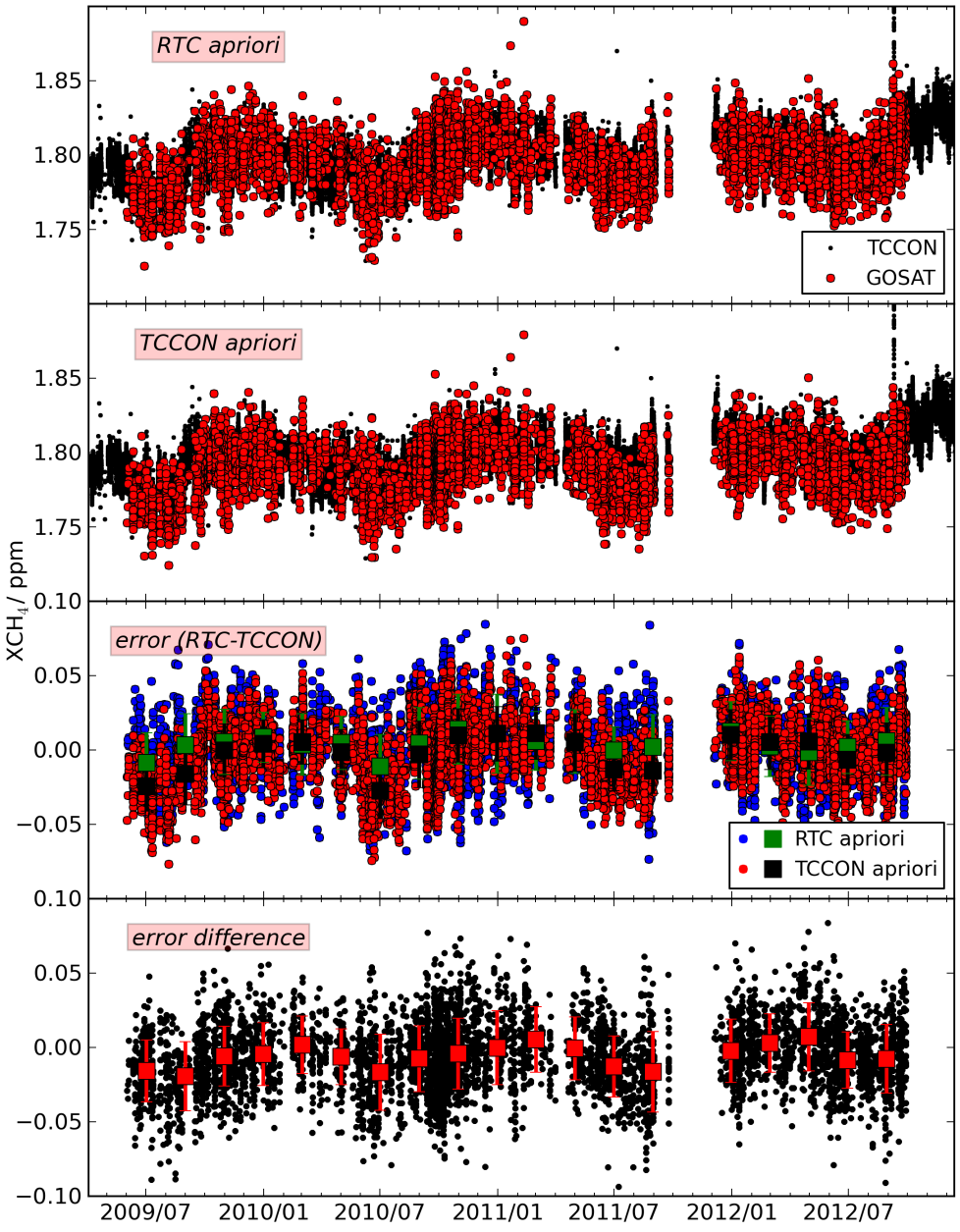

Figure 6.18.: Analyzing the different seasonality of the apriori CH_4 profiles. Same illustration as in figure 6.17 but for XCH_4 which exhibits a less pronounced seasonal cycle than XCO_2. Using the TCCON apriori XCH_4 profile induce a more pronounced seasonal cycle in the GOSAT errors with respect to TCCON.

Table 6.3.: The same TCCON statistics as in table 6.1 for the Fluorun but the RemoTeC apriori is substituted by the TCCON apriori, see equation 6.4. For direct comparison the lowest row contains the statistics without the substitution taken from table 6.1. Note that the data base is not exactly the same because the new TCCON data set containing the apriori information is for instance not available for the Bremen TCCON site.

TCCON	**Number**		**XCO_2** / ppm			**XCH_4** / ppb		
site	**collocated**	**coincident**	**bias**	**scatter**	**noise**	**bias**	**scatter**	**noise**
Bialystok	1122	709	0.14	1.92	0.76	9.17	15.89	7.65
Karlsruhe	1352	950	-0.48	2.23	0.77	6.57	15.38	7.65
Orleans	1416	615	0.24	2.08	0.77	2.82	14.07	7.62
Garmisch	1201	781	0.57	2.31	0.76	8.07	15.08	7.5
Park Falls	2708	2545	0.38	2.25	0.72	2.1	16.43	7.23
Lamont	5452	5223	-0.28	2.12	0.65	-4.21	16.52	6.68
Darwin	1870	1870	-0.09	1.69	0.52	-11.1	11.71	5.6
Wollongong	1500	1396	-0.49	1.93	0.58	-13.43	14.91	6.02
	sum	sum	std. dev.	mean	mean	std. dev.	mean	mean
	14089	16621	0.37	2.07	0.69	8.11	15.0	6.99
RTC apr.	14381	17640	0.34	2.09	0.70	2.31	14.37	7.10

Following the statistical analyzes of the previous section, table 6.3 recalculates the table 6.1 accounting for the substituted apriori profiles. For direct comparison, the lower most row repeats the concluding row from table 6.1. Substituting the apriori profiles leaves the data set's scatter indifferent. In contrast, the bias deviation among the TCCON stations is affected, especially for XCH_4. Thus, the influence of the apriori profiles is important and requires further investigation. Other limitations of the validation, for instance, due to low number of TCCON spectra for challenging space borne measurement conditions, are discussed in section 4.1.5.

This chapter discussed the updates of the RemoTeC Fluorun compared to the RemoTeC Baserun. The updates comprise the chlorophyll fluorescence retrieval, a dedicated radiance offset correction, and a residuum retrieval. The full physics chlorophyll fluorescence record is shown to be too negative compared to the reliable chlorophyll fluorescence record retrieved with the Fraunhofer retrieval. Furthermore, the full physics chlorophyll fluorescence record is too sparse and too noisy to provide valuable information on gross primary production. Further, this chapter evaluated the Fluorun's XCO_2 and XCH_4 record with TCCON measurements and this chapter discussed that the TCCON validation is limited by sparse global coverage especially in photosynthetic active regions and that the TCCON validation should account for the apriori target gas profiles. The comparison of the two full physics RemoTeC setups showed that the new Fluorun and is tentatively better than the former Baserun.

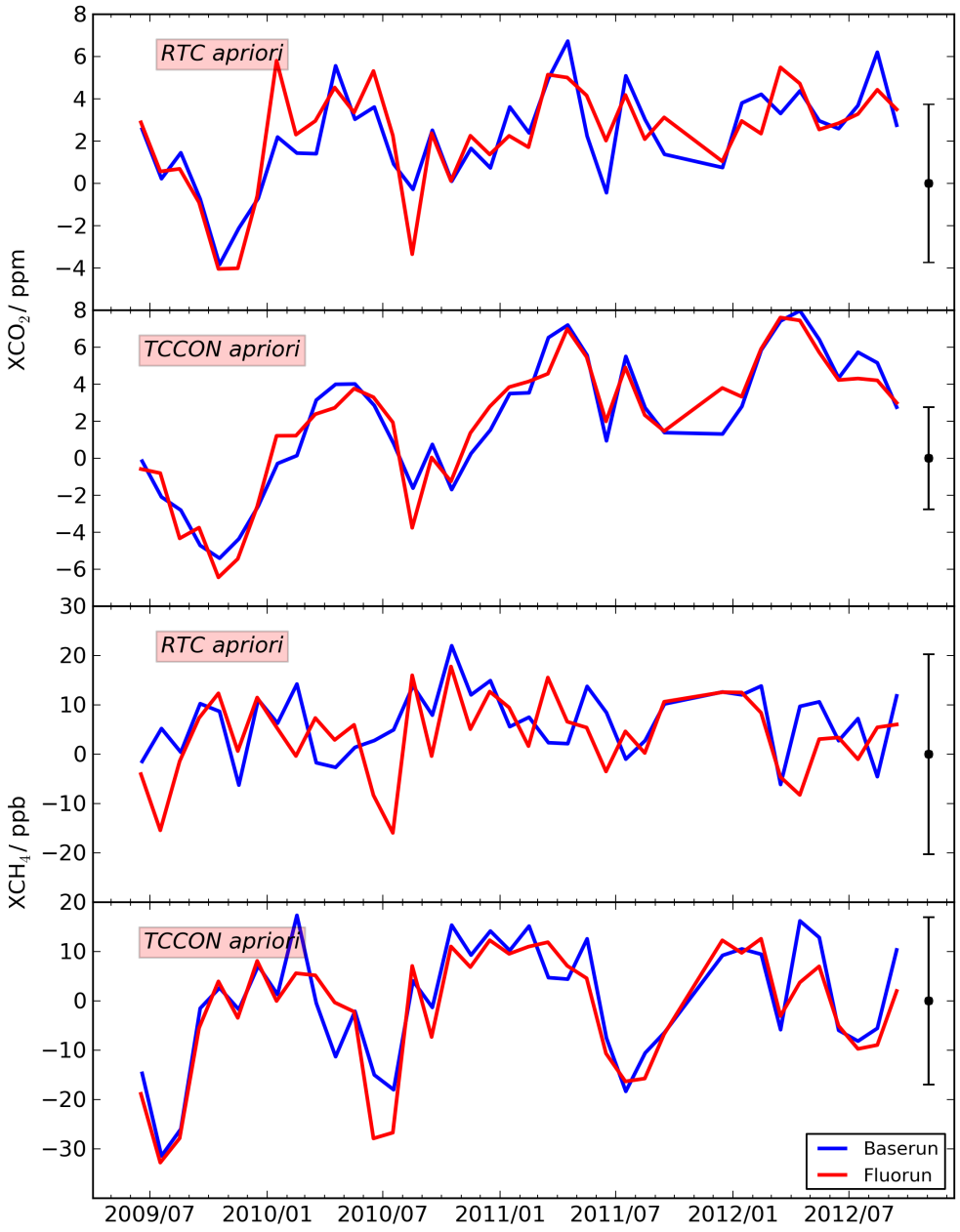

Figure 6.19.: Time series at Lamont of differences between GOSAT RemoTeC and TCCON. The two top panels show the monthly mean difference between XCO_2 RemoTeC retrievals and TCCON measurements at Lamont in blue for the Baserun and in red for the Fluorun. The first panel from top plots the data set using the standard RemoTeC XCO_2 apriori, these are the green squares from the third panel of figure 6.17 and the respective one in the Appendix. The second panel from top plots the data set using the substituted XCO_2 aprioris from TCCON, these are the black squares from the third panel of figure 6.17 and the respective one in the Appendix. The lower two panels illustrates the same differences for XCH_4. At the right side of each time series the average of the standard deviation is shown.

7. Insights in the carbon cycle

The previous chapters presented the retrieval of XCO_2 and two concepts to retrieve chlorophyll fluorescence signals from GOSAT observations. Chlorophyll fluorescence can be retrieved reliable by the Fraunhofer retrieval setup on a monthly 4° by 4° grid. In contrast, the full physics retrieval of chlorophyll fluorescence is too sparse and not reliable. However, chlorophyll fluorescence needs to be taken into account in the full physics retrieval because it tentatively improves the XCO_2 and XCH_4 record. This chapter provides insights in the carbon cycle gained by the GOSAT XCO_2 and chlorophyll fluorescence observations in section 7.1. Further, section 7.2 shows how CO_2 surface flux estimates are influenced by accounting chlorophyll fluorescence in the GOSAT XCO_2 retrievals. Finally, section 7.3 points out regional constraints on both the net biogenic carbon flux and the photosynthetic carbon sink as well as the impact of regarding chlorophyll fluorescence in the retrieval of XCO_2 on the net biogenic fluxes.

7.1. Observing changes in atmospheric CO_2 and photosynthetic activity

Subsection 7.1.1 presents the estimation of the XCO_2 background increase due to anthropogenic emissions and natural long term CO_2 surface flux changes. Subsection 7.1.2 discusses the natural carbon cycle which is driven by respiration and carbon fixation due to photosynthesis.

7.1.1. Background increase of atmospheric CO_2

To examine the natural carbon cycle, the annual increase of XCO_2, mainly caused by anthropogenic carbon emissions, has to be subtracted from the XCO_2 record. To perform this detrending, the background signal is estimated for all processed and quality checked GOSAT soundings. Further, the background XCO_2 increase is compared to independent ground based estimates.

Figure 7.1 summarizes the global XCO_2 record of the RemoTeC Fluorun retrieval. The averages of XCO_2 retrievals within three 60° latitudinal zones are shown in blue. To avoid domination by latitudes with a high number of measurements, first, the monthly averages in each 2° by 2° grid box are calculated then these XCO_2 averages are again

averaged. The red squares represent 12 months running mean values. For each month the prior six months and the posterior six months are averaged. Accordingly, the running mean of December 2010 averages all XCO_2 values from start of June 2010 till end of May 2011. Having a time series that includes 40 months, this procedure yields only 28 monthly background XCO_2 estimates. These running means evolve smoothly with time. Thus, a linear inter- and extrapolation (black solid line) gives, per 60° latitudinal zone, a good approximation of the background XCO_2 increase within the whole 40 months time period.

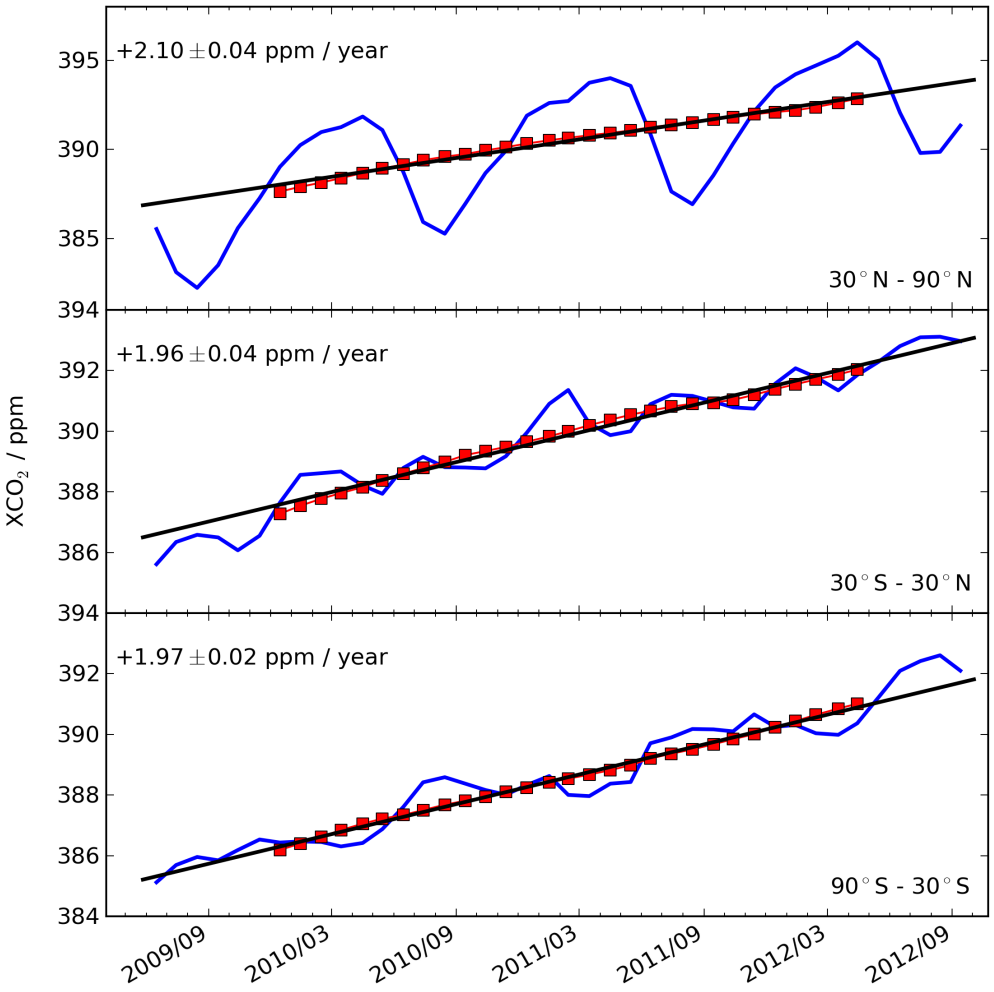

Figure 7.1.: Annual increase of Fluorun XCO_2 for three 60° latitudinal zones. The latitude range of each zone is indicated in the lower right corner of each panel. All XCO_2 measurements within one month are averaged from 2° by 2° grid box averages (blue line). Red squares show XCO_2 running means for one year, e.g. for December 2010 all values are averaged from beginning of June 2010 till end of May 2011. The black line represents a linear fit to the running means, extrapolated for the first and last six months of the regarded period. Its slope gives the annual increase in XCO_2 and is denoted in the top left of each panel. Its error is the regression's standard error.

The Earth System Research Laboratory (ESRL) from the National Oceanic and Atmospheric Administration (NOAA) operates a research station at Mauna Loa (Hawaii) which is often used as standard for this background subtraction[1]. They provide information about the annual increase at Mauna Loa. They calculate a seven year running mean for each month to correct for seasonal effects and estimate the annual increase per year with an uncertainty of 0.11 ppm per year. For the years 2009 till 2012, which are considered in this work, XCO_2 increased by 1.89 ppm, 2.43 ppm, 1.84 ppm and 2.66 ppm, respectively. With equal weights per year and the assumption that the error is not reduced for a four year average these values average to 2.21 ± 0.11 ppm per year which is in agreement with the GOSAT data set in the northern hemisphere in figure 7.1 (upper panel). Likewise, the corresponding background increase of the Baserun XCO_2 record is consistent with the reported Mauna Loa increase. The Appendix contains the corresponding figure A.8.

7.1.2. The Seasonal cycle of atmospheric CO_2 and chlorophyll fluorescence

To examine the natural seasonal cycle of XCO_2 the anthropogenic driven annual increase in XCO_2 is subtracted from the XCO_2 record. The regarded chlorophyll fluorescence record is retrieved with the Fraunhofer retrieval concept. The seasonal cycle of XCO_2 is mainly driven by the carbon uptake by photosynthesis opposing the carbon release through respiration. Figure 7.2 demonstrates the relationship between the XCO_2 cycle and the chlorophyll fluorescence cycle in the northern hemisphere. The amplitude of the chlorophyll fluorescence cycle fades with higher latitudes. In addition, the northern latitudes exhibit a steeper cycle with later onset. On the contrary, the amplitude of the XCO_2 cycle rises with higher latitudes. The XCO_2 cycle persistently reaches its yearly minimum posterior to the chlorophyll fluorescence peak. Generally, at this scale the inter annual variation is minor.

To have a closer look at the carbon cycle, this section presents details for three regions. According to the description in section 6.4, the regions feature a high chlorophyll fluorescence activity and a sufficient number of quality checked full physics retrievals. First, a region over North America is analyzed by five comparative time series in figure 7.3. The region, comprising 45° longitude and 22° latitude, is split into grid cells. All measurements are monthly averaged within each grid cell. According to the amount of available data and the respective scatter, the grid size is different for the Fraunhofer and the full physics data set. The chlorophyll fluorescence data, retrieved with the Fraunhofer concept, are gridded on 4° by 4° latitude and longitude. See section 5.5.2 for an analysis of the grid size versus noise. For chlorophyll fluorescence a monthly mean of a grid cell is calculated only if at least three spectra are available. In contrast, the full physics XCO_2 data set considers each spectrum and grids the area on 2° by 2° latitude and longitude. Although the number of XCO_2 grid cells is four times higher than the fluorescence grid cell number, the monthly chlorophyll fluorescence averages might outnumber the monthly XCO_2 means.

The first two panels from top of figure 7.3 show the monthly grid cell averages of XCO_2 and chlorophyll fluorescence, respectively. Each data point corresponds to a monthly average of a single grid cell. The time of each data point is simply the temporal average of the contained spectra. Thus, if a grid cell contains measurements homogeneously distributed throughout the month, its time is centered in the month. Especially, for chlorophyll fluorescence, a clustering of the data points in the middle of each month is visible. In addition to the data points, a solid line links monthly means of the data points. The errors of the means are omitted for clarity in figure 7.3.

[1] webpage: http://www.esrl.noaa.gov/gmd/ccgg/trends/ (visited on 3rd February 2015)

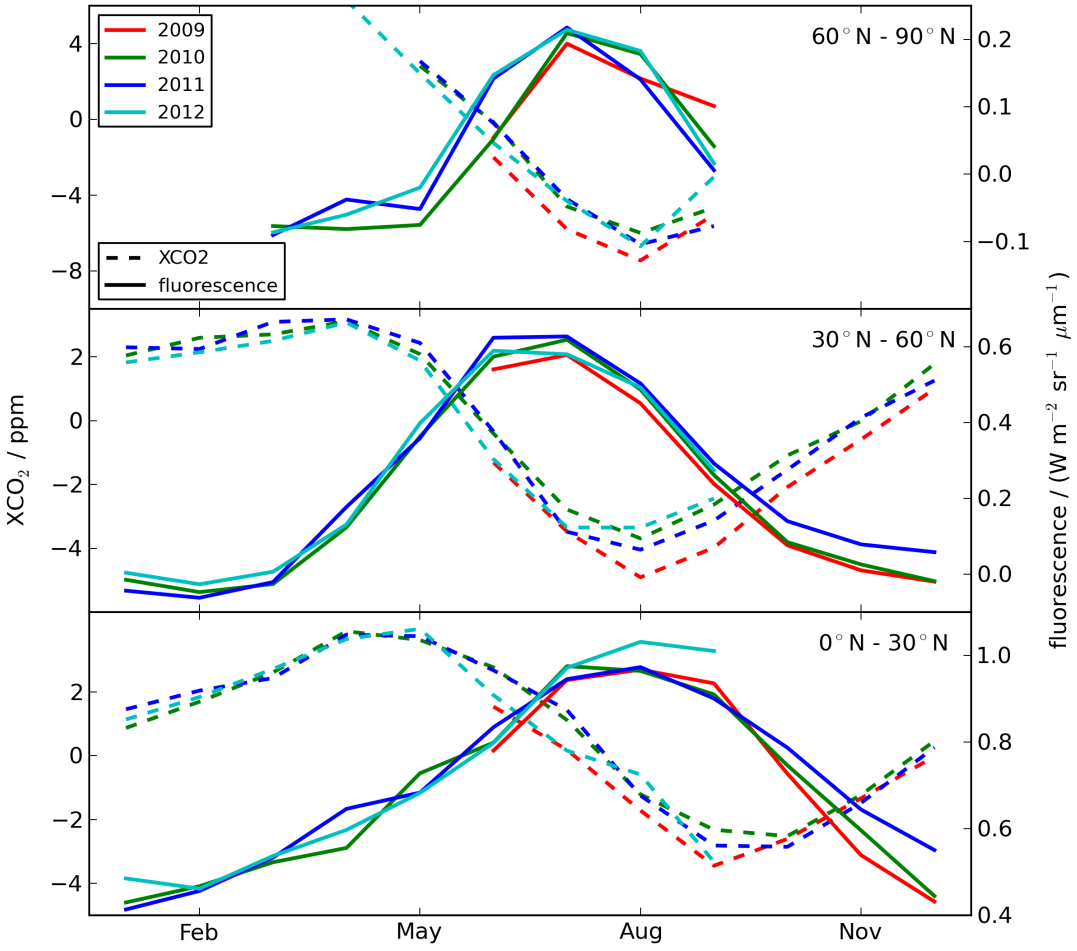

Figure 7.2.: Northern hemisphere 30° latitudinal zonal means of XCO_2 and chlorophyll fluorescence. The annual increase of XCO_2 from the upper panel of figure 7.1 is subtracted. The chlorophyll fluorescence (solid lines) peaks earlier in the year than XCO_2 (dashed lines) reaches its minimum. The time and the strength of chlorophyll fluorescence and XCO_2 cycles, vary with the zones. The colors distinguish the years. The amplitudes of the fluorescence increases from pole to equator and peaks somewhat earlier in the year for higher latitudes. In contrast, the XCO_2 signal has higher seasonal cycle amplitudes in higher northern latitudes.

The middle panel of figure 7.3 compares the XCO_2 records of the Baserun and the Fluorun. Plotted are the differences of the monthly grid cell averages, calculated by subtracting Fluorun values, shown in the top panel, from the corresponding Baserun values, not shown explicitly. Again, the solid line links the monthly means. Taken together, the first three panels from top provide clear evidence of the significant impact of chlorophyll fluorescence on the retrieval of XCO_2. In months where high chlorophyll fluorescence signals appear, the Fluorun retrieves roughly 2 ppm higher XCO_2 than the Baserun. Thus, comparisons of chlorophyll fluorescence and satellite-based XCO_2 retrievals neglecting chlorophyll fluorescence might suffer from severe systematic errors.

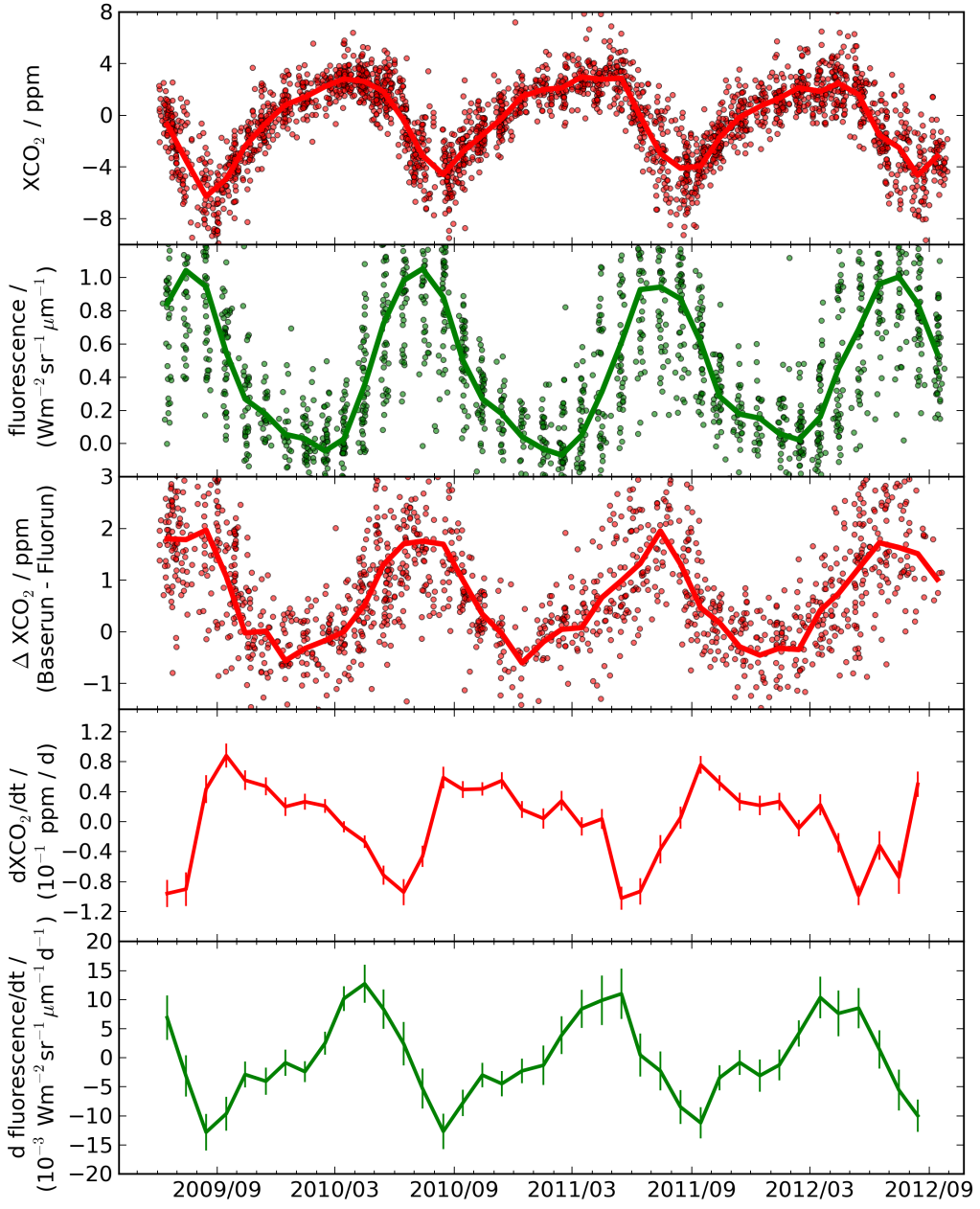

Figure 7.3.: Time series of XCO_2 and fluorescence over eastern North America (100°W-55°W, 30°N-52°N). The upper panel shows the detrended Fluorun XCO_2 time series. Plotted are the monthly averages of each 2° by 2° grid cell within the area. Additionally, the solid line links the monthly averages of the complete area. The second panel from top contains the chlorophyll fluorescence retrieved with the Fraunhofer concept. Same illustration as above but with 4° by 4° grid size. The difference between the Baserun's and the Fluorun's XCO_2 is demonstrated in the middle panel. The two lowest panels comprise the change per day of the Fluorun XCO_2 record and the chlorophyll fluorescence record, respectively.

The lower two panels of figure 7.3 plot the change per day of the XCO_2 and the chlorophyll fluorescence within the regarded region, respectively. The change per day is calculated by the numerical derivatives of the monthly averages. Within the North American region, the highest change rates of XCO_2 level roughly at 0.1 ppm XCO_2 per day. The change rate of the chlorophyll fluorescence signal per day reaches roughly one percent of the signal itself. The two panels clearly reveal that the photosynthesis which is remotely sensed by its fluorescence signal drives the change of XCO_2. The change in chlorophyll fluorescence persistently peaks before the CO_2 uptake peaks.

Having extracted the monthly mean atmospheric carbon concentrations over a region and the monthly mean chlorophyll fluorescence signal of the region, the correlation of the two illustrates the carbon cycle. Figure 7.4 depicts the carbon cycle over North America for almost four years. The solid line links the monthly mean XCO_2 fluorescence pairs chronologically. The pentagon symbols, denoting February, are in the top left corner of the plot, because, in late winter, the chlorophyll fluorescence signal has reached its minimum and, contrary, the atmospheric CO_2 abundance reached its maximum. Till May (square symbols) XCO_2 remains on its high level although the chlorophyll fluorescence increases. Assuming that atmospheric transport phenomena are not important on this scale, this results from a balanced biomass decomposition and photosynthetic carbon fixation. Along with the increasing photosynthetic activity the temperature rises which accelerates the biomass decomposition rate. Between May and August (diamond symbols) the biomass production wins over the decomposition. Thus, the atmospheric carbon abundance drops. Till February the photosynthetic activity declines and the land biosphere respires more CO_2 than it absorbs.

In addition to North America, the time series plot and the carbon cycle plot are both generated for Europe and for the northern and southern tropics. These regions, especially the tropics, reveal differences to the North American carbon cycle. The time series for the northern and southern tropics are shown in figures 7.5 and 7.6, respectively. The corresponding carbon cycle plots are compiled in figure 7.7. The plots for Europe are listed in the Appendix.

The tropical region, comprising all longitudes and ranging from 23.5°S to 23.5°N, are split at the equator. Otherwise, the northern signal variability would damp the southern variability down and vice versa. However, this split disregards any airmass transport across the equator by shifts of the inter tropical convergence zone (ITCZ). In contrast to North America and Europe, the previously described detrending is performed with the background increase inferred in the middle panel of figure 7.1. Unfortunately, the number of spectra during the monsoon time is quite low due to the prevalence of clouds. As a result, a robust analysis of the differences between Baserun and Fluorun over these photosynthetic highly active regions is hampered.

The carbon cycle plots in figure 7.7 reveal a somewhat different shape for the northern tropics compared to North America. Especially, the southern tropics exhibit a differently shaped carbon cycle. In addition, the cycle in the southern tropics varies stronger among the years. Note that the cycle in 2010 is particularly small which is conjointly reflected in the CO_2 surface flux estimates in section 7.2.

In future, these kinds of plots might provide a top down approach to identify biomes or plant's productivity. To do so on a regional scale, in particular, a higher density of accurate XCO_2 and chlorophyll fluorescence measurements is crucial.

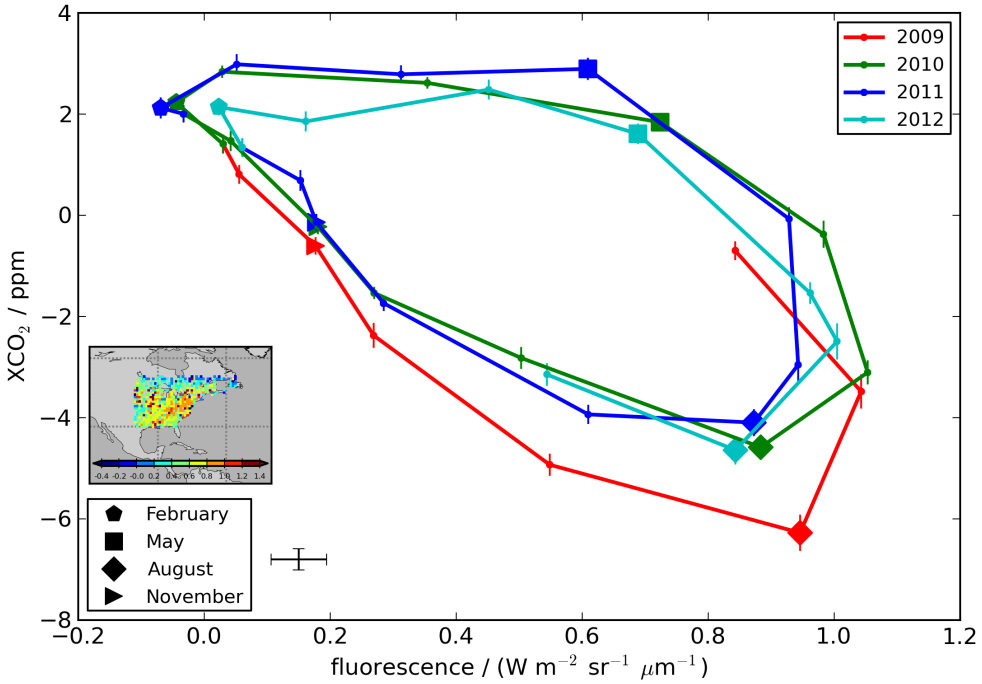

Figure 7.4.: The carbon cycle over North America. The monthly averages of XCO_2 are plotted versus the monthly averaged chlorophyll fluorescence, both are extracted from the top panels of figure 7.3. The solid line links the averages in chronological order. The color denotes the respective year. Four symbols give an orientation on the season. The error of the mean of XCO_2 is attached to each data point. For better visibility, the error of the mean of fluorescence is plotted only on average, see error bars next to the lower right legend. The map inset visualizes the region with 1° by 1° averaged fluorescence signals. Its colorbar ranges from -0.4 to 1.4.

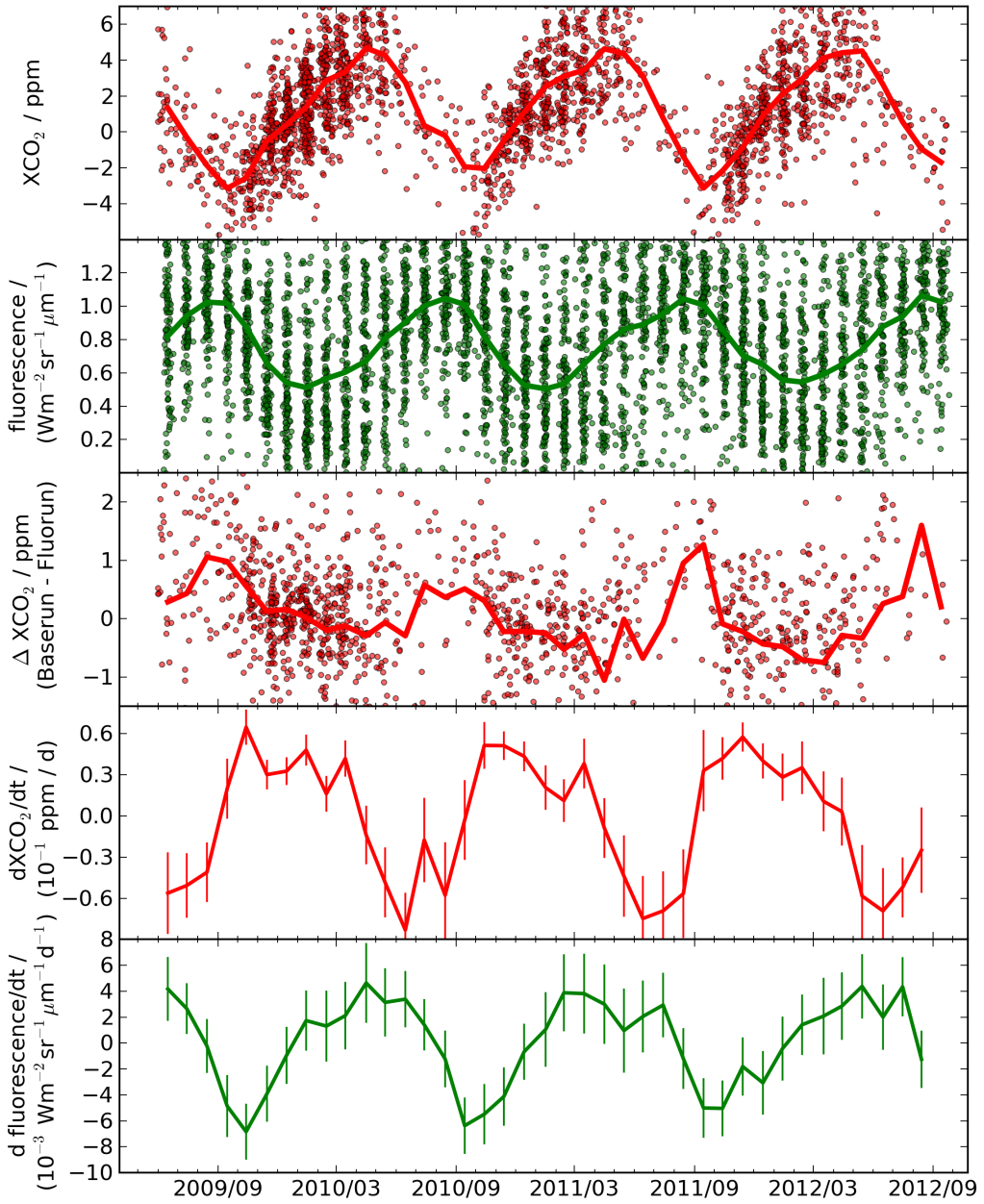

Figure 7.5.: Time series of XCO_2 and fluorescence over the northern tropics (0°N-23°N). Same illustration as in figure 7.3. During the monsoon time only few XCO_2 soundings pass all quality criteria. Unfortunately, this hampers a zoom into smaller regions and, in addition, it results in a weak comparison between the Baserun and the Fluorun in the middle panel.

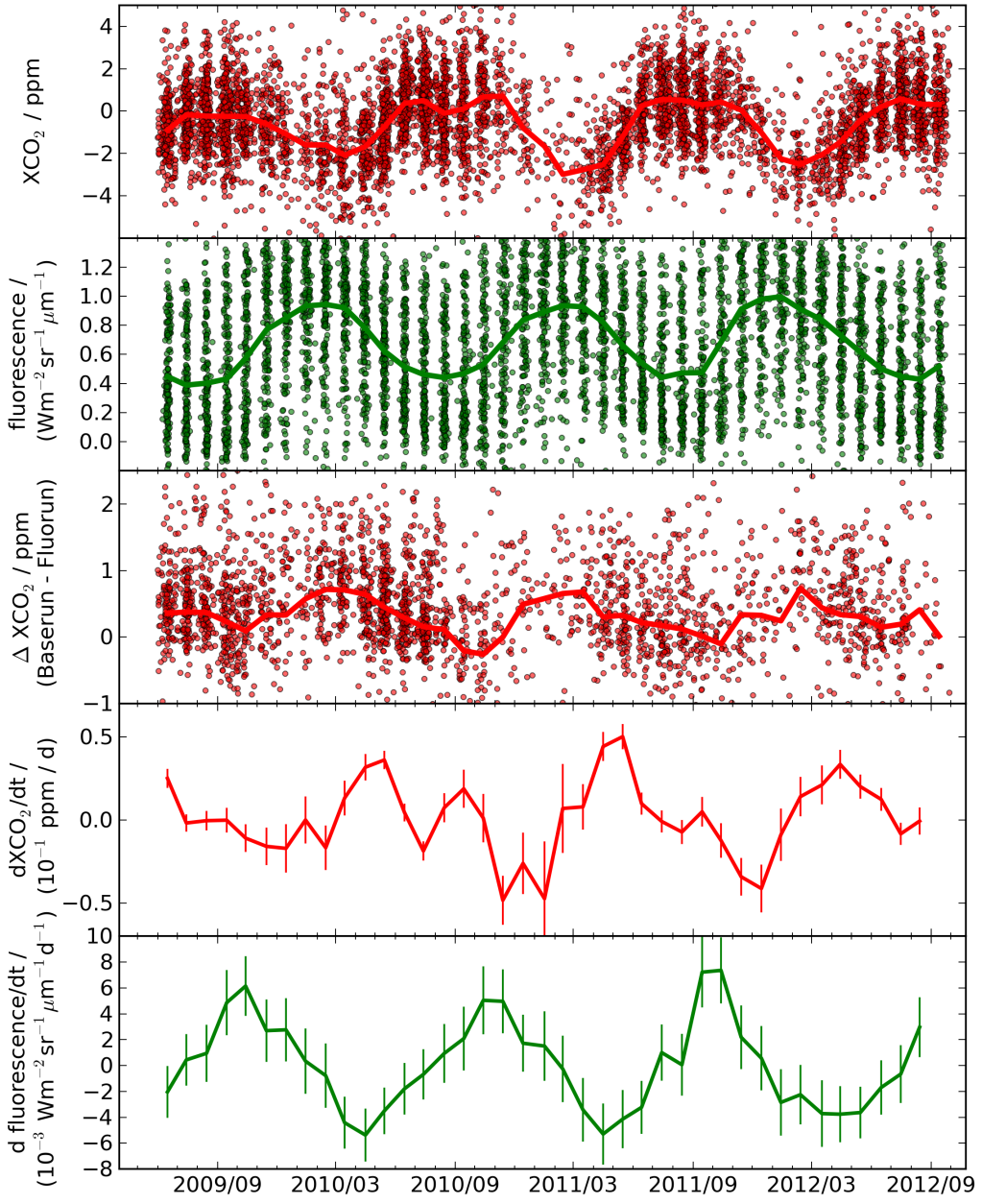

Figure 7.6.: Time series of XCO_2 and fluorescence over the southern tropics (23°S-0°S). Same illustration as in figure 7.3. The southern hemispheric XCO_2 cycle is weaker and phase shifted compared to the northern hemispheric one. Note that the sampling here only regards the latitudes. Consequently, any air-mass transport across the equator, due to changes in the ITCZ, interferes the northern and southern hemispheric XCO_2 cycles.

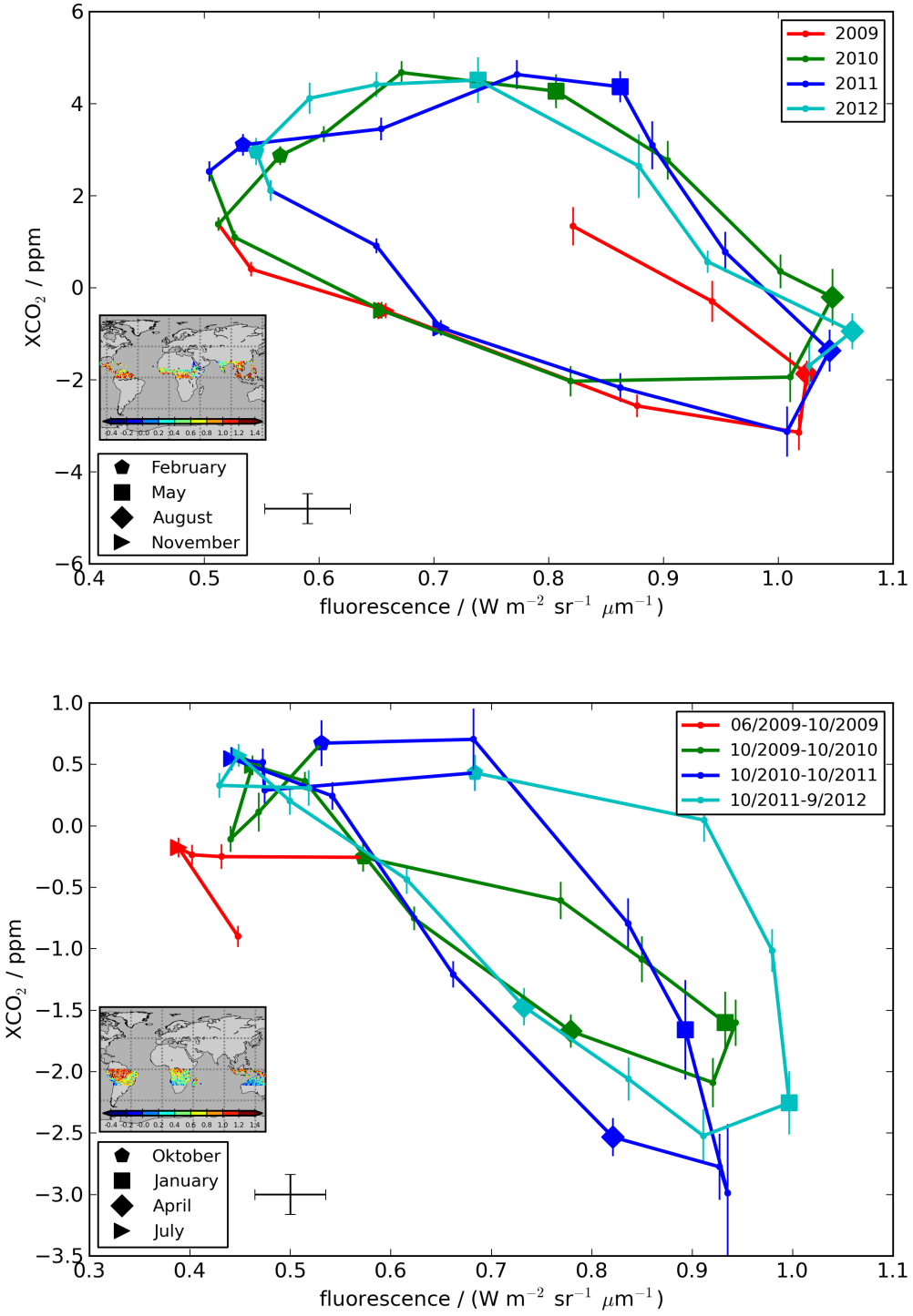

Figure 7.7.: The carbon cycle of the northern and southern tropics in the upper and lower panel, respectively. Same illustration as in figure 7.4. Note that the map inset cuts of some area to keep aspect ratios. Again, any interferences of the two cycles, due to airmass transport, is disregarded. The shape and the inter annual variation of the cycles depend strongly on the investigated region. Concerning the errors of the means, especially, the cycle in the southern tropics would benefit from more information about XCO_2.

7.2. Impact of chlorophyll fluorescence on CO_2 surface flux estimates

The uncertainty of CO_2 surface flux estimates due to sparse CO_2 measurements can be reduced by assimilating GOSAT XCO_2 observations (Basu et al., 2013). However, small regional biases in the GOSAT XCO_2 record can significantly affect CO_2 surface flux estimates. To check the influence of neglecting chlorophyll fluorescence in GOSAT retrievals on CO_2 surface flux estimates, a couple of atmospheric inversions are presented here. The constraints on the CO_2 sources and sinks are given by four different sets of observations where the bias corrected or uncorrected GOSAT XCO_2 record accounts or neglects chlorophyll fluorescence. The atmospheric inversion uses a TM5 4DVAR setup which is described in detail by Meirink et al. (2008). The experiment closely follows the study reported by Basu et al. (2013).

In this atmospheric inversion, CO_2 tracers are transported on meteorological wind fields and, in addition, they are compared to measurements. Subsequently, the surface fluxes are adjusted to improve the match between modeled and measured CO_2 concentrations. In particular, the CO_2 surface fluxes of terrestrial biosphere and oceans are optimized whereas anthropogenic fossil fuel emissions are not optimized. The atmospheric inversion setups used here has some updates compared to the setup in Basu et al. (2013). The most important ones are a finer atmospheric transport model (TM5, Krol et al., 2005) grid resolution of 3° by 2°, updated prior flux estimates and their uncertainties. Additionally, more CO_2 observation sites are included in the optimization. In contrast to the setup by Basu et al. (2013), only high gain land nadir observations from GOSAT are considered here.

Basu et al. (2013) found the GOSAT observations retrieved by RemoTeC able to reasonably constrain the TM5 4DVAR estimated CO_2 surface fluxes in the tropics and in the northern extra-tropics. In the southern extra-tropics a stronger seasonal cycle was obtained with GOSAT data compared to independent measurements. A bias correction of 0.93 ppm XCO_2 between ocean glint and land nadir observations was found to substantially reduce this artifact. In comparison with the in situ data, the GOSAT observations enhanced the net poleward directed carbon flux which was in contrast to earlier findings by Stephens et al. (2007). The most realistic optimized fluxes were obtained in a joint setup where both GOSAT total column measurements and flask measurements constrained the CO_2 concentrations.

Here, the inversions are constrained by GOSAT data only and not jointly constrained by GOSAT and in situ measurements. Thus, the fluxes are not to be considered as quantitatively optimized. The study here focuses on the influence of neglecting or accounting chlorophyll fluorescence in the GOSAT XCO_2 records on the surface flux estimates. The according RemoTeC retrievals are called Baserun and Fluorun. In addition, the bias corrected RemoTeC records are compared to the non bias corrected ones.

Figure 7.8 shows the annual total biogenic and oceanic CO_2 fluxes aggregated within six different spatial regions. The first group of bars shows the global carbon emissions, summing up the ocean surface and the land biosphere fluxes, for different inversions. The next two bar groups reveal the partitioning of the natural carbon sinks between ocean and land biosphere. Finally, three bar groups show the emissions for the northern extra-tropics, the tropics, and the southern extra-tropics, respectively. The upper panel shows the results for the year 2010 and the lower one for the year 2011. Each bar group comprises the prior surface fluxes (grey), the optimized surface flux data that are constrained by a) only surface flask measurements (in situ, yellow), b) bias corrected RemoTeC Baserun re-

trieved GOSAT observations ('RTC no fluo bc', green), c) the non bias corrected RemoTeC Baserun retrieved GOSAT observations ('RTC no fluo', light blue), d) bias corrected RemoTeC Fluorun retrievals that explicitly account chlorophyll fluorescence in the radiative transfer ('RTC fluo bc', blue), and, finally, e) non bias corrected RemoTeC Fluorun retrievals ('RTC fluo', red).

The uncertainty of the globally aggregated CO_2 surface fluxes is highest for the prior flux. As expected, the in situ data constraint reduces the estimated uncertainty. In both years the uncertainty reduction is nearly 30%. The GOSAT data further reduces the uncertainty of the global CO_2 sink estimate in both years by roughly 20%.

For the 'RTC no fluo' and 'RTC no fluo bc' inversion setups, using only the Baserun data, the tropics are a net source of atmospheric carbon which is in contrast to the results of the in situ inversion setup. The RemoTeC bias correction has a minor influence on the Baserun constrained inversions which is in line with the low impact on the TCCON error correlations. accounting for chlorophyll fluorescence in the radiative transfer model results in a significant reduction of the CO_2 emissions in the tropics. Indeed, the inversion estimates a significant CO_2 sink in the tropics in the year 2011 for the non bias corrected Fluorun. Thus, accounting for chlorophyll fluorescence brings GOSAT constrained inversions more in line with the in situ constrained inversion. The enhanced tropical CO_2 sink is, however, masked by the RemoTeC bias correction. Remembering the influence of the XCO_2 apriori profile on the TCCON validation, the RemoTeC bias correction might need to be reconsidered.

The 'RTC fluo' inversion setup, using the bias corrected Fluorun data, estimates, in both considered years, roughly 2 Pg less carbon emissions in the tropics. Using the non bias corrected Fluorun data, the CO_2 sink is enhanced by roughly 2.5 Pg in the year 2010 and almost 3 Pg in the year 2011. This enhancement of the carbon sink in the tropics is on the order of 50% and 30% of the global carbon sink in the years 2010 and 2011, respectively. The tropics are only weakly constrained by in situ mesurements and comprise the highest chlorophyll fluorescence signals. In future, satellite observations need to take chlorophyll fluorescence into account to provide better constraints on the carbon flux estimates.

Another effect of accounting for chlorophyll fluorescence is that the ocean land partitioning of the global CO_2 surface fluxes is more realistic because the carbon uptake by the land biosphere is enhanced. This effect is consistent in both years. However, it is stronger for the bias corrected Fluorun and only significant in the year 2011. The ocean land bias correction, applied by Basu et al. (2013) to RemoTeC GOSAT retrievals that neglected chlorophyll fluorescence, qualitatively exhibits the same behavior. Thus, this ocean land bias correction might to some extend compensate erroneous biases that are caused by neglecting chlorophyll fluorescence in the XCO_2 retrieval.

7.3. The carbon cycle constrained by GOSAT's observations

The natural carbon cycle considered here is constituted by the atmospheric carbon source of biomass decomposition and wild fires and, opposingly, the atmospheric carbon sink of photosynthesis. Both the source and the sink sum up to the net biogenic carbon surface flux. Hitherto, this chapter discussed the regional change per day in atmospheric CO_2 concentrations related to chlorophyll fluorescence signals. The CO_2 concentrations were detrended to exclude the anthropogenic carbon source or any long term changes. Further, the previous subsection presented net biogenic carbon surface flux estimates by several

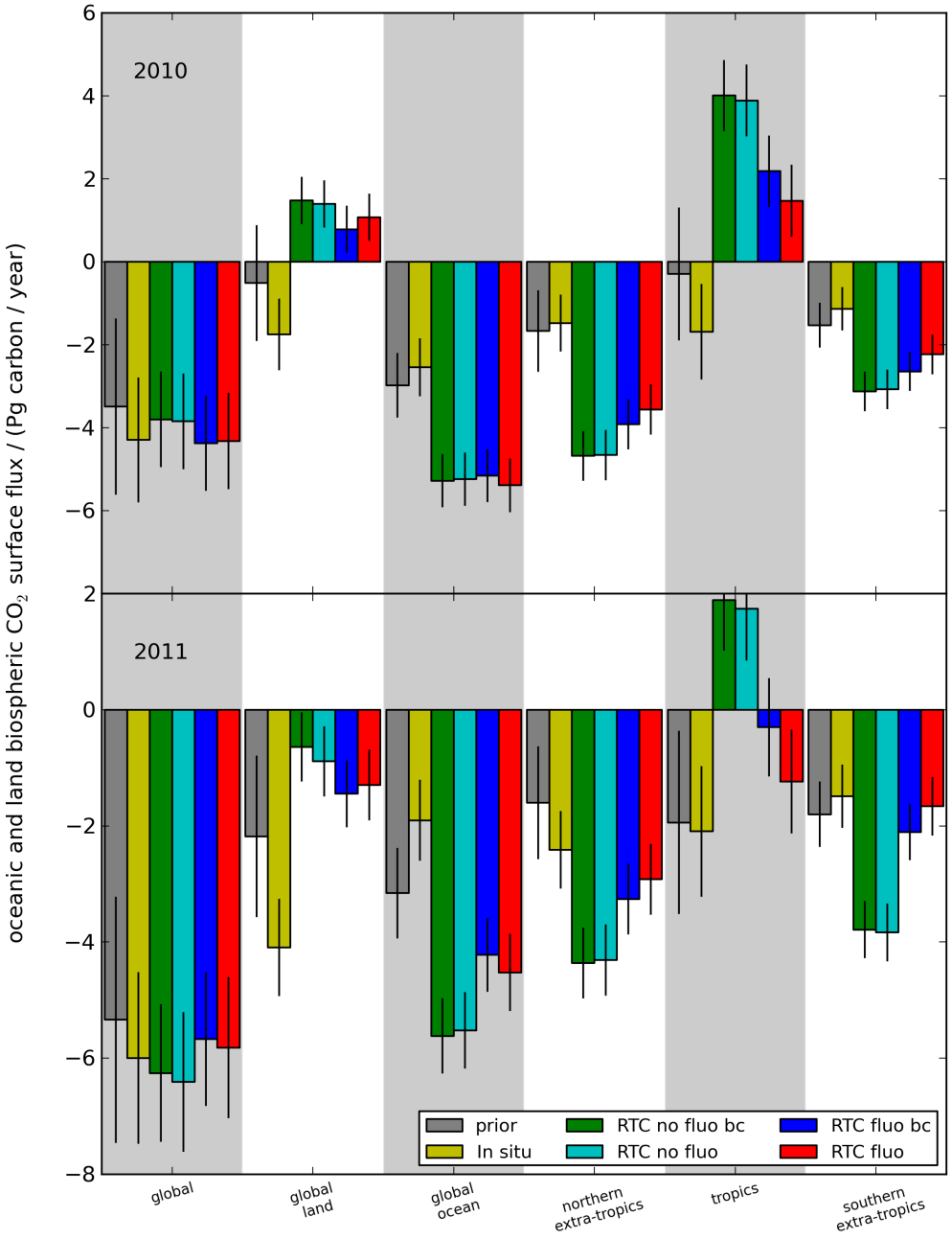

Figure 7.8.: CO_2 surface fluxes. Shown are the total annual CO_2 oceanic and biospheric land surface fluxes for the year 2010 and 2011 in the upper and lower panel, respectively. The fluxes are aggregated globally, for all land and all ocean surfaces, for the northern and southern extra-tropics, and for the tropics (23.5°S to 23.5°N). The prior surface fluxes are illustrated in grey, the five optimized surface flux data sets are constrained by different measurements. These are surface flask measurements only (In situ, yellow), RemoTeC Baserun (green), RemoTeC Baserun without bias correction (light blue), RemoTeC Fluorun that explicitly account for fluorescence in the radiative transfer (blue), and RemoTeC Fluorun without bias correction (red). Considering chlorophyll fluorescence in the RemoTeC retrievals significantly changes the fluxes in the tropics. An effect that is masked to some extend by the RemoTeC bias correction. The flux partitioning between ocean and land are not realistic, see text for explanation.

atmospheric inversions constrained by different measurement data sets. This section here, discusses how to identify and constrain regional carbon fluxes directly with GOSAT's observations.

The chlorophyll fluorescence is directly linked to the biogenic sink of atmospheric carbon. This was discussed in chapter 5 where the chlorophyll fluorescence was found to be highly correlated with the gross primary production (GPP) data modeled from the MPI-BGC Jena (Jung et al., 2011). The GPP of a region can be calculated using the correlation shown in figure 5.9. The chlorophyll fluorescence is retrieved on a monthly 4° by 4° grid. However, not every grid cell in the regarded region is covered by the chlorophyll fluorescence record in each month. To calculate the regional GPP, GOSAT's chlorophyll fluorescence record is assumed to be representative for the complete region and is averaged over the complete land surface of these regions. This assumption introduces low uncertainties if the regarded region exhibits a quite homogeneous photosynthetic activity. Given the measurement density and accuracy, the calibration of regional GPP per month with GOSAT observations is rather qualitative. Future satellite missions might provide a chlorophyll fluorescence record that enables a quantitative calculation of net fluxes for North America, Europe and other regions.

The change in XCO_2 within a certain region is correlated to the net carbon surface flux in that region. Of course, this correlation could be disturbed by any airmass transport in and out of the region. The previous subsection presented sophisticated carbon surface flux estimates that can be used to calibrate the change in XCO_2 with the net carbon surface flux. The correlation of the change in XCO_2 over North America with the estimated net biogenic fluxes is shown in figure 7.9. The estimates of the net biogenic fluxes are jointly constrained by in situ data and the full physics RemoTeC data accounting for chlorophyll fluorescence in the retrieval. The fluxes are aggregated over the Transcom[2] region North America. This Transcom region is larger than the North American region in which the change in XCO_2 is observed. The difference between these two areas introduces a systematic error in the flux calibration. Despite this error and the neglected airmass transport, the correlation found in figure 7.9 is very high with a Pearson correlation coefficient of $R^2 = 0.87$. In addition to the discussed error sources, the TM5 4DVAR surface flux estimates themselves are not fully optimized as discussed in the previous section. For instance, GOSAT's ocean glint data are neglected in the inverse model runs. Thus, the calibration of biogenic carbon surface fluxes with changes of XCO_2 should be considered to be qualitative.

Having discussed the schematic calculation of the biogenic carbon fluxes from GOSAT observations, figure 7.10 presents the multi year averaged carbon flux cycle of North America and Europe. The inner axes show the GOSAT retrievals. The outer axes show the schematically calibrated carbon fluxes. During spring and summer, photosynthesis extracts more carbon from the atmosphere than biomass decomposition releases into the atmosphere. This results in a net carbon sink illustrated in blue. From late summer onwards, the photosynthesis fades and the biomass decomposition turns the area into a carbon source illustrated in red. Both photosynthesis and respiration result in large carbon fluxes compared to the net yearly carbon surface flux. The carbon flux cycle disregarding chlorophyll fluorescence in the RemoTeC retrieval is shown in figure 7.10 in dashed green. Comparing the two cycles reveals that neglecting chlorophyll fluorescence in the XCO_2 retrieval leads to a significant underestimation of both fluxes.

[2] url: http://transcom.project.asu.edu/transcom03_protocol_basisMap.php on 2015/08/17

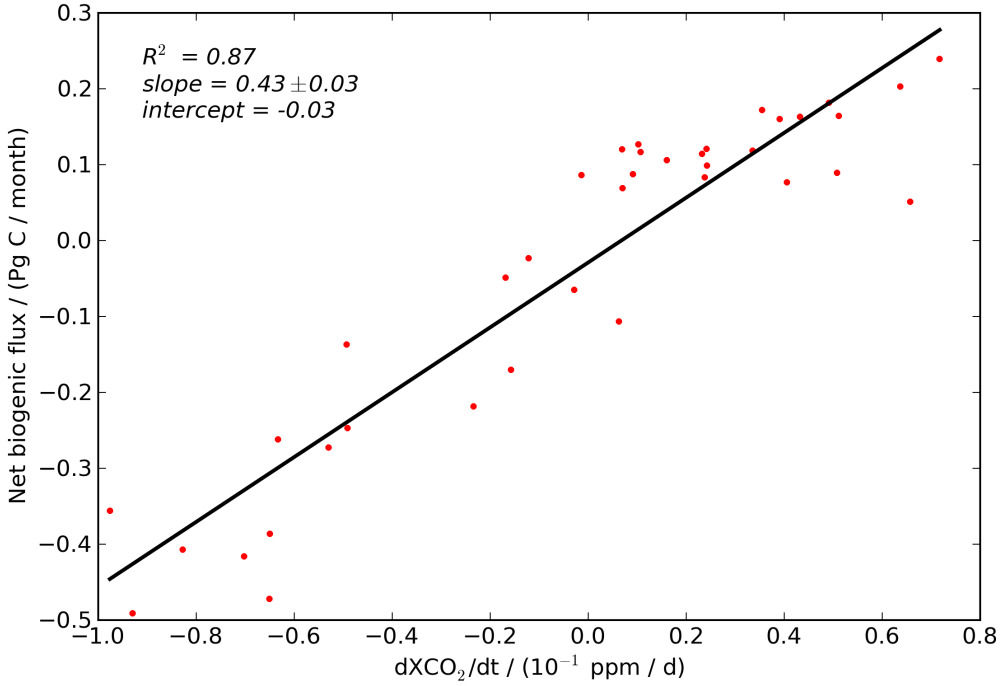

Figure 7.9.: Surface fluxes correlates with change in XCO_2. This figure shows monthly carbon surface flux estimates correlated with change in XCO_2 per day observed over North America by GOSAT. The carbon surface fluxes are estimated using the joint inversion setup accounting for chlorophyll fluorescence and are aggregated per month over the Transcom North America region. The change in XCO_2 per day is calculated from the difference of monthly XCO_2 averages of North America.

This chapter determined the annual XCO_2 background increase measured by GOSAT and found it to be consistent with independent measurements from the Mauna Loa NOAA-ESRL station. Having subtracted the long term XCO_2 increase, the seasonality of the atmospheric CO_2 concentration and its biogenic sink was discussed and illustrated for different regions. Estimates of carbon surface fluxes constrained by different RemoTeC data sets which account or neglect chlorophyll fluorescence in the XCO_2 retrieval were presented. Accounting for chlorophyll fluorescence has a significant impact on surface flux estimates, especially in the tropics. The surface flux estimates constrained with GOSAT data are more in line with in situ measurement constrained surface fluxes when the GOSAT data retrieval accounts for chlorophyll fluorescence in the XCO_2 retrieval. Finally, the GOSAT data were used to qulitatively calculate the natural carbon flux cycle over North America and Europe. It was shown that the biogenic carbon surface fluxes are strongly underestimated in regions exhibiting high photosynthetic activity if chlorophyll fluorescence is neglected in the retrieval.

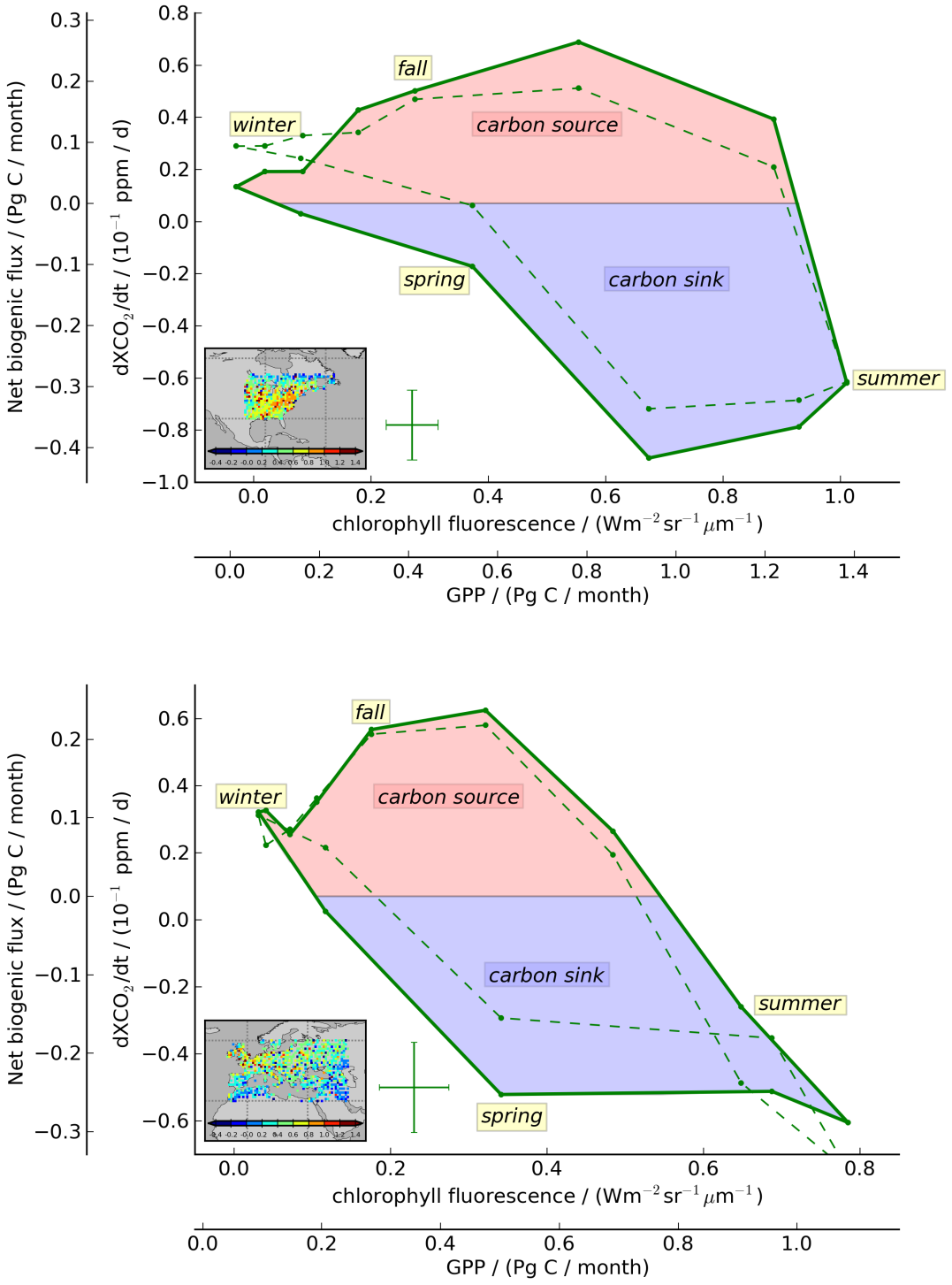

Figure 7.10.: The schematic carbon cycle of North America and Europe in the upper and lower panel, respectively. The multi year monthly averages of change in XCO_2 and chlorophyll fluorescence form the carbon cycle (solid green). The correlations from figures 5.9 and 7.9 map the chlorophyll fluorescence and the change in XCO_2 to GPP and the net biogenic carbon surface flux, respectively. The ratio of GPP to respiration divides the enclosed area into a net carbon source during fall and winter and a net carbon sink during spring and summer. The summer season, for instance, comprises the months June, July, and August and is denoted next to July's average. The dashed green carbon cycle is calculated with the Baserun's XCO_2 record. The map insets show the chlorophyll fluorescence soundings of the respective regions on a 1° by 1° grid. Next to the map insets the mean errorbars are plotted.

8. Conclusion and outlook

The greenhouse gases CO_2 and CH_4 are the key drivers of the anthropogenic climate change. However, the natural stocks and fluxes of these gases are huge compared to the anthropogenic influences. Nonetheless, a change in the climatic and geophysical conditions can result in a feedback of the natural carbon fluxes. This feedback might release CO_2 into the atmosphere due to more efficient biomass decomposition or, contradictory, it might extract CO_2 from the atmosphere by larger gross primary production (GPP) of biomass. The feedbacks will be different for permafrost areas or tropical wetlands. Thus, observing these natural carbon fluxes accurately on a regional scale is crucial to understand the feedback mechanisms.

The Greenhouse Gases Observing Satellite (GOSAT) is the first satellite that provides the opportunity to remotely sense CO_2 and CH_4 with an accuracy that allows for regionally constrained carbon surface flux estimates.

The RemoTeC algorithm retrieves the total column dry air mixing ratios of CO_2 and CH_4 (XCO_2 and XCH_4) from GOSAT's spectroscopic measurements. This thesis gives an overview on RemoTeC's scientific applications and introduces the setups used or developed in the scope of this work. Further, this thesis discusses in detail the two core modules of RemoTeC: the radiative transfer model and the inversion scheme. This work updates the inversion scheme using a stronger CO_2 profile regularization to improve the retrieval performance. This improved inversion setup is reported in Guerlet et al. (2013b).

This work evaluates the accuracy and precision of RemoTeC's XCO_2 and XCH_4 records in comparison to the ground-based Total Carbon Column Observing Network (TCCON). Within the regarded 40 months time period RemoTeC successfully processes roughly 12,600 TCCON coincident spectra and retrieves XCO_2 with a regional bias of 0.4 ppm and a single measurement precision of 2.0 ppm. RemoTeC retrieves XCH_4 with a regional bias of 2.5 ppb and a single measurement precision of 14.4 ppb. Generally, the differences with respect to TCCON correlate low with all investigated geophysical parameters. The O_2 A-band introduces multiple problems into the full physics retrieval. Thus, this thesis discusses whether the RemoTeC retrieval could exclude the O_2 A-band, following a suggestion by Butz et al. (2009). Unfortunately, the performance of all tested setups skipping the O_2 A-band suffers from insufficient information about atmospheric aerosol scattering.

The direct link between the chlorophyll fluorescence and the plant's photosynthetic activity

is discussed. Remote sensing of chlorophyll fluorescence provides estimates of photosynthetic GPP. Viciously, this chlorophyll fluorescence is an error source for remote sensed XCO_2 and XCH_4 records if it is neglected in the radiative transfer. Previous studies already retrieved chlorophyll fluorescence and correlated it to GPP. However, none of these studies included a physics based radiative transport model of the chlorophyll fluorescence emitted at the Earth's surface. This thesis discusses modifications of RemoTeC's radiative transfer model. These updates are reported in Schepers et al. (2014). Further, this thesis presents a necessary radiance offset correction procedure for high gain GOSAT spectra. Now, RemoTeC is able to consider the lightpath of the surface emitted chlorophyll fluorescence radiance in a multiple scattering atmosphere. The physics based RemoTeC chlorophyll fluorescence retrieval uses Fraunhofer lines in the vicinity of the O_2 A-band. The chlorophyll fluorescence retrieved with this so called Fraunhofer setup is highly correlated with GPP and is well in line with other published data. Thus, the results presented here support and validate the published ones.

Further, this work presents the updates of the full physics setup to account for chlorophyll fluorescence. These updates comprise the chlorophyll fluorescence retrieval, a dedicated radiance offset correction, and a residuum retrieval. The chlorophyll fluorescence retrieved in the full physics setup using the complete O_2 A-band suffers from high correlation of the chlorophyll fluorescence with aerosol parameters. The chlorophyll fluorescence record is too negative, sparse, and too noisy compared to the chlorophyll fluorescence record retrieved with the Fraunhofer retrieval. However, the comparison of the two full physics RemoTeC setups showed that accounting for chlorophyll fluorescence tentatively improves the retrieval. This work finds the sparse global coverage of TCCON measurements to limit the significance of the validation. In particular, this applies to regions exhibiting high photosynthetic activity. In addition, this thesis discusses that the apriori target gas profiles should be considered in the validation procedure.

The annual XCO_2 background increase measured by GOSAT is found to be consistent with independent measurements. This thesis illustrates the seasonality of the atmospheric CO_2 concentration and its biogenic sink for different regions. Further, this work presents estimates of carbon surface fluxes constrained by different RemoTeC data sets accounting for chlorophyll fluorescence or neglecting it. Especially in the tropics, a significant impact on surface flux estimates by accounting for chlorophyll fluorescence is reported. The surface flux estimates constrained with GOSAT data are more in line with in situ measurement constrained surface fluxes when chlorophyll fluorescence is accounted in the XCO_2 retrieval. Finally, the GOSAT data were used to calculate the natural carbon flux cycle, for instance, over North America, see figure 8.1. The inner axes show observed monthly changes of XCO_2 and the recorded chlorophyll fluorescence. The outer axes illustrate the corresponding fluxes schematically. The solid and dashed circle represent the carbon cycle derived with XCO_2 retrievals accounting for or neglecting chlorophyll fluorescence, respectively. Comparing them it is obvious that the carbon fluxes have been strongly underestimated in regions comprising high photosynthetic activity.

Taken together, the observations from GOSAT provide constraints on carbon surface flux estimates. Given the measurement density and quality, the constraints on regional carbon fluxes are rather qualitative. However, interannual comparisons of GOSAT observations might reveal flux variations that can be tracked down to geophysical processes. The RemoTeC algorithm is a powerful and flexible tool to retrieve greenhouse gas concentrations from spectroscopic measurements. RemoTeC will be applied to future instruments retrieving chlorophyll fluorescence and greenhouse gas concentrations by accounting for the multiple scattering atmosphere and, from now on, accounting for an additional subtle physical processes: the photosynthetic lightsource at the Earth's surface.

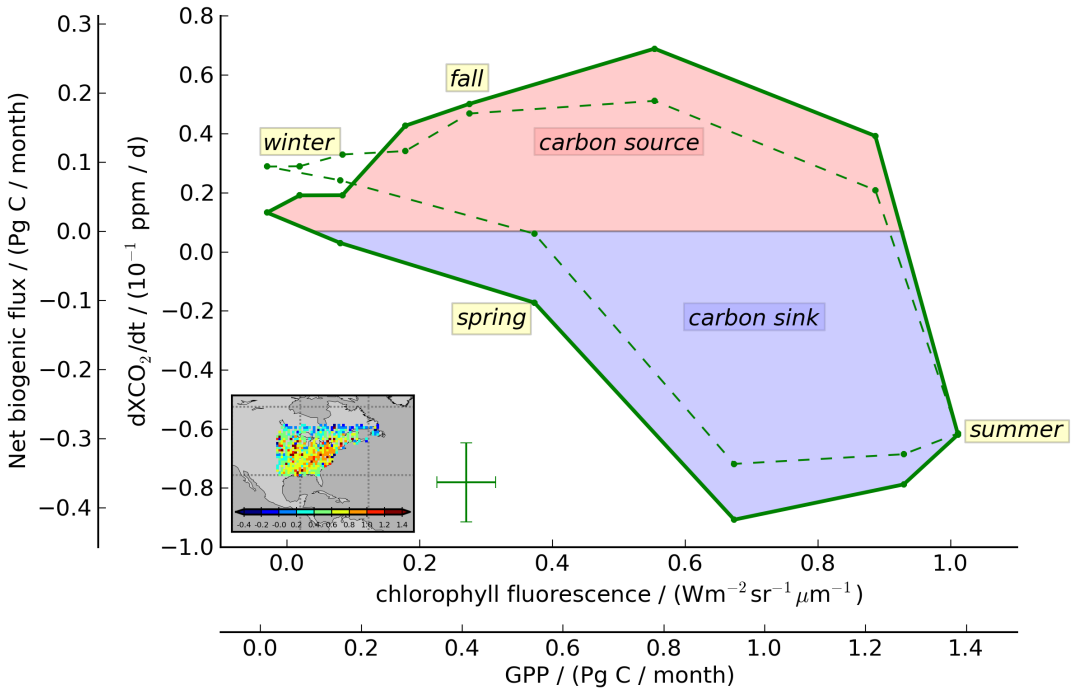

Figure 8.1.: The schematic carbon cycle of North America. The multi year monthly averages of change in XCO_2 and chlorophyll fluorescence form the carbon cycle (solid green). Section 7.3 discusses how to map the chlorophyll fluorescence and the change in XCO_2 qualitatively to GPP and net biogenic carbon surface flux, respectively. The dashed carbon cycle is calculated with the former XCO_2 record neglecting the spectroscopic effect of chlorophyll fluorescence in the O_2 A-band. The map inset shows the chlorophyll fluorescence soundings of the regarded region on a 1° by 1° grid. Next to the map inset the mean errorbar is plotted.

A. Additional figures

Figure A.1 shows the correction of the radiance offset dependence on on the mean signal level for three retrievals. The illustration is the same as in figure 5.4 where the correction is shown for the retrieval window around 755 nm wavelength measured in S-polarization. Here, the correction are shown for P-polarized radiance in the retrieval window around 755 nm wavelength, and the retrievals in the window around 772nm wavelength for S- and P-polarized measurements, respectively.

The correlation of single measurement errors, with respect to TCCON, with different parameters subject to bias corrections, see section 6.5. The correlation coefficients and linear regressions for the bias corrected data sets were given in the respective figures. However, the two dimensional histogram, for instance, of figure 6.12 showed only the uncorrected data. Here, the bias corrected data sets are plotted for both the Baserun and the Fluorun and for both target gases in figures A.2, A.3, A.4, and A.5, respectively.

In section 6.6 the temporal differences of the RemoTeC and the TCCON aprioris at the Lamont TCCON site for the Fluorun were analyzed in figures 6.17 and 6.18. For the Baserun the same illustration is shown in figures A.6 and A.7 for both XCO_2 and XCH_4, respectively.

In Section 7.1.1 the annual background increase of XCO_2 is calculated for the Fluorun GOSAT measurements. The same calculation is performed for the Baserun, see figure A.8. In the time series plots for XCO_2 and fluorescence, the middle panel compares XCO_2 records of the Baserun and the Fluorun, see, for instance, figure A.9. Both records are detrended individually. This means the Baserun's background increase from figure A.8 is subtracted from the Baserun XCO_2 record and the Fluorun is detrended according to figure 7.1.

According to section 7.1.2, figures A.9 and A.10 demonstrate the carbon cycle analyzes for Europe.

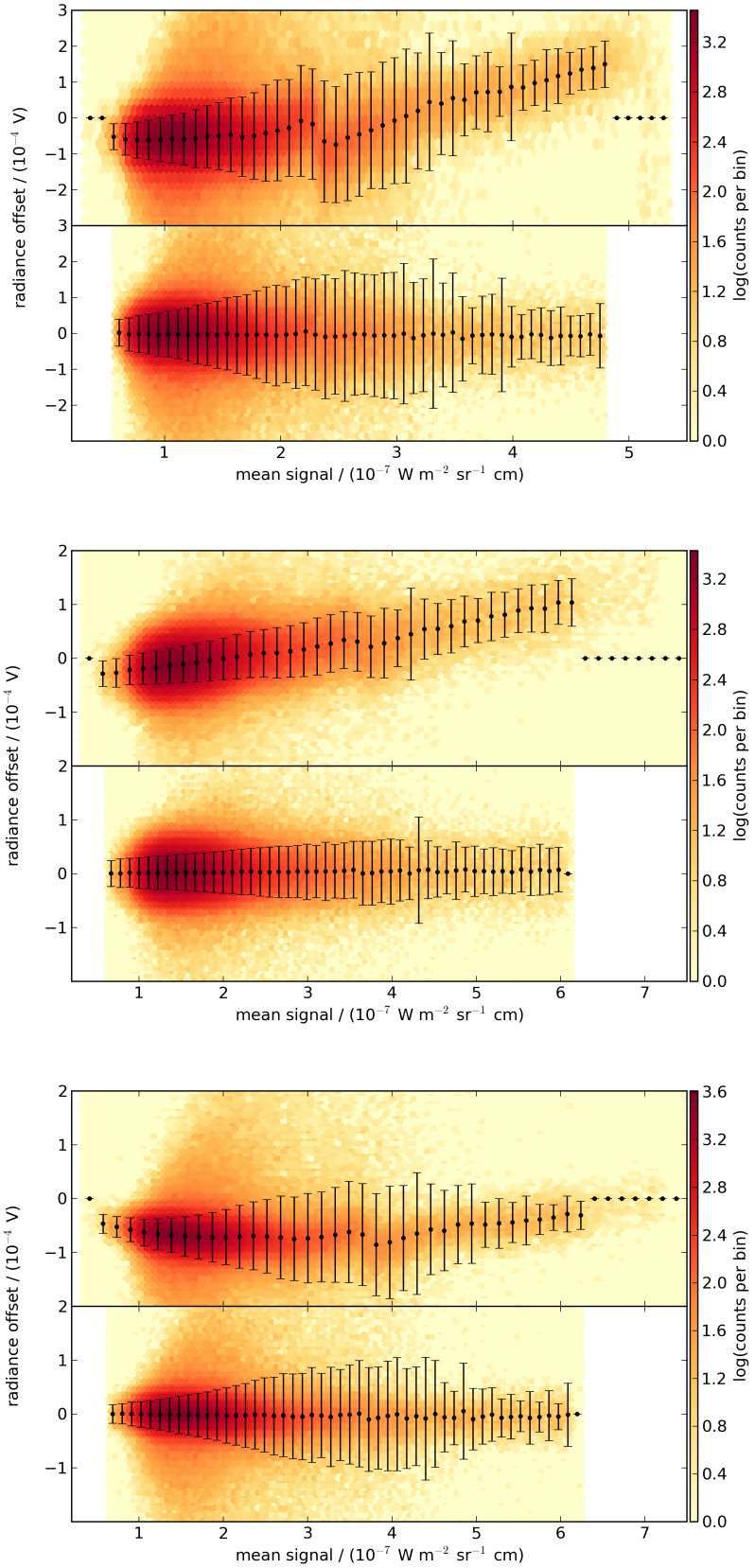

Figure A.1.: Correction procedure for the radiance offset dependence on mean signal. The Thesis shows the result for the retrieval window around 755 nm wavelength measured in s-polarization, see 5.4. Here the results for s polarization in the retrieval window around 772 nm (top) and for p polarization in both retrieval windows (middle: window around 755 nm wavelength, bottom: window around 772 nm wavelength).

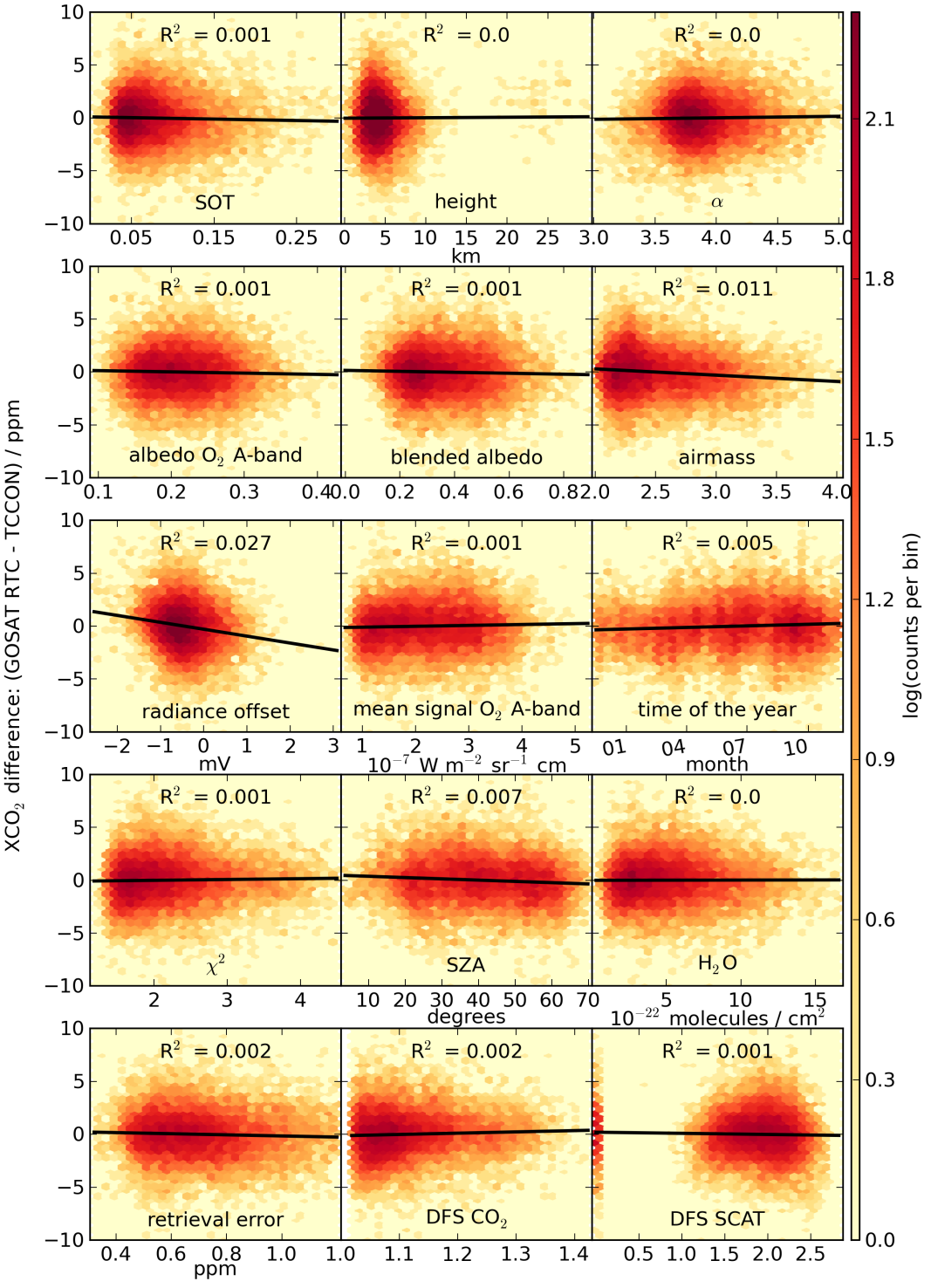

Figure A.2.: XCO_2 error correlations of the Baserun after applying the bias correction. The corresponding figure 4.3 shows the TCCON coincident data set as heat map for the Baserun without bias correction. Overplotted are the heat maps with linear regression lines and the corresponding Pearson correlation coefficients. Here, the heat map itself contains the bias corrected data. The bias correction is given in equation 4.1.

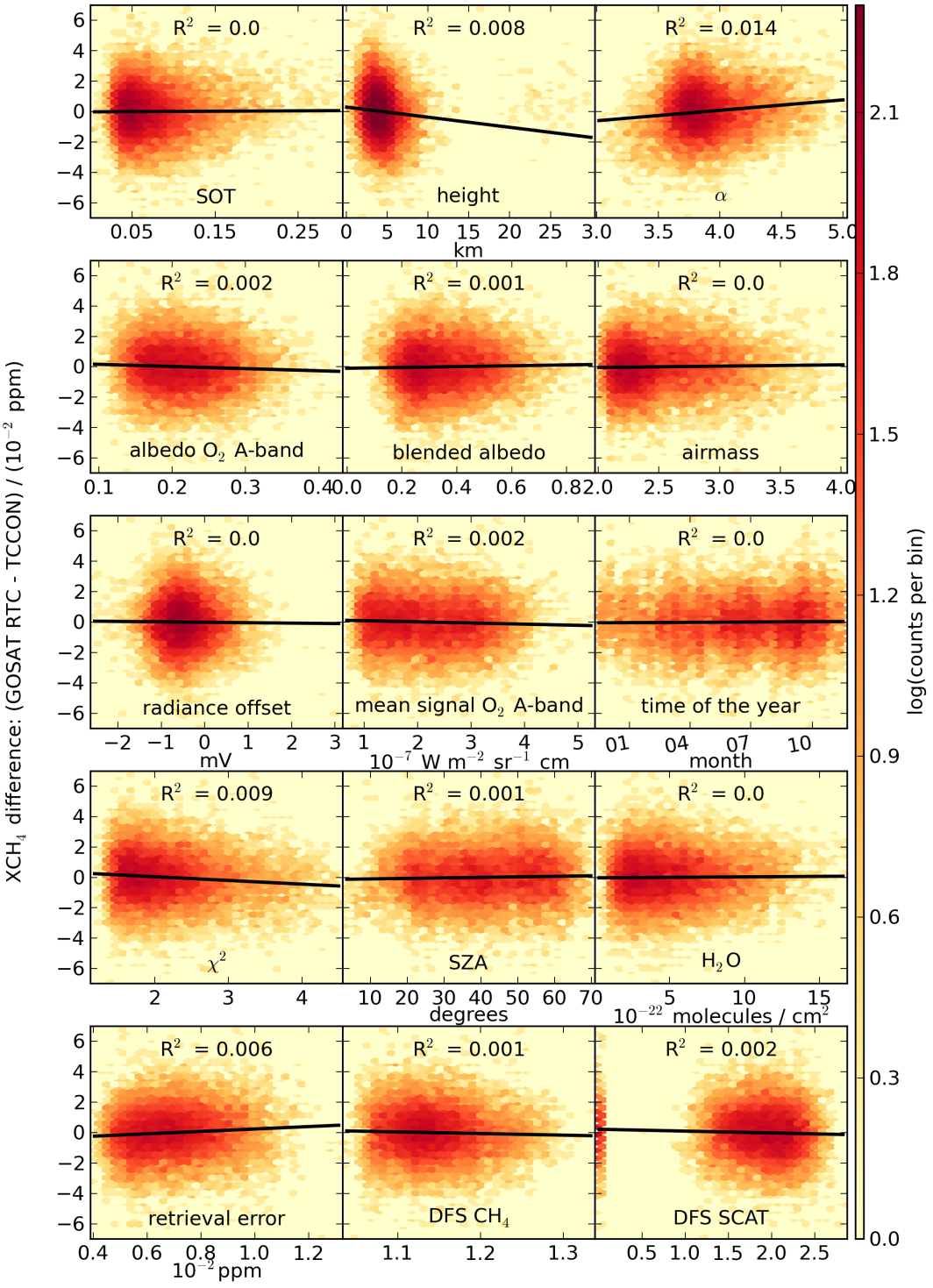

Figure A.3.: XCH_4 error correlations of the Baserun after applying the bias correction. Same as figure 4.4 but including the bias correction from equation 4.2.

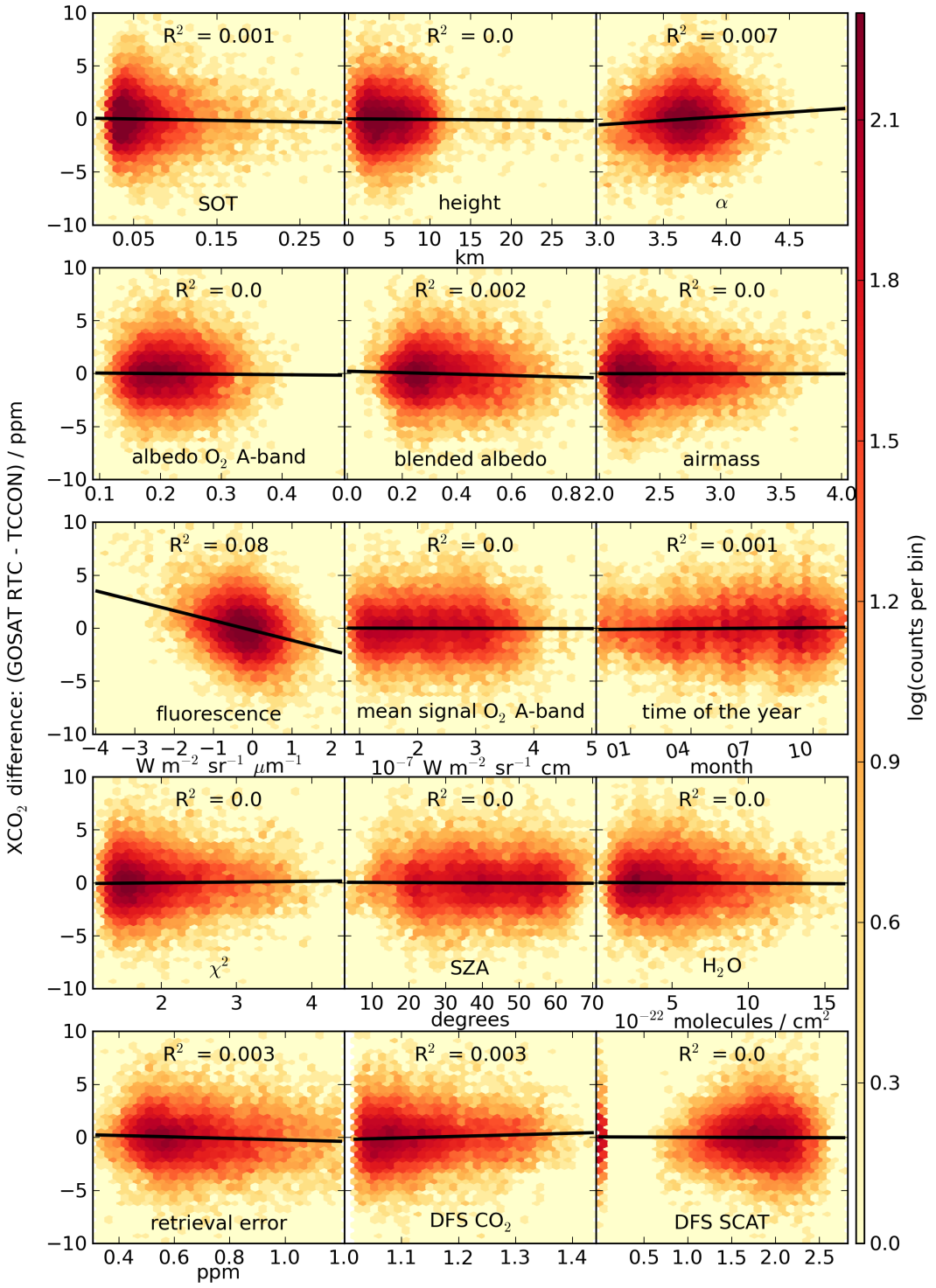

Figure A.4.: XCO_2 error correlations for the Fluorun after applying the bias correction. Same as in figure 6.12 but with bias correction from equation 6.1. The bias correction based on the parameters SOT, albedo, and the aerosol layer height substantial reduce or remove the error correlation for all regarded parameters which is not the case for the Baserun bias corrected data set.

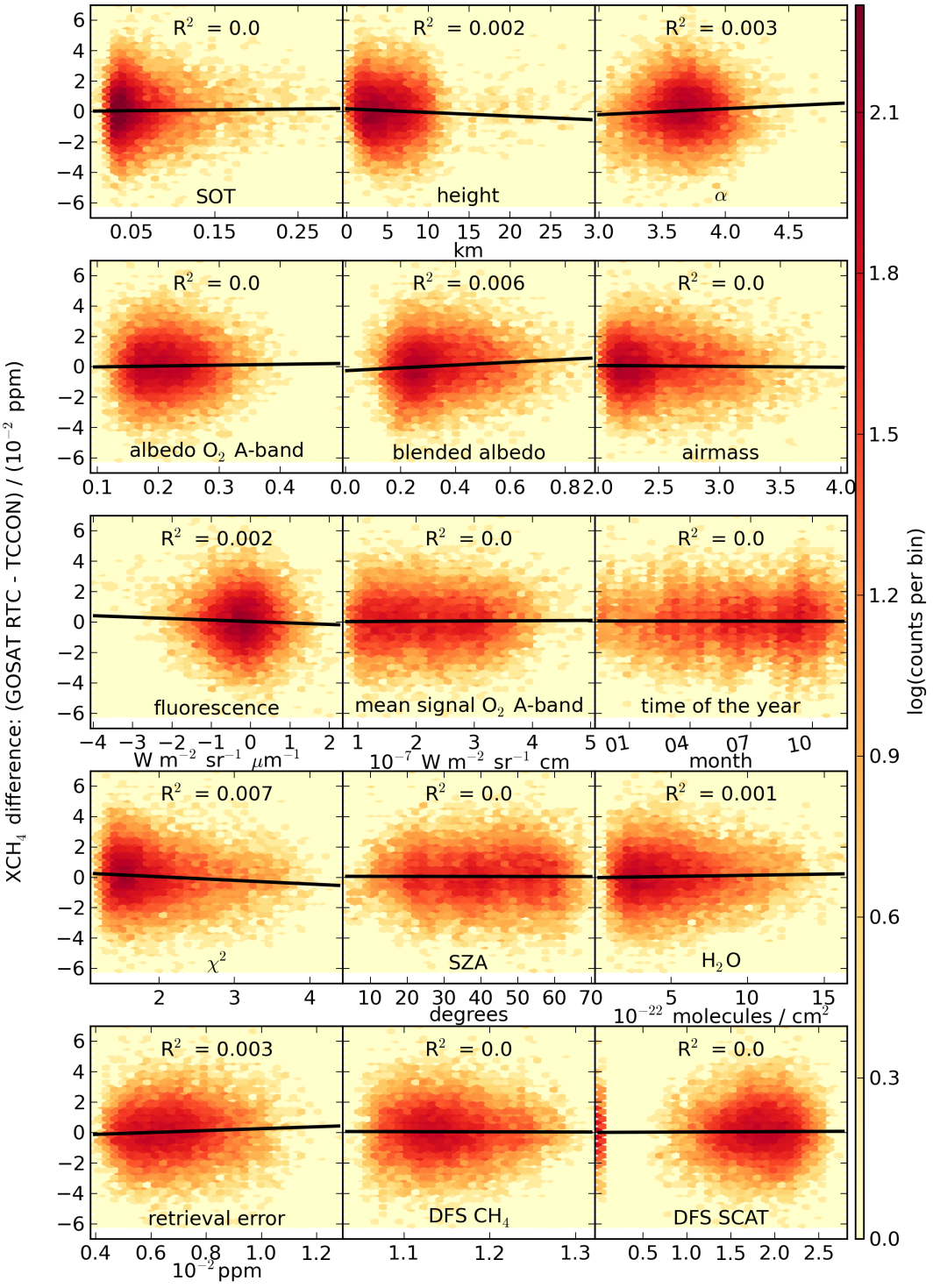

Figure A.5.: XCH_4 error correlations after applying the bias correction. Same as in figure 6.13 but with bias correction from equation 6.2. The bias correction based on the parameters SOT and α substantial reduce or remove the error correlation for all regarded parameters except the for the blended albedo.

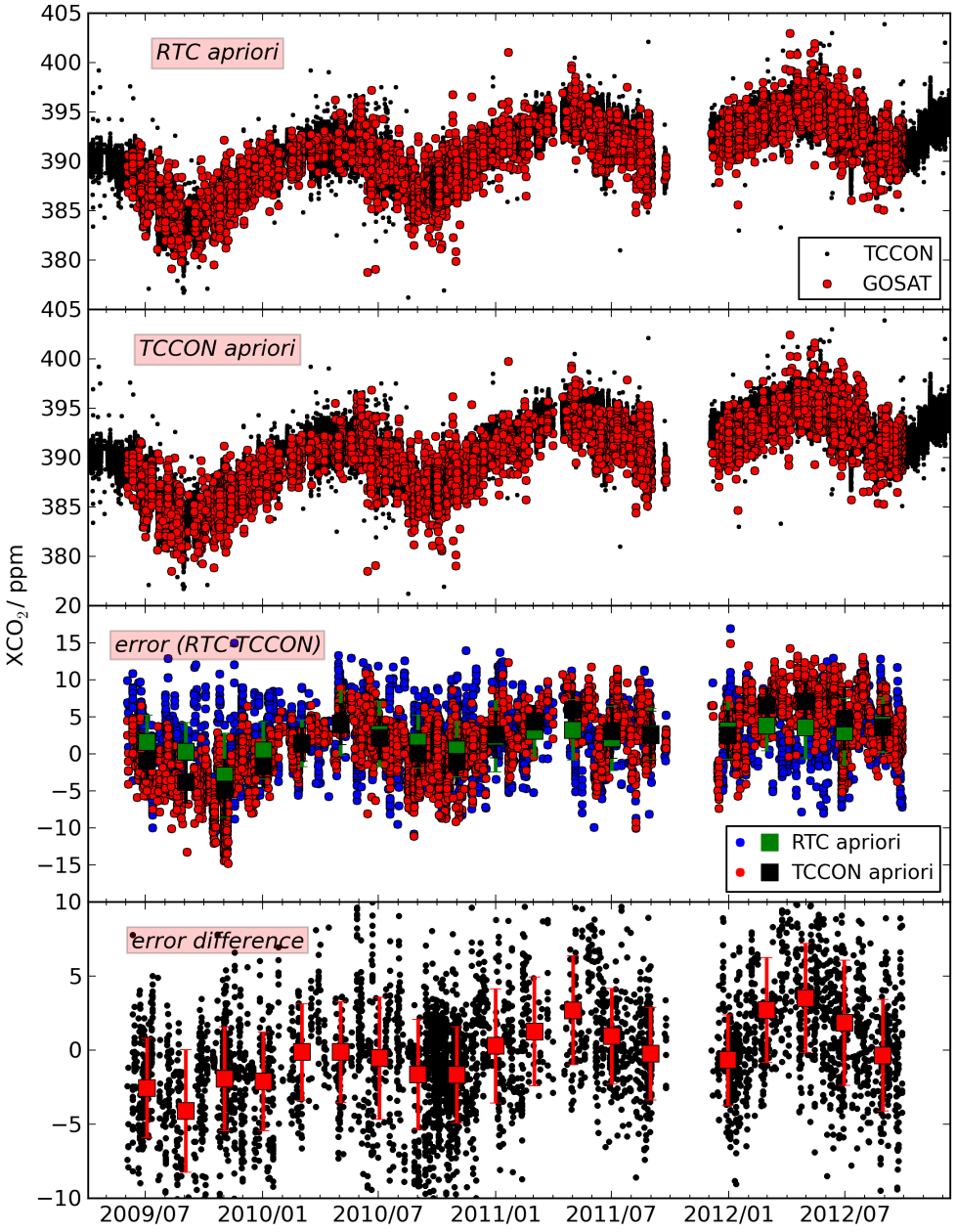

Figure A.6.: Analyzing the different seasonality of the apriori CO_2 profiles for the Baserun. The upper two panels show the time series of the collocated GOSAT TCCON pairs, with both the RemoTeC apriori and the TCCON apriori, respectively. The third panel from top contains the single measurement errors of both data sets along with running mean values for every two months. The standard error is attached to every running mean. The subsequent panel plots in black the differences between the errors, shown in blue and red in the panel above, again, along with running mean values.

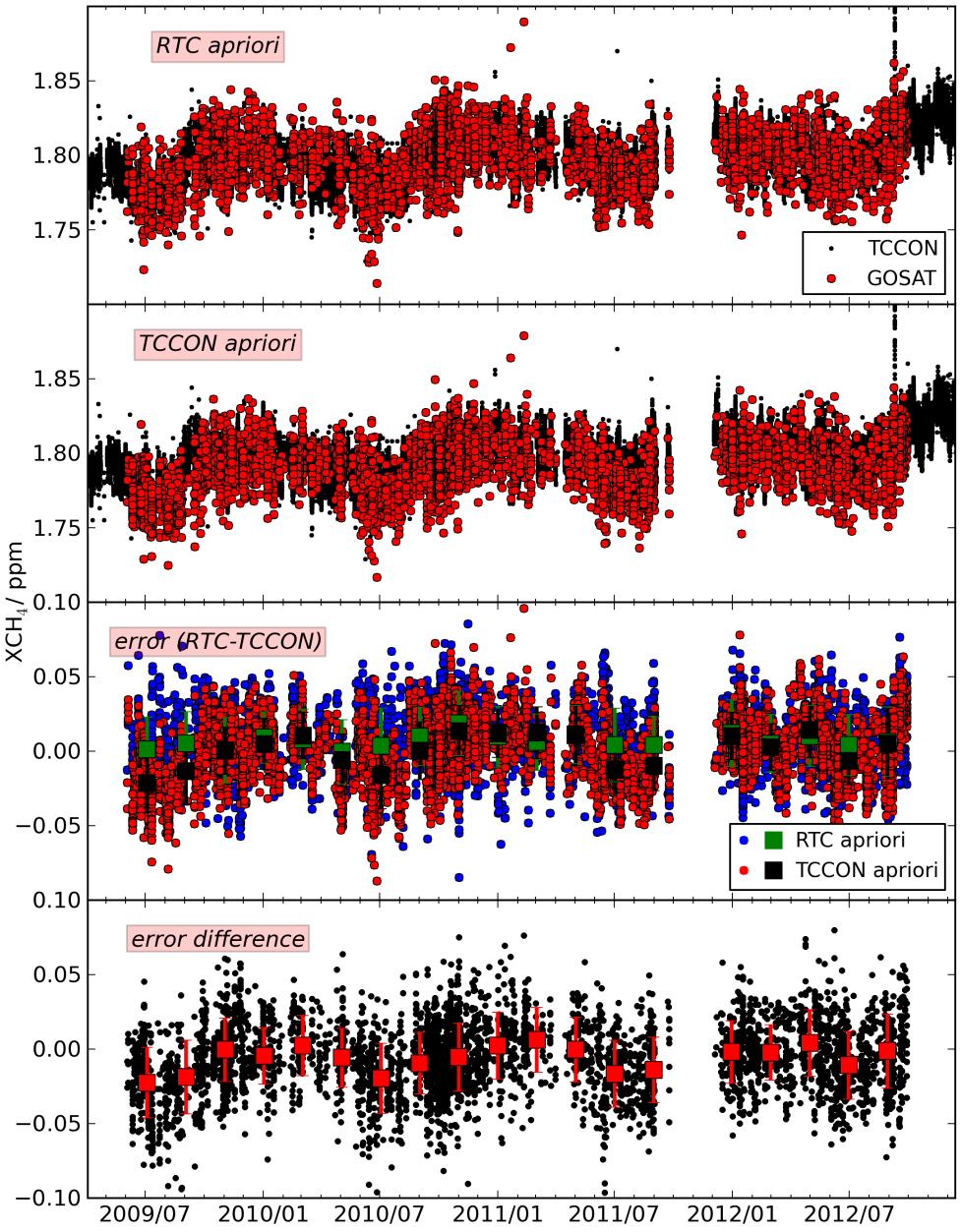

Figure A.7.: Analyzing the different seasonality of the apriori CH_4 profiles for the Baserun. The upper two panels show the time series of the collocated GOSAT TCCON pairs, with both the RemoTeC apriori and the TCCON apriori, respectively. The third panel from top contains the single measurement errors of both data sets along with running mean values for every two months. The standard error is attached to every running mean. The subsequent panel plots in black the differences between the errors, shown in blue and red in the panel above, again, along with running mean values.

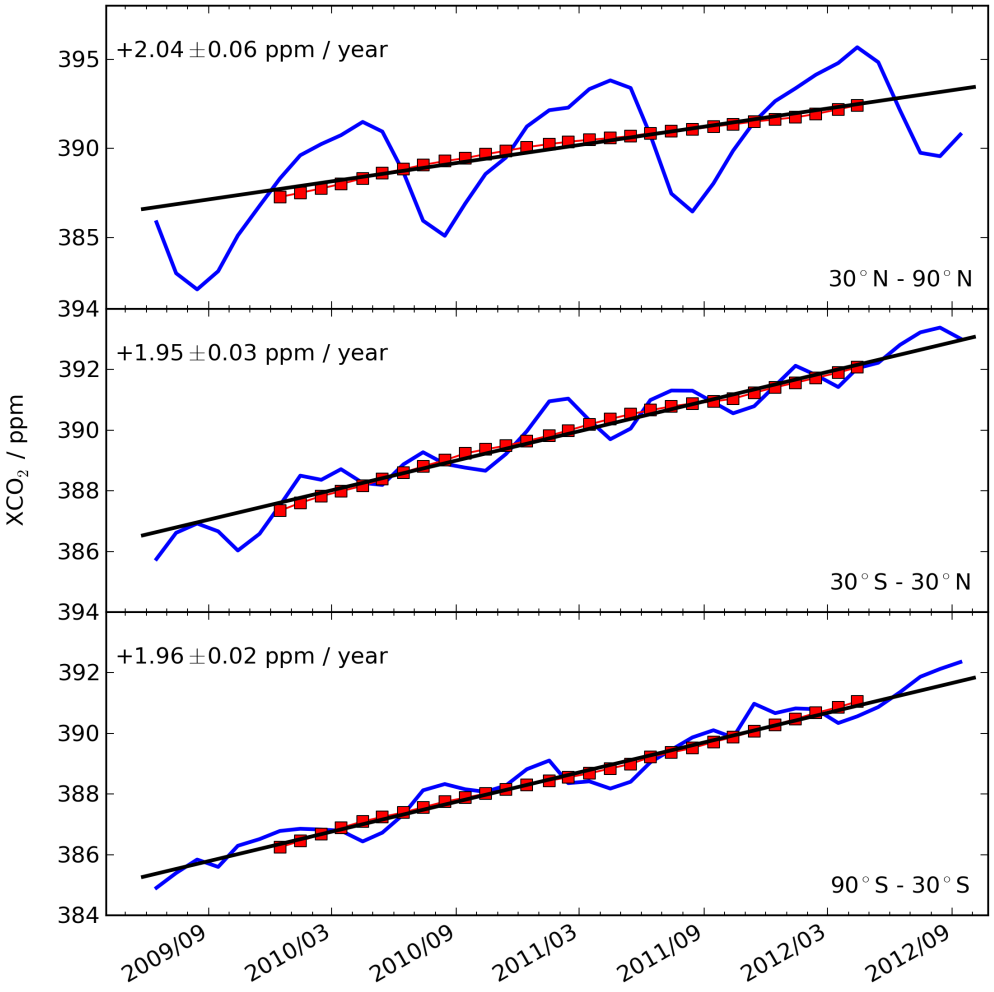

Figure A.8.: Annual increase of the Baserun XCO_2 for three 60° latitudinal zones. The latitude range of each zone is indicated in the lower right corner of each panel. All XCO_2 measurements within one month are averaged from 2° by 2° grid box averages (blue line). Red squares show XCO_2 running means for one year, e.g. for December 2010 all values are averaged from begin of June 2010 till end of May 2011. The black line represents a linear fit to the running means, extrapolated for the first and last six months of the regarded period. Its slope gives the annual increase in XCO_2 and is denoted in the top left of each panel. Its error is the regression's standard error.

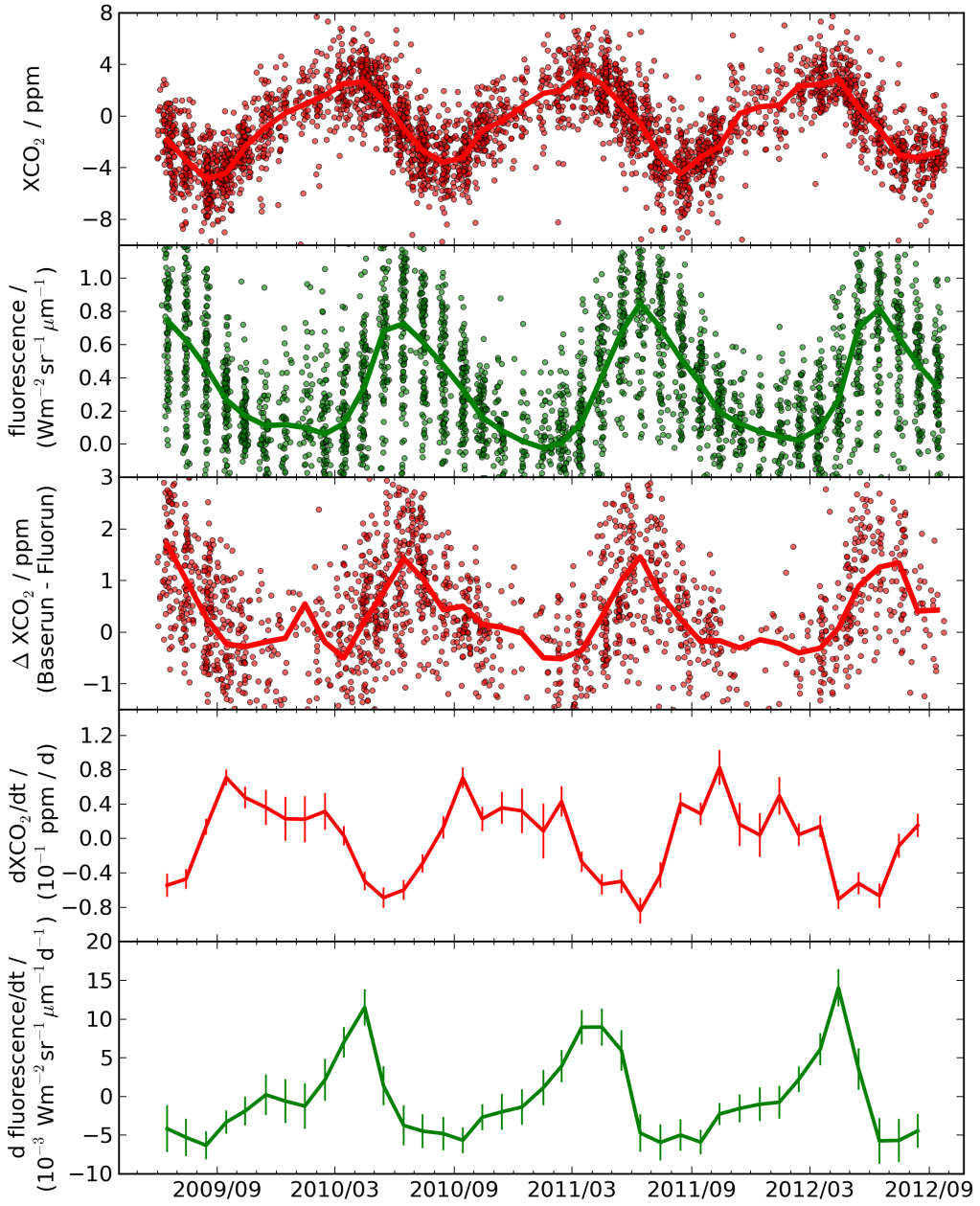

Figure A.9.: Timeseries of XCO_2 and fluorescence over Europe (16°W - 50°E, 30°N-60°N) The upper panel shows the detrended Fluorun XCO_2 time series. Plotted are the monthly averages of each 2° by 2° grid cell within the area. Additionally, the solid line links the monthly averages of the complete area. The second panel from top contains the chlorophyll fluorescence retrieved with the Fraunhofer concept. Same illustration as above but with 4° by 4° grid size. The difference between the Baserun's and the Fluorun's XCO_2 is demonstrated in the middle panel. The two lowest panels comprise the differential quotients of the monthly averages from the two top panels.

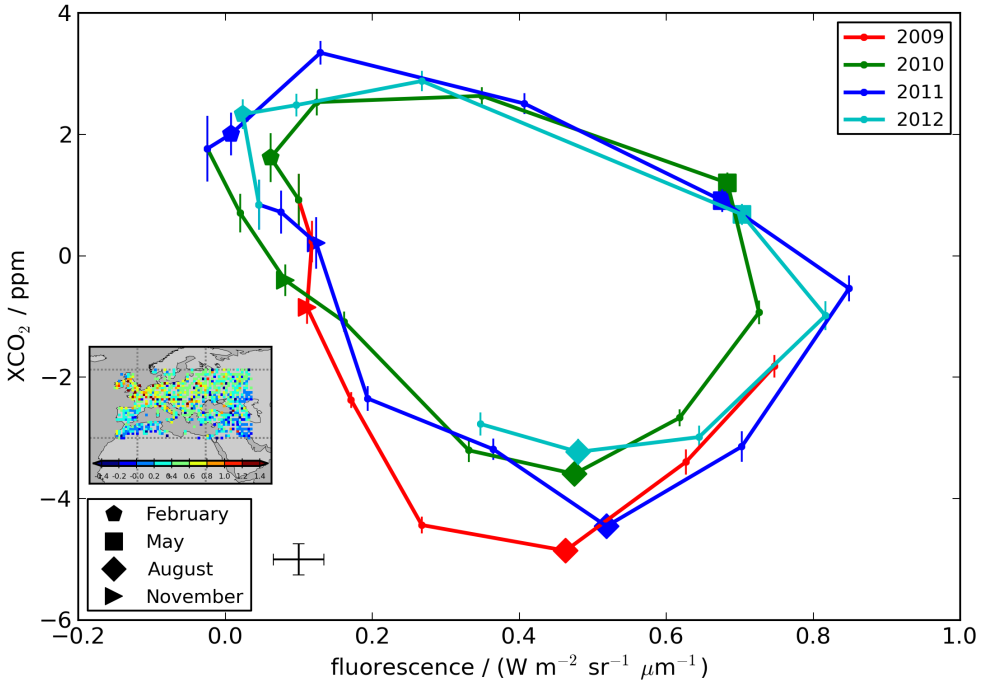

Figure A.10.: The carbon cycle over Europe. The monthly averages of XCO_2 are plotted versus the monthly averaged chlorophyll fluorescence, both are extracted from the top panels of figure 7.3. The solid line links the averages in chronological order. The color denotes the respective year. Four symbols give an orientation on the season. The error of the mean of XCO_2 is attached to each data point. For better visibility, the error of the mean of fluorescence is plotted only on average, see errorbars next to the lower right legend. The map inset visualizes the region with 1° by 1° averaged fluorescence signals. Its colorbar ranges from -0.4 to 1.4.

B. Publications

Results obtained within this work are reported in these two peer reviewed publications:

- Schepers, D., aan de Brugh, J., Hahne, P., Butz, A., Hasekamp, O., and Landgraf, J.: LINTRAN v2. 0: A linearised vector radiative transfer model for efficient simulation of satellite-born nadir-viewing reflection measurements of cloudy atmospheres, Journal of Quantitative Spectroscopy and Radiative Transfer, URL *http://www.sciencedirect.com/science/article/pii/S002240731400363X*, 2014.
- Guerlet, S., Basu, S., Butz, A., Krol, M., Hahne, P., Houweling, S., Hasekamp, O., and Aben, I.: Reduced carbon uptake during the 2010 Northern Hemisphere summer from GOSAT, Geophysical Research Letters, 40, 2378–2383, URL *http://onlinelibrary.wiley.com/doi/10.1002/grl.50402/full*, 2013a.

Posters presented on international conferences:

- Hahne, Guerlet, Hasekamp, TCCON partners, Butz: Performance evaluation of XCO2 retrievals from GOSAT using short-cut full physics methods, AGU Fall Meeting, 05.12.2012
- Hahne, Frankenberg, Hasekamp, Landgraf, Schepers, Butz: Chlorophyll fluorescence: implementation in the full physics RemoTeC algorithm, EGU Meeting, 02.05.2014

C. Acknowledgment

Access to GOSAT data was granted through the 2nd GOSAT research announcement jointly issued by JAXA, NIES, and MOE. I acknowledge all the individuals contributing to GOSAT's success.

ECMWF ERA Interim analyses are provided through the Web site http://data-portal.ecmwf.int/data/d/interim_daily/

CarbonTracker data are provided by NOAA ESRL, Boulder, Colorado, USA from the Web site at http://carbontracker.noaa.gov.

TCCON data were obtained from the TCCON Data Archive, operated by the California Institute of Technology from the website at http://tccon.ipac.caltech.edu/. In particular, I acknowledge the principle investigators Justus Notholt and Thorsten Warneke (Bialystok, Bremen, Orleans), David Griffith (Darwin, Wollongong), Ralf Sussmann (Garmisch), Frank Hase (Karlsruhe), and Paul Wennberg (Lamont, Park Falls).

I acknowledge Sourish Basu, National Oceanic and Atmospheric Administration, Global Monitoring Division, Boulder, USA, for performing several atmospheric inversions and supplying me with carbon surface flux estimates. The optimization used ObsPack data provided by NOAA ESRL, Boulder, Colorado, USA. In particular, data from 21 stations were used. I acknowledge the principle investigators Pieter Tans (NOAA), Arlyn Andrews (NOAA), Ed Dlugokencky (NOAA), Martin Steinbacher (JFJ), Marc Delmotte (LPO), Markus Leuenberger (JFJ), Luciana V. Gatti (IPEN), Ernst Brunke (CPT), Atsushi Takizawa (JMA), Colm Sweeney (NOAA), Paul Steele (CSIRO), Doug Worthy (EC), Michel Ramonet (LSCE/RAMCES), Ingeborg Levin (UHEI-IUP), Ralph Keeling, (SIO), Shinji Morimoto (SYO), Laszlo Haszpra (HUN), Britton Stephens (NCAR), Angel J. Gomez-Pelaez (IZO), Juha Hatakka (PAL), Kazuhiro Tsuboi (AOA), and Harro Meijer (RUG).

I acknowledge Martin Jung, Max Planck Institute for Biogeochemistry, Jena, Germany, for providing modeled gross primary production data.

The graduate school for climate and environment (GRACE) funded parts of my three month internship in Utrecht, Netherlands, and some interesting workshops.

Bibliography

Abrams, M. C., Toon, G., and Schindler, R.: Practical example of the correction of Fourier-transform spectra for detector nonlinearity, Applied optics, 33, 6307–6314, 1994.

Alexe, M., Bergamaschi, P., Segers, A., Detmers, R., Butz, A., Hasekamp, O., Guerlet, S., Parker, R., Boesch, H., Frankenberg, C., et al.: Inverse modelling of CH 4 emissions for 2010–2011 using different satellite retrieval products from GOSAT and SCIAMACHY, Atmospheric Chemistry and Physics, 15, 113–133, 2015.

Baker, N. R.: Chlorophyll fluorescence: a probe of photosynthesis in vivo, Annu. Rev. Plant Biol., 59, 89–113, 2008.

Basu, S., Guerlet, S., Butz, A., Houweling, S., Hasekamp, O., Aben, I., Krummel, P., Steele, P., Langenfelds, R., Torn, M., et al.: Global CO 2 fluxes estimated from GOSAT retrievals of total column CO 2, Atmospheric Chemistry and Physics, 13, 8695–8717, URL http://www.atmos-chem-phys.net/13/8695/2013/, 2013.

Basu, S., Krol, M., Butz, A., Clerbaux, C., Sawa, Y., Machida, T., Matsueda, H., Frankenberg, C., Hasekamp, O., and Aben, I.: The seasonal variation of the CO2 flux over Tropical Asia estimated from GOSAT, CONTRAIL, and IASI, Geophysical Research Letters, 41, 1809–1815, 2014.

Buchwitz, M., Reuter, M., Schneising, O., Boesch, H., Guerlet, S., Dils, B., Aben, I., Armante, R., Bergamaschi, P., Blumenstock, T., et al.: The Greenhouse Gas Climate Change Initiative (GHG-CCI): Comparison and quality assessment of near-surface-sensitive satellite-derived CO 2 and CH 4 global data sets, Remote Sensing of Environment, 2013.

Burrows, J., Hölzle, E., Goede, A., Visser, H., and Fricke, W.: SCIAMACHY - Scanning imaging absorption spectrometer for atmospheric chartography, Acta Astronautica, 35, 445–451, 1995.

Butz, A., Hasekamp, O. P., Frankenberg, C., and Aben, I.: Retrievals of atmospheric CO< sub> 2</sub> from simulated space-borne measurements of backscattered near-infrared sunlight: accounting for aerosol effects, Applied optics, 48, 3322–3336, URL http://www.opticsinfobase.org/abstract.cfm?uri=ao-48-18-3322, 2009.

Butz, A., Hasekamp, O., Frankenberg, C., Vidot, J., and Aben, I.: CH4 retrievals from space-based solar backscatter measurements: Performance evaluation against simulated aerosol and cirrus loaded scenes, Journal of Geophysical Research: Atmospheres (1984–2012), 115, 2010.

Butz, A., Guerlet, S., Hasekamp, O., Schepers, D., Galli, A., Aben, I., Frankenberg, C., Hartmann, J.-M., Tran, H., Kuze, A., et al.: Toward accurate CO2 and CH4 observations from GOSAT, Geophysical Research Letters, 38, 2011.

Butz, A., Galli, A., Hasekamp, O., Landgraf, J., Tol, P., and Aben, I.: TROPOMI aboard Sentinel-5 Precursor: Prospective performance of CH 4 retrievals for aerosol and cirrus loaded atmospheres, Remote Sensing of Environment, 120, 267–276, 2012.

Butz, A., Guerlet, S., Hasekamp, O., Kuze, A., and Suto, H.: Using ocean-glint scattered sunlight as a diagnostic tool for satellite remote sensing of greenhouse gases, Atmospheric Measurement Techniques Discussions, 6, 4371–4400, URL http://www.atmos-meas-tech-discuss.net/6/4371/2013/, 2013.

Chandrasekhar, S.: Radiative transfer, Courier Corporation, 1960.

Checa-Garcia, R., Landgraf, J., Hase, F., Tran, H., Boudon, V., Alkemade, F., and Butz, A.: Mapping spectroscopic uncertainties into prospective methane retrieval errors from Sentinel-5 and its precursor, Atmospheric Measurement Techniques Discussions, 8, 1333–1363, 2015.

Ciais, P., Sabine, C., Bala, G., Bopp, L., Brovkin, V., Canadell, J., Chhabra, A., DeFries, R., Galloway, J., Heimann, M., et al.: Carbon and other biogeochemical cycles, in: Climate change 2013: the physical science basis. Contribution of Working Group I to the Fifth Assessment Report of the Intergovernmental Panel on Climate Change, pp. 465–570, Cambridge University Press, 2014.

Cox, C. and Munk, W.: Statistics of the sea surface derived from sun glitter, Journal of Marine Research, 13, 198–227, 1954.

Crisp, D., Atlas, R., Breon, F.-M., Brown, L., Burrows, J., Ciais, P., Connor, B., Doney, S., Fung, I., Jacob, D., and et al.: The Orbiting Carbon Observatory (OCO) mission, Advances in Space Research, 34, 700–709, doi:10.1016/j.asr.2003.08.062, URL http://dx.doi.org/10.1016/j.asr.2003.08.062, 2004.

Crisp, D., Fisher, B., O'Dell, C., Frankenberg, C., Basilio, R., Bosch, H., Brown, L., Castano, R., Connor, B., Deutscher, N., et al.: The ACOS CO2 retrieval algorithm-Part II: Global XCO2 data characterization, 2012.

Dee, D., Uppala, S., Simmons, A., Berrisford, P., Poli, P., Kobayashi, S., Andrae, U., Balmaseda, M., Balsamo, G., Bauer, P., et al.: The ERA-Interim reanalysis: Configuration and performance of the data assimilation system, Quarterly Journal of the Royal Meteorological Society, 137, 553–597, 2011.

Dils, B., Buchwitz, M., Reuter, M., Schneising, O., Boesch, H., Parker, R., Guerlet, S., Aben, I., Blumenstock, T., Burrows, J., et al.: The Greenhouse Gas Climate Change Initiative (GHG-CCI): comparative validation of GHG-CCI SCIAMACHY/ENVISAT and TANSO-FTS/GOSAT CO2 and CH4 retrieval algorithm products with measurements from the TCCON, 2014.

Frankenberg, C., Butz, A., and Toon, G.: Disentangling chlorophyll fluorescence from atmospheric scattering effects in O2 A-band spectra of reflected sun-light, Geophysical Research Letters, 38, 2011a.

Frankenberg, C., Fisher, J. B., Worden, J., Badgley, G., Saatchi, S. S., Lee, J.-E., Toon, G. C., Butz, A., Jung, M., Kuze, A., et al.: New global observations of the terrestrial carbon cycle from GOSAT: Patterns of plant fluorescence with gross primary productivity, Geophysical Research Letters, 38, 2011b.

Frankenberg, C., O'Dell, C., Guanter, L., and McDuffie, J.: Remote sensing of near-infrared chlorophyll fluorescence from space in scattering atmospheres: implications for its retrieval and interferences with atmospheric CO 2 retrievals, Atmospheric Measurement Techniques, 5, 2081–2094, 2012.

Frankenberg, C., O'Dell, C., Berry, J., Guanter, L., Joiner, J., Köhler, P., Pollock, R., and Taylor, T. E.: Prospects for chlorophyll fluorescence remote sensing from the Orbiting Carbon Observatory-2, Remote Sensing of Environment, 147, 1–12, 2014.

Galli, A., Guerlet, S., Butz, A., Aben, I., Suto, H., Kuze, A., Deutscher, N., Notholt, J., Wunch, D., Wennberg, P., et al.: The impact of spectral resolution on satellite retrieval accuracy of CO2 and CH4, 2014.

Gerbig, C., Lin, J., Wofsy, S., Daube, B., Andrews, A., Stephens, B., Bakwin, P., and Grainger, C.: Toward constraining regional-scale fluxes of CO2 with atmospheric observations over a continent: 1. Observed spatial variability from airborne platforms, Journal of Geophysical Research: Atmospheres (1984–2012), 108, 2003.

Guanter, L., Alonso, L., Gómez-Chova, L., Meroni, M., Preusker, R., Fischer, J., and Moreno, J.: Developments for vegetation fluorescence retrieval from spaceborne high-resolution spectrometry in the O2-A and O2-B absorption bands, Journal of Geophysical Research: Atmospheres (1984–2012), 115, 2010.

Guanter, L., Frankenberg, C., Dudhia, A., Lewis, P. E., Gómez-Dans, J., Kuze, A., Suto, H., and Grainger, R. G.: Retrieval and global assessment of terrestrial chlorophyll fluorescence from GOSAT space measurements, Remote Sensing of Environment, 121, 236–251, 2012.

Guanter, L., Zhang, Y., Jung, M., Joiner, J., Voigt, M., Berry, J. A., Frankenberg, C., Huete, A. R., Zarco-Tejada, P., Lee, J.-E., et al.: Global and time-resolved monitoring of crop photosynthesis with chlorophyll fluorescence, Proceedings of the National Academy of Sciences, 111, E1327–E1333, 2014.

Guanter, L., Aben, I., Tol, P., Krijger, J., Hollstein, A., Köhler, P., Damm, A., Joiner, J., Frankenberg, C., and Landgraf, J.: Potential of the TROPOspheric Monitoring Instrument (TROPOMI) onboard the Sentinel-5 Precursor for the monitoring of terrestrial chlorophyll fluorescence, Atmospheric Measurement Techniques, 8, 1337–1352, 2015.

Guerlet, S., Basu, S., Butz, A., Krol, M., Hahne, P., Houweling, S., Hasekamp, O., and Aben, I.: Reduced carbon uptake during the 2010 Northern Hemisphere summer from GOSAT, Geophysical Research Letters, 40, 2378–2383, URL `http://onlinelibrary.wiley.com/doi/10.1002/grl.50402/full`, 2013a.

Guerlet, S., Butz, A., Schepers, D., Basu, S., Hasekamp, O., Kuze, A., Yokota, T., Blavier, J.-F., Deutscher, N., Griffith, D. T., et al.: Impact of aerosol and thin cirrus on retrieving and validating XCO2 from GOSAT shortwave infrared measurements, Journal of Geophysical Research: Atmospheres, 118, 4887–4905, URL `http://onlinelibrary.wiley.com/doi/10.1002/jgrd.50332/full`, 2013b.

Hamazaki, T., Kuze, A., and Kondo, K.: Sensor system for greenhouse gas observing satellite (GOSAT), in: Optical Science and Technology, the SPIE 49th Annual Meeting, pp. 275–282, International Society for Optics and Photonics, 2004.

Hasekamp, O. and Landgraf, J.: A linearized vector radiative transfer model for atmospheric trace gas retrieval, Journal of Quantitative Spectroscopy and Radiative Transfer, 75, 221–238, URL `http://www.sciencedirect.com/science/article/pii/S0022407301002473`, 2002.

Hasekamp, O. P. and Landgraf, J.: Ozone profile retrieval from backscattered ultraviolet radiances: The inverse problem solved by regularization, Journal of Geophysical Research: Atmospheres (1984–2012), 106, 8077–8088, URL `http://onlinelibrary.wiley.com/doi/10.1029/2000JD900692/full`, 2001.

Hasekamp, O. P. and Landgraf, J.: Linearization of vector radiative transfer with respect to aerosol properties and its use in satellite remote sensing, Journal of Geophysical Research: Atmospheres (1984–2012), 110, 2005.

Huete, A., Didan, K., Miura, T., Rodriguez, E. P., Gao, X., and Ferreira, L. G.: Overview of the radiometric and biophysical performance of the MODIS vegetation indices, Remote sensing of environment, 83, 195–213, 2002.

Ishida, H., Nakjima, T. Y., Yokota, T., Kikuchi, N., and Watanabe, H.: Investigation of gosat tanso-cai cloud screening ability through an intersatellite comparison, Journal of Applied Meteorology and Climatology, 50, 1571–1586, 2011.

Joiner, J., Yoshida, Y., Vasilkov, A., Middleton, E., et al.: First observations of global and seasonal terrestrial chlorophyll fluorescence from space, Biogeosciences, 8, 637–651, 2011.

Joiner, J., Yoshida, Y., Vasilkov, A., Middleton, E., Campbell, P., Kuze, A., et al.: Filling-in of near-infrared solar lines by terrestrial fluorescence and other geophysical effects: Simulations and space-based observations from SCIAMACHY and GOSAT, Atmospheric Measurement Techniques, 5, 809–829, 2012.

Joiner, J., Guanter, L., Lindstrot, R., Voigt, M., Vasilkov, A., Middleton, E., Huemmrich, K., Yoshida, Y., and Frankenberg, C.: Global monitoring of terrestrial chlorophyll fluorescence from moderate-spectral-resolution near-infrared satellite measurements: methodology, simulations, and application to GOME-2, 2013.

Jung, M., Reichstein, M., Margolis, H. A., Cescatti, A., Richardson, A. D., Arain, M. A., Arneth, A., Bernhofer, C., Bonal, D., Chen, J., et al.: Global patterns of land-atmosphere fluxes of carbon dioxide, latent heat, and sensible heat derived from eddy covariance, satellite, and meteorological observations, Journal of Geophysical Research: Biogeosciences (2005–2012), 116, 2011.

Krol, M., Houweling, S., Bregman, B., van den Broek, M., Segers, A., van Velthoven, P., Peters, W., Dentener, F., and Bergamaschi, P.: The two-way nested global chemistry-transport zoom model TM5: algorithm and applications, Atmospheric Chemistry and Physics, 5, 417–432, doi:10.5194/acp-5-417-2005, URL `http://dx.doi.org/10.5194/acp-5-417-2005`, 2005.

Kuze, A., Suto, H., Nakajima, M., and Hamazaki, T.: Thermal and near infrared sensor for carbon observation Fourier-transform spectrometer on the Greenhouse Gases Observing Satellite for greenhouse gases monitoring, Applied optics, 48, 6716–6733, 2009.

Kuze, A., Suto, H., Shiomi, K., Urabe, T., Nakajima, M., Yoshida, J., Kawashima, T., Yamamoto, Y., and Kataoka, F.: Level 1 algorithms for TANSO on GOSAT: processing and on-orbit calibrations, Atmospheric Measurement Techniques Discussions, 5, 2959–3018, 2012.

Lamouroux, J., Tran, H., Laraia, A., Gamache, R., Rothman, L., Gordon, I., and Hartmann, J.-M.: Updated database plus software for line-mixing in CO 2 infrared spectra and their test using laboratory spectra in the 1.5–2.3 μm region, Journal of Quantitative Spectroscopy and Radiative Transfer, 111, 2321–2331, 2010.

Landgraf, J., Hasekamp, O. P., Box, M. A., and Trautmann, T.: A linearized radiative transfer model for ozone profile retrieval using the analytical forward-adjoint perturbation theory approach, Journal of Geophysical Research: Atmospheres (1984–2012), 106, 27 291–27 305, URL `http://onlinelibrary.wiley.com/doi/10.1029/2001JD000636/full`, 2001.

Landgraf, J., Hasekamp, O., and Trautmann, T.: Linearization of radiative transfer with respect to surface properties, Journal of Quantitative Spectroscopy and Radiative Transfer, 72, 327–339, URL `http://www.sciencedirect.com/science/article/pii/S0022407301001261`, 2002.

Le Quéré, C., Moriarty, R., Andrew, R., Peters, G., Ciais, P., Friedlingstein, P., Jones, S., Sitch, S., Tans, P., Arneth, A., et al.: Global carbon budget 2014, Earth System Science Data Discussions, 7, 521–610, 2014.

Lee, J.-E., Frankenberg, C., van der Tol, C., Berry, J. A., Guanter, L., Boyce, C. K., Fisher, J. B., Morrow, E., Worden, J. R., Asefi, S., et al.: Forest productivity and water stress in Amazonia: observations from GOSAT chlorophyll fluorescence, Proceedings of the Royal Society B: Biological Sciences, 280, 20130 171, 2013.

Lichtenthaler, H. K. and Miehe, J. A.: Fluorescence imaging as a diagnostic tool for plant stress, Trends in Plant Science, 2, 316–320, 1997.

Lichtenthaler, H. K. and Rinderle, U.: The role of chlorophyll fluorescence in the detection of stress conditions in plants, CRC Critical Reviews in Analytical Chemistry, 19, S29–S85, 1988.

Liou, K.-N.: An introduction to atmospheric radiation, vol. 84, Academic press, 2002.

Mandrake, L., Frankenberg, C., O'Dell, C., Osterman, G., Wennberg, P., and Wunch, D.: Semi-autonomous sounding selection for OCO-2, Atmospheric Measurement Techniques, 6, 2851–2864, 2013.

Masarie, K., Peters, W., Jacobson, A., and Tans, P.: ObsPack: a framework for the preparation, delivery, and attribution of atmospheric greenhouse gas data, Earth System Science Data Discussions, 7, 495–519, 2014.

Meirink, J., Eskes, H., and Goede, A.: Sensitivity analysis of methane emissions derived from SCIAMACHY observations through inverse modelling, Atmospheric chemistry and physics, 6, 1275–1292, 2006.

Meirink, J. F., Bergamaschi, P., and Krol, M. C.: Four-dimensional variational data assimilation for inverse modelling of atmospheric methane emissions: method and comparison with synthesis inversion, Atmospheric Chemistry and Physics, 8, 6341–6353, doi:10.5194/acp-8-6341-2008, URL `http://dx.doi.org/10.5194/acp-8-6341-2008`, 2008.

Meroni, M., Rossini, M., Guanter, L., Alonso, L., Rascher, U., Colombo, R., and Moreno, J.: Remote sensing of solar-induced chlorophyll fluorescence: Review of methods and applications, Remote Sensing of Environment, 113, 2037–2051, 2009.

Morino, I., Uchino, O., Inoue, M., Yoshida, Y., Yokota, T., Wennberg, P., Toon, G., Wunch, D., Roehl, C., Notholt, J., et al.: Preliminary validation of column-averaged volume mixing ratios of carbon dioxide and methane retrieved from GOSAT short-wavelength infrared spectra, Atmospheric Measurement Techniques, 4, 1061–1076, 2011.

Munro, R., Eisinger, M., Anderson, C., Callies, J., Corpaccioli, E., Lang, R., Lefebvre, A., Livschitz, Y., and Albiñana, A. P.: GOME-2 on MetOp, in: Proc. of The 2006 EUMETSAT Meteorological Satellite Conference, Helsinki, Finland, pp. 12–16, 2006.

Nguyen, H., Osterman, G., Wunch, D., O'Dell, C., Mandrake, L., Wennberg, P., Fisher, B., and Castano, R.: A method for colocating satellite X CO 2 data to ground-based data and its application to ACOS-GOSAT and TCCON, Atmospheric Measurement Techniques Discussions, 7, 1495–1533, URL `http://www.atmos-meas-tech-discuss.net/7/1495/2014/amtd-7-1495-2014.html`, 2014.

O'Brien, D. M., Polonsky, I., O'Dell, C., Kuze, A., Kikuchi, N., Yoshida, Y., and Natraj, V.: Testing the Polarization Model for TANSO-FTS on GOSAT Against Clear-Sky Observations of Sun Glint Over the Ocean, Geoscience and Remote Sensing, IEEE Transactions on, 51, 5199–5209, 2013.

O'Dell, C., Connor, B., Bösch, H., O'Brien, D., Frankenberg, C., Castano, R., Christi, M., Eldering, A., Fisher, B., Gunson, M., et al.: The ACOS CO [subscript 2] retrieval algorithm-Part 1: Description and validation against synthetic observations, 2012.

Oshchepkov, S., Bril, A., Yokota, T., Wennberg, P. O., Deutscher, N. M., Wunch, D., Toon, G. C., Yoshida, Y., O'Dell, C. W., Crisp, D., et al.: Effects of atmospheric light scattering on spectroscopic observations of greenhouse gases from space. Part 2: Algorithm intercomparison in the GOSAT data processing for CO2 retrievals over TCCON sites, Journal of Geophysical Research: Atmospheres, 118, 1493–1512, URL `http://onlinelibrary.wiley.com/doi/10.1002/jgrd.50146/full`, 2013.

Papageorgiou, G.: Chlorophyll fluorescence: an intrinsic probe of photosynthesis, Bioenergetics of photosynthesis, pp. 319–371, 1975.

Papageorgiou, G. C.: Chlorophyll a fluorescence: a signature of photosynthesis, vol. 19, Springer Science & Business Media, 2004.

Parazoo, N. C., Bowman, K., Frankenberg, C., Lee, J.-E., Fisher, J. B., Worden, J., Jones, D., Berry, J., Collatz, G. J., Baker, I. T., et al.: Interpreting seasonal changes in the carbon balance of southern Amazonia using measurements of XCO2 and chlorophyll fluorescence from GOSAT, Geophysical Research Letters, 40, 2829–2833, URL `http://onlinelibrary.wiley.com/doi/10.1002/grl.50452/full`, 2013.

Parker, R., Boesch, H., Cogan, A., Fraser, A., Feng, L., Palmer, P. I., Messerschmidt, J., Deutscher, N., Griffith, D. W., Notholt, J., et al.: Methane observations from the Greenhouse Gases Observing SATellite: Comparison to ground-based TCCON data and model calculations, Geophysical Research Letters, 38, 2011.

Peters, W., Jacobson, A. R., Sweeney, C., Andrews, A. E., Conway, T. J., Masarie, K., Miller, J. B., Bruhwiler, L. M., Petron, G., Hirsch, A. I., et al.: An atmospheric perspective on North American carbon dioxide exchange: CarbonTracker, Proceedings of the National Academy of Sciences, 104, 18 925–18 930, 2007.

Plascyk, J. A.: The MK II Fraunhofer line discriminator (FLD-II) for airborne and orbital remote sensing of solar-stimulated luminescence, Optical Engineering, 14, 339–0, 1975.

Reuter, M., Buchwitz, M., Hilker, M., Heymann, J., Schneising, O., Pillai, D., Bovensmann, H., Burrows, J., Bösch, H., Parker, R., et al.: Satellite-inferred European carbon sink larger than expected, Atmospheric Chemistry and Physics, 14, 13 739–13 753, 2014.

Rodgers, C. D. et al.: Inverse methods for atmospheric sounding: theory and practice, vol. 2, World scientific Singapore, 2000.

Rothman, L., Gordon, I., Babikov, Y., Barbe, A., Benner, D. C., Bernath, P., Birk, M., Bizzocchi, L., Boudon, V., Brown, L., et al.: The HITRAN2012 molecular spectroscopic database, Journal of Quantitative Spectroscopy and Radiative Transfer, 130, 4–50, 2013.

Rothman, L. S., Gordon, I. E., Barbe, A., Benner, D. C., Bernath, P. F., Birk, M., Boudon, V., Brown, L. R., Campargue, A., Champion, J.-P., et al.: The HITRAN 2008 molecular spectroscopic database, Journal of Quantitative Spectroscopy and Radiative Transfer, 110, 533–572, 2009.

Schepers, D., Guerlet, S., Butz, A., Landgraf, J., Frankenberg, C., Hasekamp, O., Blavier, J.-F., Deutscher, N., Griffith, D., Hase, F., et al.: Methane retrievals from Greenhouse Gases Observing Satellite (GOSAT) shortwave infrared measurements: Performance comparison of proxy and physics retrieval algorithms, Journal of Geophysical Research: Atmospheres (1984–2012), 117, 2012.

Schepers, D., aan de Brugh, J., Hahne, P., Butz, A., Hasekamp, O., and Landgraf, J.: LINTRAN v2. 0: A linearised vector radiative transfer model for efficient simulation of satellite-born nadir-viewing reflection measurements of cloudy atmospheres, Journal of Quantitative Spectroscopy and Radiative Transfer, URL `http://www.sciencedirect.com/science/article/pii/S002240731400363X`, 2014.

Schulze, E.-D.: Biological control of the terrestrial carbon sink, Biogeosciences, 3, 147–166, 2006.

Sioris, C. E., Bazalgette Courrèges-Lacoste, G., and Stoll, M.-P.: Filling in of Fraunhofer lines by plant fluorescence: Simulations for a nadir-viewing satellite-borne instrument, Journal of Geophysical Research: Atmospheres (1984–2012), 108, 2003.

Stephens, B. B., Gurney, K. R., Tans, P. P., Sweeney, C., Peters, W., Bruhwiler, L., Ciais, P., Ramonet, M., Bousquet, P., Nakazawa, T., and et al.: Weak Northern and Strong Tropical Land Carbon Uptake from Vertical Profiles of Atmospheric CO2, Science, 316, 1732–1735, doi:10.1126/science.1137004, URL `http://dx.doi.org/10.1126/science.1137004`, 2007.

Stocker, T., Qin, D., Plattner, G.-K., Tignor, M., Allen, S. K., Boschung, J., Nauels, A., Xia, Y., Bex, V., and Midgley, P. M.: Climate change 2013: The physical science basis, Cambridge University Press Cambridge, UK, and New York, 2014.

Stoll, M.-P., Laurila, T., Cunin, B., Gitelson, A. A., Lichtenthaler, H. K., and Hame, T.: FLEX: fluorescence explorer–a space mission for screening vegetated areas in the Fraunhofer lines, in: Remote Sensing, pp. 108–119, International Society for Optics and Photonics, 1999.

Takagi, H., Houweling, S., Andres, R. J., Belikov, D., Bril, A., Boesch, H., Butz, A., Guerlet, S., Hasekamp, O., Maksyutov, S., et al.: Influence of differences in current GOSAT XCO2 retrievals on surface flux estimation, Geophysical Research Letters, 41, 2598–2605, 2014.

Tran, H. and Hartmann, J.-M.: An improved O2 A band absorption model and its consequences for retrievals of photon paths and surface pressures, Journal of Geophysical Research: Atmospheres (1984–2012), 113, 2008.

Tucker, C. J.: Red and photographic infrared linear combinations for monitoring vegetation, Remote sensing of Environment, 8, 127–150, 1979.

Ustinov, E.: Inverse problem of the photometry of solar radiation reflected from an optically thick planetary atmosphere-Mathematical framework and weight functions of the linearized inverse problem, Kosmicheskie Issledovaniia, 29, 604–620, 1991.

Ustinov, E. A.: Adjoint sensitivity analysis of radiative transfer equation: temperature and gas mixing ratio weighting functions for remote sensing of scattering atmospheres in thermal IR, Journal of Quantitative Spectroscopy and Radiative Transfer, 68, 195–211, 2001.

Van der Tol, C., Verhoef, W., and Rosema, A.: A model for chlorophyll fluorescence and photosynthesis at leaf scale, Agricultural and forest meteorology, 149, 96–105, 2009a.

Van der Tol, C., Verhoef, W., Timmermans, J., Verhoef, A., and Su, Z.: An integrated model of soil-canopy spectral radiances, photosynthesis, fluorescence, temperature and energy balance, Biogeosciences, 6, 3109–3129, 2009b.

Vasilkov, A., Joiner, J., and Spurr, R.: Note on rotational-Raman scattering in the O 2 A-and B-bands: implications for retrieval of trace-gas concentrations and terrestrial chlorophyll fluorescence, Atmospheric Measurement Techniques Discussions, 5, 8789–8813, 2012.

Veefkind, J., Aben, I., McMullan, K., Förster, H., De Vries, J., Otter, G., Claas, J., Eskes, H., De Haan, J., Kleipool, Q., et al.: TROPOMI on the ESA Sentinel-5 Precursor: A GMES mission for global observations of the atmospheric composition for climate, air quality and ozone layer applications, Remote Sensing of Environment, 120, 70–83, 2012.

Walter, H. H., Landgraf, J., and Hasekamp, O. P.: Linearization of a pseudo-spherical vector radiative transfer model, Journal of Quantitative Spectroscopy and Radiative Transfer, 85, 251–283, 2004.

Wellburn, A. R.: The spectral determination of chlorophylls a and b, as well as total carotenoids, using various solvents with spectrophotometers of different resolution, Journal of plant physiology, 144, 307–313, 1994.

Wunch, D., Toon, G. C., Blavier, J.-F. L., Washenfelder, R. A., Notholt, J., Connor, B. J., Griffith, D. W., Sherlock, V., and Wennberg, P. O.: The total carbon column observing network, Philosophical Transactions of the Royal Society A: Mathematical, Physical and Engineering Sciences, 369, 2087–2112, 2011a.

Wunch, D., Wennberg, P., Toon, G., Connor, B., Fisher, B., Osterman, G., Frankenberg, C., Mandrake, L., O'Dell, C., Ahonen, P., et al.: A method for evaluating bias in global measurements of CO 2 total columns from space, Atmospheric Chemistry and Physics, 11, 12 317–12 337, URL http://www.atmos-chem-phys.net/11/12317/2011/acp-11-12317-2011.html, 2011b.

Yokota, T., Oguma, H., Morino, I., Higurashi, A., Aoki, T., and Inoue, G.: Test measurements by a BBM of the nadir-looking SWIR FTS aboard GOSAT to monitor CO2 column density from space, in: Fourth International Asia-Pacific Environmental Remote Sensing Symposium 2004: Remote Sensing of the Atmosphere, Ocean, Environment, and Space, pp. 182–188, International Society for Optics and Photonics, URL http://proceedings.spiedigitallibrary.org/proceeding.aspx?articleid=857154, 2004.